HIGH PERFORMANCE LASERS AND SPIN-POLARIZED LIGHT EMITTING DIODES WITH QUANTUM DOT ACTIVE REGIONS

by

Sasan Fathpour

A dissertation submitted in partial fulfillment
of the requirements for the degree of
Doctor of Philosophy
(Electrical Engineering)
in The University of Michigan
2005

Doctoral Committee:

Professor Pallab K. Bhattacharya, Chair
Associate Professor Rachel S. Goldman
Associate Professor Fred L. Terry
Assistant Professor Jamie D. Phillips

To the memory of
my grandfather,
Nasser Zamanifar

ACKNOWLEDGMENTS

This work would not have been possible without the visionary coaching and exceptional support of my Ph.D. advisor, Professor Pallab Bhattacharya, to whom I am deeply grateful. He has never hesitated in receiving me for any discussion and his office door has always been open to me for sometimes several meetings in a day. I am thankful to the other members of my doctoral committee Professors Rachel Goldman, Fred Terry and Jamie Phillips for their time and valuable suggestions to improve the quality of this dissertation. I also thank Professor Kevin Pipe for serving as a substitute in my oral defense. I am deeply grateful to my mentors and ex-colleagues, Professor Siddhartha Ghosh and Dr. Sameer Pradhan and to my colleagues Zetian Mi, Dr. Subhananda Chakrabarti, Mike Holub and Juraj Topolancik for their great help and contributions to this work. I would appreciate the technical support of the Solid-State Electronics Laboratory of the University of Michigan and I acknowledge the funding agencies of my projects (Army Research Office, Defense Advanced Research Projects Agency and Air Force Office of Scientific Research). I sincerely thank Dr. Alexey Kovsh and his colleagues at NL Nanosemiconductor GmbH, Dortmund, Germany for the epitaxial growth of the 1.3 μm p-doped quantum dot laser heterostructures. I would acknowledge Yuanyuan Lei at Argonne National Laboratory, Argonne, IL for the transmission electron micrographs and X-ray energy dispersive spectroscopy analysis on diluted magnetic quantum dots.

I came to Ann Arbor more than four and a half years ago with the invaluable helps of my only friend in Michigan, Babak Amirparviz, whom I wish the best in his life. I will be soon leaving the city with many wonderful friends I have found here. I will carry a lot

of pleasant memories of the time I have shared with Pedram Mohseni, Tara Javidi, Weber Stayman, Yulia Hanansen, Shayan Afshar, Shervin AhmadBeygi, Idin Motedayen, Farhad Ameri, Ardalan Vahidi, my group-mates and many other great friends.

My family friends and relatives Dr. Mehdi Naghdi, Mr. and Mrs. Cyrus Radmanesh and Dr. Shokoufeh Naderi have been generously hosting me during my vacations and providing me warm family environments, for which I am very thankful. It has been very distressing to live away from my beloved homeland, Iran, over these years with a *de facto* prohibition of traveling there and visiting my friends and extended family and particularly my younger brother, Saman, whom I miss so much. I have to express my wholehearted gratitude to my other brother, Kamyar, and my parents, Roohangiz and Hossein, for their love and priceless supports and for visiting me here. Last but not least, I should find something beyond words to voice my thanks to my love, Haleh, whose appearance in my cold life during the course of my Ph.D. program has been the ultimate motivation to finish this work.

SASAN FATHPOUR

Ann Arbor, Michigan

May 16, 2005

TABLE OF CONTENTS

LIST OF FIGURES

Figure

LIST OF TABLES

Table

CHAPTER I

INTRODUCTION

"May the right hand of Light guard and save you..."
FROM EPISTLES OF MANI
(PHILOSOPHER OF 3RD CENTURY A.D.)

1.1 Foreword

Very few engineering accomplishments in modern history have been acknowledged and celebrated as outstanding contributions to the human civilization. If we rely on the judgment of the Nobel Foundation over the last century, we can only name the invention of transistors, integrated circuits, and semiconductor heterostructures as engineering achievements worthy of awarding the prize in Physics. In the press release of the first Physics prize of the new millennium, awarded to Z. I. Alferov and H. Kroemer (who shared half of the prize), we read:

> *"Zhores I. Alferov and Herbert Kroemer have invented and developed fast opto- and microelectronic components based on layered semiconductor structures, termed semiconductor heterostructures. Fast transistors built using heterostructure technology are used in e.g. radio link satellites and the base stations of mobile telephones. Laser diodes built with the same technology drive the flow of information in the Internet's fibre-optical cables. They are also found in CD players, bar-code readers and laser pointers. With heterostructure technology powerful light-emitting diodes are being built for use in car brake-lights, traffic lights and other warning lights. Electric bulbs may in the future be replaced by light-emitting diodes."*

The original idea of spontaneous and stimulated light emission in direct band gap semiconductor heterojunctions is about fifty years old. Nonetheless, the mentioned

applications in the above press release are fairly recent and have demanded more and more improvements in the characteristics of semiconductor lasers and light emitting diodes. The philosophy of my thesis can perhaps be viewed in this general context, if I want to summarize it in one sentence.

One of the major applications of semiconductor lasers is as the light source of optical fiber communication systems. The almost unlimited bandwidth of single-mode fibers provides the opportunity for broad-band optical transmission of data in local area networks (LAN), metropolitan area networks (MAN) and long-haul intercontinental networks. The wavelength range of interest is from 0.9 to 1.6 μm, which is selected for a certain system by cost concerns as well as the loss and dispersion of present silica fiber technology. Wavelength division multiplexing (WDM) is a scheme to utilize the very high bandwidth capacity of fiber communication. In this scheme, numerous parallel light sources with different wavelengths are multiplexed at the transmitter end into the optical channel and demultiplexed at the receiver end. For the realization of such a broad-band network, semiconductor lasers with high spectral purity, low threshold current, high modulation bandwidth, tunable wavelength and high power are desirable.

Future 80 GHz WDM systems require optical sources with more challenging bandwidths. Currently, with the availability of single-mode fiber and high-speed (>60 GHz) photodetectors, the bottleneck of speed in an optical channel seems to be the low (<40 GHz) modulation bandwidth of semiconductor lasers. A fascinating emerging technology to further exploit the capacities of optical modulation is *spintronics*, which utilizes the polarization of the modulating light. In other words, if the handedness of the circularly polarized input light of the optical channel can be manipulated, a new

dimension is added to modulation schemes. For instance, (In)(Ga)MnAs compounds are diluted magnetic semiconductors which can inject spin-polarized carriers into the active region of high performance light sources, in order to provide polarized light output. Since spintronic materials also have applications in memory devices, it can be envisioned that electronic, memory and optoelectronic components of multitasking systems can be integrated on a single chip in the future.

1.2 History of Semiconductor Lasers

The year 1962 will probably be recognized as the birth date of semiconductor lasers in the history of science and technology. Four groups reported electrically injected stimulated emission of radiation from GaAs and GaAsP homojunctions [1]-[4]. Arguably, many claims can be made regarding the first person who suggested the idea of making a semiconductor laser, but the referred four demonstrations were realized without the benefit of these suggestions [5]. The next breakthrough was when Alferov and Kroemer independently developed the concept of double heterostructure (DHS) lasers [6],[7], which leads to superior injection of carriers, and better optical and carrier confinement. Technological challenges of epitaxial growth of high quality heterostructures delayed the continuous wave operation of DHS lasers at room temperature until 1970 [8],[9].

As schematically shown in Fig. 1.1, by quantum confinement of carriers in a thin well (e.g., GaAs/AlGaAs), the density of states (DOS) would noticeably increase and become less temperature dependent, which leads to a reduction in threshold current density, improved gain, modulation bandwidth, etc. The first preliminary report on quantum well (QW) lasers appeared in 1975 [10], but the first laser with characteristics

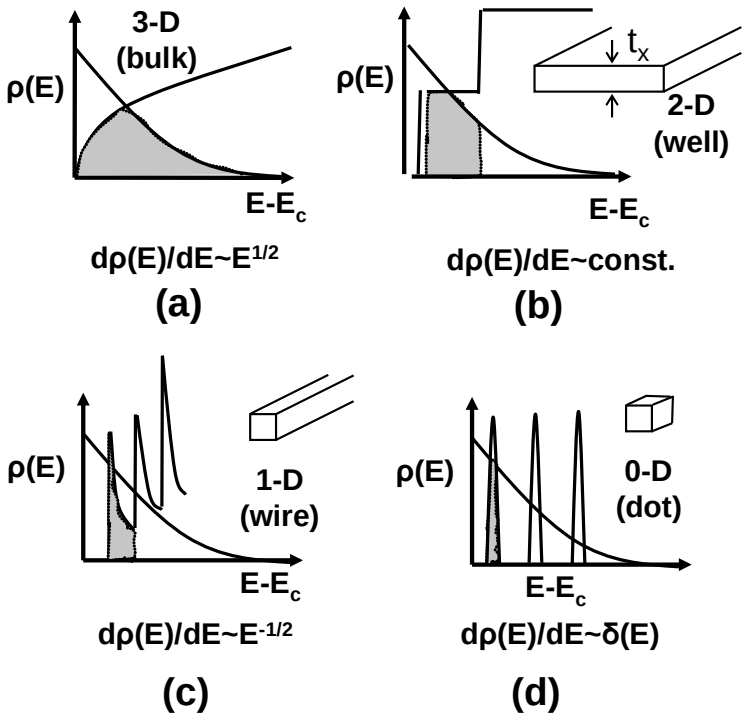

Fig. 1.1: Schematic of density of states, $\rho(E)$, versus energy with respect to the conduction band edge for different dimensional confinements: (a) bulk (3-D); (b) quantum well (2-D); (c) quantum wire (1-D) and (d) quantum dot (0-D). The shaded areas represent carrier densities with identical quasi-Fermi levels.

matching DHS lasers was demonstrated three years later [11]. This would not have been possible without tremendous efforts of researchers in developing two modern epitaxial growth techniques, i.e., metal organic vapor phase epitaxy (MOCVD) [12] and molecular beam epitaxy (MBE) [13]. Currently, commercial QW lasers based on GaAs and InP emitting at 0.9 to 1.6 μm are standard light sources for fiber optical communication systems, which is a multi-billion dollar industry. The characteristics of QW lasers have been improving steadily since their first demonstration of low threshold current, high output power and efficiency, and large modulation bandwidth. However, QW lasers suffer from large dynamic chirp and rather strong temperature dependence of threshold currents, especially at longer wavelengths.

1.3 Quantum Dot Lasers

The success of two-dimensional (2-D) confined, quantum well lasers in the 1980's attracted attention to lower dimensional confinements, i.e., quantum wires and quantum dots (QD) with 1-D and 0-D carrier confinement, respectively. 1-D and 0-D confined heterostructures would possess increased DOS (Fig. 1.1), which in turn leads to narrower optical gain spectrum and increased differential gain. Arakawa and Sakaki [14] theoretically considered these effects and, in particular, predicted significant reduction of threshold current and infinite characteristic temperature in *ideal* QD lasers due to their singular DOS. By fabricating the dots with electron beam lithography and etching techniques, QD lasers became a reality in 1994 [15]. However, due to interface defects these lasers had threshold current densities as high as 7.6 kA/cm^2 even at 77 K. As discussed in the next Chapter, self-organized QDs grown by MBE and MOCVD appear to be the most promising technique to form 3-D confined islands for various devices, such as far infrared detectors [16]-[18], field effect transistors [19], electro-optic modulators [20], and of course lasers [21]-[25]. The self-organized QD laser was first demonstrated by MBE in 1994 with a threshold current density of 120 A/cm^2 [21], and was followed by lasers grown by MOCVD [22]. It is noteworthy that Bhattacharya's optoelectronics group at the University of Michigan is one of the first groups to report room temperature operation and modulation properties of QD lasers [23]-[25].

Currently, QD lasers with threshold current densities as low as 13 A/cm^2 [26], large differential gain [25],[27], reduced linewidth enhancement factor [28] and chirp [29], and suppressed filamentation [30] have been reported in conventional QD lasers. However, as discussed in Chapter II, unique and inherent problems associated with conventional QD

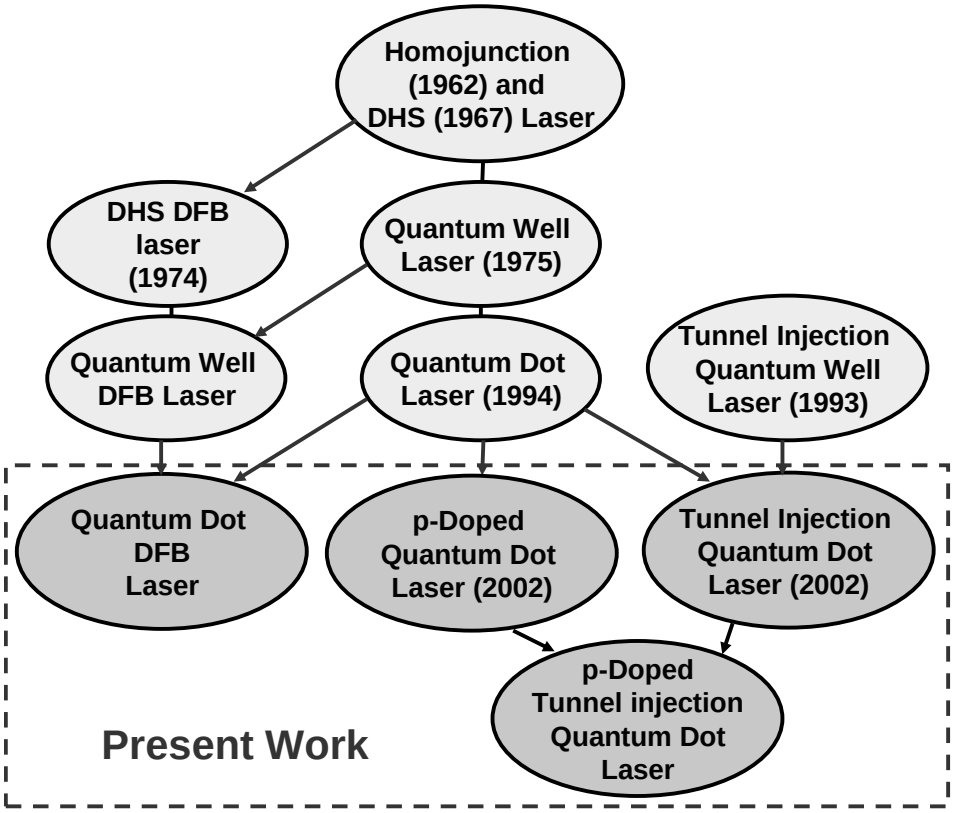

Fig 1.2: Different types of high-performance quantum dot lasers discussed in this thesis, with respect to a relevant chronologic diagram for the development of different types of semiconductor lasers in the last few decades.

lasers limit their performance in obtaining single-mode operation, ultrahigh characteristic temperature and large modulation bandwidth. The solution for single-mode operation is the well-known distributed feedback (DFB) mechanism. P-doping and tunnel injection (TI) have been proposed as solutions to the latter unique problems. Studying the characteristics and physics of these three types of lasers are the main focus of the present thesis. The different high-performance QD lasers studied here are categorized in Fig. 1.2, along with the chronology of advancement of semiconductor laser technology relevant to this work.

1.4 Spintronics for Optical Communication

As I discussed in Section 1.1, spintronics promises to increase the effective bandwidth of WDM optical fiber networks by adding a new dimension, polarization of the light carrying the signal, in the modulation schemes for optical transmission. Exploiting spin to store information is by no means new. As a matter of fact, magnetic tapes, hard disks and magneto-optical tapes for data storage based on ferromagnetic materials (mostly *metals*) have been commonplace for decades. The concept of spintronics, however, is a new paradigm in electronic and optoelectronic devices. It is an emerging field that exploits carriers spin in *semiconductor* materials - in addition to charge - for storing, manipulating and communicating data [31]. Spin transistors and spin memory devices are examples of electronic applications [32],[33]. Optical spintronics is not only a means of detecting carriers spin [34] but spin-polarized light sources are promising devices for future optical communication systems [35]. In a broader sense, spintronics also includes spin-based quantum computation where a quantum bit (qubit) is the fundamental unit of information [36].

A viable spintronics technology requires four fundamental elements: (a) efficient electrical injection of spin-polarized carriers from a ferromagnetic contact or spin-aligning layer into a semiconductor material; (b) efficient transport of spin-polarized carriers across the semiconductor, i.e., sufficiently long spin lifetimes; (c) effective means for control and manipulation of spin according to the desired functionality; (d) effective detection of the performed function on the spin-polarized carriers [37]-[39]. Efficient spin injection has been the major obstacle to the implementation of spintronics. Many attempts to use ferromagnetic metal contacts to inject spin-polarized carriers into

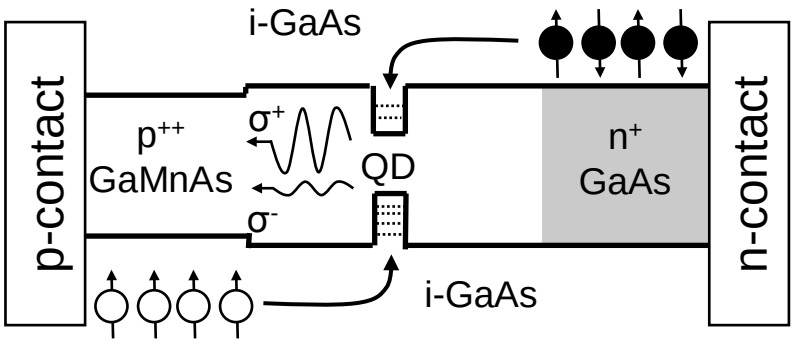

Fig. 1.3: Schematic of spin-polarized light emitting diode with quantum dot active region. The ferromagnetic GaMnAs p-contact layer and spin-aligner injects holes with preferred spin-up orientation into the quantum dots. According to quantum selection rules for quantum dot states, the intensity of the right-circular polarization light (σ^+) is much higher than the left-circular polarization (σ^-).

semiconductors have yielded little or no polarization due to large differences in the number and energy of carriers at the metal/semiconductor interface [40]. The successful growth of diluted magnetic semiconductors has been a breakthrough in the development of spintronic devices [41]. Magnetic properties of GaMnAs and InMnAs heterostructures are presented and discussed in Chapter VII.

In Chapter VIII, the characteristics of spin-polarized LEDs with quantum dot active regions and GaMnAs spin injector layers is presented. The spin-polarized LED, shown in Fig. 1.3 and described in the caption, is not only a means of detecting and studying the efficiency of spin-polarized carrier injection and transport in semiconductors, but is also a first step towards demonstrating spin-polarized lasers for future spintronic-based optical fiber communication. As will be discussed in Chapter VIII, QDs have been chosen as the active region, rather than QWs due to: (a) increased spin decoherence of holes in QWs; (b) longer spin relaxation times in QDs; (c) the interband ground-state transition energy

of QDs is considerably smaller than the bandgap of the GaMnAs aligner and therefore, despite the Zeeman splitting in this layer, field induced dichroism should be negligible.

1.5 Organization of This Thesis

The outline of the present thesis is summarized in Fig. 1.4. After the present Introduction, Chapter II presents a background on high-performance QD lasers and functions as an opening to the subsequent four chapters. The chapter begins with a review of QD lasers theory and epitaxial growth of self-organized (or self-assembled) 1.0-1.3 μm In(Ga)As QDs by MBE. This is followed by a discussion on the factors that limit high performance of conventional QD lasers in terms of their single-mode output spectrum, high speed modulation and high characteristic temperature. DFB mechanism, tunnel injection, and p-doping are recognized as solutions to these unique problems. These three types of advanced heterostructure QD lasers are the subjects of Chapters III-VI.

Chapter III presents the characteristics of 1.0 μm QD loss-coupled DFB lasers. Single-mode operation with a high side-mode suppression ratio and decreased temperature dependence of the lasing mode is demonstrated. However, similar to conventional QD Fabry-Perot lasers, the modulation bandwidth is limited to 5-6 GHz.

Chapter IV presents the static characteristics of 1.1 and 1.3 μm p-doped QD lasers. Infinite characteristic temperature, i.e., complete temperature insensitivity of the threshold current around and above room temperature, is observed for the first time in any semiconductor laser in the 1.3 μm p-doped QD lasers. Increase of characteristic temperature and threshold current upon p-doping is explained through a self-consistent model that calculates different components of threshold current in p-doped lasers.

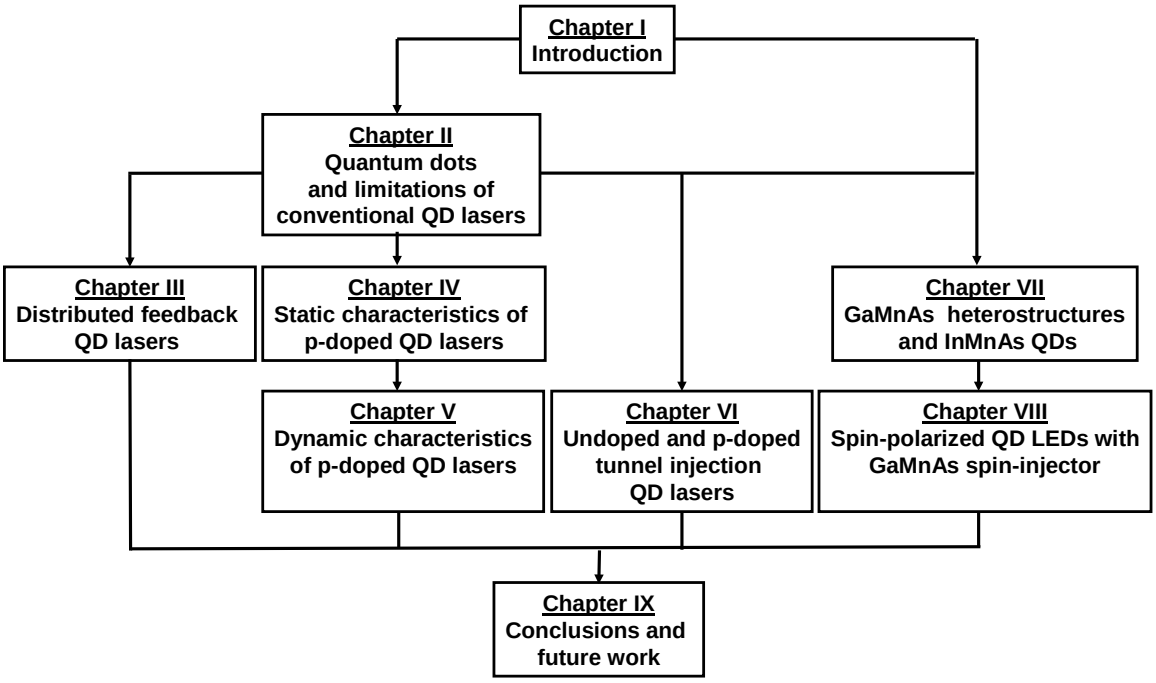

Fig. 1.4: Block diagram showing the outline of this thesis.

Chapter V focuses on the small-signal modulation bandwidth and other dynamic properties of the same lasers discussed in Chapter IV. Despite previous theoretical predications, only slight improvement of the modulation bandwidth (2-4 GHz) is observed which is explained by calculating the gain and differential gain from the DC model of Chapter IV and appropriate rate equations for p-doped QD lasers.

Chapter VI discusses the high performance characteristics of undoped and p-doped TI 1.1 μm QD lasers. After a review of the DC and small-signal modulation properties of undoped TI lasers, measurements on the linewidth enhancement factor, chirp and near-field beam pattern of these lasers are presented and compared with otherwise identical quantum well lasers. Characteristics of p-doped TI-QD lasers are the subject of the final

sections in Chapter VI. It will be seen that these lasers have static and dynamic properties matching or surpassing those of commercial QW lasers. These include: ~25 GHz modulation bandwidth, which is the highest value in any quantum dot laser; zero linewidth enhancement factor and negligible chirp; and modal gain as high as 19 cm^{-1} per dot layer.

Chapter VII begins with a review on the origin of ferromagnetism in GaMnAs, followed by its MBE growth and magnetic properties of as-grown and annealed bulk, thin layers and multilayers of its GaAs-based heterostructures. Epitaxial growth and magnetic properties of InMnAs QDs with Curie temperatures above room temperature are also presented. Chapter VIII presents the characteristics of spin-polarized 1.0 μm QD LEDs with GaMnAs spin injector layers which exhibit record high temperature and output polarization operation. Chapter IX summarizes the main conclusions of the thesis with some suggested future works.

CHAPTER II

HIGH-PERFORMANCE QUANTUM DOT LASERS

2.1 Introduction

As discussed in Section 1.2, due to near-singular density of states, self-assembled quantum dot lasers have long been envisioned as promising devices for high-performance light source applications. Self-organized QD lasers have been the subject of extensive study in the last decade and have demonstrated lower threshold current, linewidth enhancement factor and dynamic chirp than quantum well (QW) lasers [26],[28],[29]. However, there are still certain problems and challenges in achieving high-performance QD lasers. First, due to inhomogenous linewidth broadening of QDs luminescence single mode operation cannot be achieved in Fabry-Perot lasers. This problem can be eliminated in distributed feedback lasers, which are the subject of Chapter III. Furthermore, demonstration of high-speed QD lasers is another challenge, but realization of such devices may be considered a major breakthrough due to their potential application as coherent light sources for 1.0-1.3 μm short-haul local area network and metropolitan area network 10 Gb/s communication systems. However, achieving high modulation bandwidths with conventional separate confinement heterostructure (SCH) quantum dot lasers has not been possible [24]. There are unique problems that limit the modulation performance of conventional SCH QD lasers as compared to what is expected from an

ideal QD laser with discrete density of states. SCH QD lasers suffer from significant hot-carrier effects and associated gain compression due to the large density of states for the wetting layer and barrier states as compared with QDs [42]. As a result, the conventional devices cannot be modulated at bandwidths above 6-8 GHz [24]. In addition, the hole distribution is thermally broadened into many available states with small energy spacing in QDs, and a large injected hole density is required for a large gain in the ground state. This would also decrease the attainable gain and differential gain in conventional QD lasers.

Two unique solutions have been proposed and implemented to overcome these problems in conventional SCH QD lasers: tunneling injection (TI) and acceptor (p) doping of the dots [43]-[46]. With p-doping, extra holes are provided at the ground state energy by either direct doping of the dots or by modulation doping in the GaAs barriers. These extra holes ensure population inversion with less injected holes from the contacts. Consequently, the electron population in the dots and their leakage into barrier and waveguide layers is reduced as well. Chapter IV and V focus on the static and dynamic characteristics of p-doped QD lasers. In the tunnel injection scheme, *cold carriers* are injected directly into the ground state of the QDs by phonon-assisted tunneling from an adjacent injector layer and are removed by stimulated emission at approximately the same rate. Therefore, the differential gain of the lasers can be optimized and hot carrier effects are minimized. Characteristics of tunnel injection lasers are the subject of Chapter VI.

The purpose of the present Chapter is to function as an introduction to Chapters IV, V, and VI by elaborating upon the aforementioned unique problems in QD lasers. First, a

review of the self-assembled growth of QDs by molecular beam epitaxy is presented. I will then describe the intrinsic characteristics of QD lasers that determine the small-signal modulation bandwidth and the temperature dependence of the threshold current in Section 3.3. This is followed by a description of tunnel injection and p-doping in QD lasers in Section 3.4. Upon observing the results in Chapters IV-VI, we will see that although p-doping is helpful in improving the characteristic temperature, T_0, of QD lasers - especially at 1.3 μm - it does not help in realizing high modulation bandwidth lasers. On the other hand, tunnel injection not only decreases the temperature sensitivity of QD lasers, but also significantly enhances the high frequency response of the devices. It will be evident that present high-speed QD lasers are promising candidates for applications in MAN and LAN systems.

2.2 Theory of Quantum Dot Lasers

Quantum dots are three-dimensionally (3-D) confined semiconductor heterostructures. Stimulated emission of light from confined carriers in QDs can therefore be achieved if the dots serve as the optical gain medium in a separate confined heterostructure laser cavity. In order to develop a theory of static characteristics of QD lasers, the density of states (DOS), optical gain, threshold condition, and threshold current components need to be addressed, as follows.

An ideal QD is virtually an *artificial atom* with a discrete energy spectrum. In the effective mass approximation, the energy levels, E, are obtained from the eigenvalues of Schrödinger's wave equation:

$$\left[\frac{\mathbf{p}^2}{2m^*} + V(x,y,z)\right]\psi(x,y,z) = E\psi(x,y,z), \qquad (2.1)$$

where $\mathbf{p} = -i\hbar\nabla$ is the momentum operator. ψ and m^* are the carrier envelope wave function and effective mass, respectively. For an ideal QD, the potential *V(x,y,z)* can be assumed to be an infinitely deep 3-D well (box) with dimensions t_x, t_y, and t_z. Consequently, the energy eigenvalues are

$$E_{l.m.n} = \frac{\hbar^2\pi^2}{2m^*}\left(\frac{l^2}{t_x^2} + \frac{m^2}{t_y^2} + \frac{n^2}{t_z^2}\right), \tag{2.2}$$

where *l,m,n*=1,2,… are the quantum numbers of the discrete energy levels. The density of states, *ρ(E)*, is the number of states per unit volume between *E* and *E+dE*. It is evident from Eqn. 2.2 that *ρ(E)* in an ideal QD is *singular* and, with spin degeneracy included, is expressed as:

$$\rho(E) = \frac{2}{V_{dot}}\sum_{l,m,n}\delta(E - E_{l,m.n}), \tag{2.3}$$

where $V_{dot}=t_x t_y t_z$ is the volume of a single dot.

It is necessary to include the photon-electron interaction in Schrödinger's wave equation in order to understand the optical gain of transitions from the conduction to the valence band. The photon-electron Hamiltonian can be included by modifying **p** to **p**+*q***A** in Eqn. 2.1, where *q* is the electron charge and $\mathbf{A}e^{i\omega t}$ is the electromagnetic wave vector potential. The result for the transition rate, W_{eh}, is the universal Fermi's golden rule in quantum mechanics [47]:

$$\begin{aligned} W_{eh} &= \frac{2\pi}{\hbar}\left|H_{eh}\right|^2\delta(E_e - E_h - \hbar\omega), \\ H_{eh} &= \left\langle \psi_h \middle| H_p(\mathbf{r}) \middle| \psi_e \right\rangle, \\ H_p(\mathbf{r}) &= \frac{q}{2m_0}A(\mathbf{r})\mathbf{e}\cdot\mathbf{p}, \end{aligned} \tag{2.4}$$

where $H_p(\mathbf{r})$ is the perturbation Hamiltonian of the electron-photon interaction, **r** is the position vector, and **e** is the polarization of **A**. W_{eh} is for the transition of a single electron-hole pair residing in the E_e and E_h energy levels, respectively. In order to obtain the total interband transition per unit volume, W_{ij}, the DOS and the respective Fermi-Dirac distributions of electrons and holes, f_n and f_p, have to be accounted for:

$$W_{ij} = \frac{2}{V_{dot}} \sum_{i,j} \frac{2\pi}{\hbar} \left| H_{eh} \right|^2 \delta(E_e^i - E_h^j - \hbar\omega) f_n(E_e^i) \left(1 - f_p(E_h^j)\right), \qquad (2.5)$$

where $i=\{l_e,m_e,n_e\}$ and $i=\{l_h,m_h,n_h\}$ denote the eigenstates of electrons and holes, respectively. It is evident from the discrete DOS in Eqn. 2.3 that W_{ij} in QDs is independent of **k** wavevector, i.e., there is no need to introduce the concept of *reduced* DOS and integrate the transition rate over **k**-space as it is done for quantum well and bulk materials. It is also noteworthy that employing the Fermi-Dirac distribution is only valid at temperatures above 150 K, where the thermal distribution of carriers is near equilibrium. At lower temperatures, non-equilibrium distributions amongst the isolated dots have been developed [48],[49]. Also, $\left|H_{eh}\right|^2 = (qA/2m_0)^2 \left|M_{ij}\right|^2$ can be expressed in terms of the transition matrix element $\left|M_{ij}\right|^2$ which accounts for the quantum-mechanical selection rules [47]. Finally, the material gain in QDs can be expressed as:

$$g_{mat}(\hbar\omega) = \frac{2}{V_{dot}} \frac{\pi q^2}{\varepsilon_0 c n_r m_0^2 \omega} \sum_{i,j} \left|M_{ij}\right|^2 \delta(E_e^i - E_h^j - \hbar\omega) \left(f_n(E_e^i) - f_p(E_h^j)\right), \qquad (2.6)$$

where n_r is the refractive index. The last equation expresses the main advantage of QD lasers over quantum well and double heterostructure lasers. The material gain is not only discrete but is also temperature independent. Therefore, lasers with infinite characteristic

temperature are readily predicted. The ultra-narrow linewidth of lasers with such discrete gain spectrum resembles the optical spectrum of atomic lasers.

In reality, however, there are finite homogenous and inhomogenous linewidths associated with the QD states. To include the spectral broadening, the above gain expression must be convolved with some spectral lineshape function. The Lorentzian distribution can represent the homogenous linewidth broadening. However, as discussed in the next section, in self-assembled QDs there is normally a 40-60 meV inhomogenous linewidth associated with the luminescence spectrum due to a stochastic size distribution of the dot ensemble. Since inhomogenous broadening usually dominates the homogenous broadening, a Gaussian function with an energy spectral width, σ_E, is a better distribution for self-assembled QDs [50]. In this case, Eqn. 2.6 is modified to as follows:

$$g_{mat}(\hbar\omega) = \frac{2}{V_{dot}} \frac{\pi e^2}{\varepsilon_0 c n_r m_0^2 \omega} \sum_{i,j} \left|M_{ij}\right|^2 G(\hbar\omega, E_{ij}, \sigma_E)\left(f_n(E_e^i) - f_p(E_h^j)\right),$$
$$G(\hbar\omega, E_{ij}, \sigma_E) = \frac{1}{\sigma_E \sqrt{2\pi}} \exp\left(-\frac{(\hbar\omega - E_e^i + E_h^j}{2\sigma_E^2}\right). \tag{2.7}$$

If lasers with uniform dots limited by homogenous broadening are achieved, the Gaussian distribution, *G*, should be replaced with the Lorentzian function:

$$L(\hbar\omega, E_{ij}, \tau_{phase}) = \frac{1}{\pi} \frac{\hbar/\tau_{phase}}{(E_{ij} - \hbar\omega)^2 + (\hbar/\tau_{phase})^2}, \tag{2.8}$$

where the phase decoherence time, τ_{phase}, accounts for all mechanisms causing loss of coherence between the electromagnetic and carriers wavefunctions.

Furthermore, in near-pyramidal self-organized QDs, the assumption of an infinitely-deep 3-D potential leading to Eqn. 2.2 is not valid. Different approaches such as effective mass, perturbation effective mass, and pseudopotential theory can be used as better

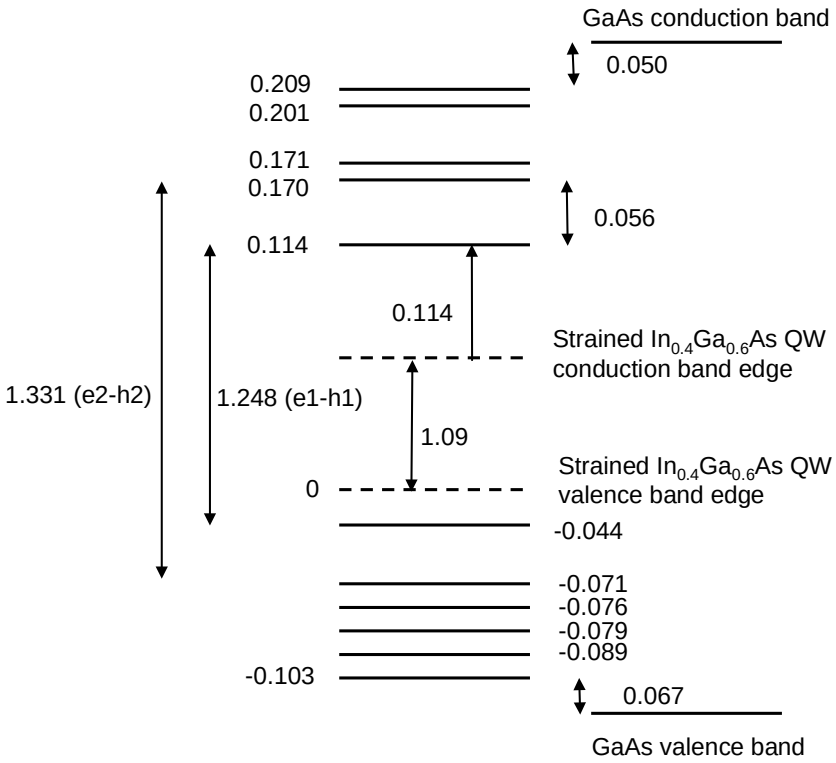

Fig. 2.1: The calculated energy levels of an $In_{0.40}Ga_{0.60}As/GaAs$ pyramidal-shape quantum dot with a base width of 124 Å and height of 62 Å, calculated by eight-band **k.p** model (reproduced from Ref. [53]).

approximations, but the most accurate method to calculate the bandstructure of strained In(Ga)As/GaAs QDs is eight-band **k.p** method after calculating the strain distribution from the valence force-field model [51]-[53]. The details of such calculations are beyond the scope of this thesis, but calculated energy levels for a typical $In_{0.40}Ga_{0.60}As/GaAs$ dot are reproduced in Fig 2.1 [53]. It is observed that the energy levels remain discrete, thus the theory presented in Eqns. 2.3-2.7 are generally valid, if the appropriate values of E_e^i and E_h^j are selected. An interesting feature of the calculated energy levels by **k.p** method is the observed near double degeneracy of the first and second excited states due to time-reflection symmetry of different $[110]$ and $[1\bar{1}0]$ exciton directions [51]. This

degeneracy is on top of the aforementioned spin-degeneracy and has to accounted for in Eqn. 2.7.

The threshold condition for lasing in QD lasers is similar to other types of semiconductor lasers, i.e., when the change in the intensity of the light undergoing a roundtrip within the cavity with an optical gain, $g=\Gamma g_{mat}$, overcomes the cavity loss, γ, and mirror losses as expressed by:

$$\Gamma g_{mat}^{th} = \gamma + \frac{1}{2l}\ln\left(\frac{1}{R_1 R_2}\right). \qquad (2.9)$$

R_1 and R_2 are the facet reflectivities and l is the laser cavity length. $\Gamma=\Gamma_z\Gamma_{xy}$ is the optical confinement factor of the active region with respect to the vertical confinement factor, Γ_z, and the in-plane areal fill factor of the ensemble of dots, Γ_{xy}.

In order to calculate the threshold current component due to recombination in the dots, the spontaneous recombination rate per volume per unit of energy needs to be calculated by multiplying the rate W_{ij} in Eqn. 2.5 by the number of optical modes in the differential energy range, i.e.,

$$R_{sp}^{QD}(\hbar\omega) = \frac{2}{\hbar\omega V_{dot}}\sum_{i,j}\left|M_{ave}\right|^2 G(\hbar\omega, E_{ij}, \sigma_E)\rho_{opt}(\hbar\omega) f_n(1-f_p). \qquad (2.10)$$

$\left|M_{ave}\right|^2$ is the optical matrix element averaged over the three polarizations along x, y, and z axes. The optical mode density, $\rho_{opt}(\hbar\omega)$, is given by [47]:

$$\rho_{opt}(\hbar\omega) = \frac{n_r^3}{\pi^2(\hbar c)^3}(\hbar\omega)^2. \qquad (2.11)$$

The threshold current density due to QD recombination per dot layer is expressed as:

$$J_{QD} = qd_{eff}\int R_{sp}^{QD}(\hbar\omega)d(\hbar\omega), \qquad (2.12)$$

where $d_{eff} = V_{dot}\,\rho_{dot}$ and ρ_{dot} is the areal density of the dots. Eqn. 2.12 is still strongly temperature independent, but in reality it is not the only term contributing to the threshold current. As will be discussed in the next section, In(Ga)As QDs are grown on GaAs buffer/barrier layers and the dots are formed on top of a wetting layer in the Stranski-Krastanow mode. The wetting layer can be modeled as a two-dimensional electron gas [42]. Therefore, radiative recombination in the GaAs layers, J_{GaAs}, and the wetting layer, J_{WL}, are also significant 2-D and 3-D temperature-dependent factors at high temperatures which increase the threshold current and reduce the characteristic temperature of QD lasers. J_{GaAs} and J_{WL} are calculated with expressions similar to Eqn. 2.12 with the corresponding 2-D and 3-D reduced densities of states [47].

2.3 Molecular Beam Epitaxial Growth of Quantum Dots

Significant improvement in the performance of optoelectronic devices - especially semiconductor lasers – with quantum dot active region was proposed theoretically in the early 1980's [14]. However, fabricating these three-dimensionally confined heterostructures was a technological challenge for about a decade. Some of the attempted fabricating techniques include: laterally pattering quantum wells by e-beam lithography followed by wet or dry etching, regrowth of epitaxial layers, selective growth on patterned substrates and cleaved-edge overgrowth [54]-[57]. QD lasers were demonstrated for the first time by e-beam and etching techniques, but with very high threshold currents [15]. All of the above-mentioned fabrication techniques suffer from problems such as extremely high heterointerface recombination, impurity contamination and defect formation, thus the fabricated QDs have no or poor optical quality.

Self-assembled formation of islands (quantum dots) during epitaxial growth is a natural process that eliminates all of the above problems and, therefore, high-quality confined heterostructures can serve as the gain medium of semiconductor lasers. Surface roughness in InGaAs/GaAs islands grown in the Stranski-Krastanow mode, as discussed below, was observed and evaluated by several groups in the 1980's [58]-[60], but it was not recognized as a means of self-forming QDs until later, when both metal-organic chemical vapor deposition (MOCVD), and molecular beam epitaxy (MBE) were employed to grow self-assembled QDs [61],[62]. MBE is more advantageous than MOCVD, at least for fundamental research, since MBE can produce high quality materials with abrupt interfaces and provide precise (monolayer) control over thickness and the possibility of *in situ* monitoring by techniques such as reflection high-energy electron diffraction (RHEED).

In general, depending on the lattice mismatch between the substrate and the grown material, three distinct modes may occur, which are named after pioneering researchers during the 1920-50's, who developed the thermodynamic conditions for these different regimes [63]-[65]. They are schematically shown in Fig. 2.2 and can be described as follows:

(a) Frank-van der Merwe (FM) mode: there is zero or very small lattice mismatch and the epitaxial growth proceeds layer-by-layer;

(b) Volmer-Weber (VW) mode: the lattice mismatch is more than ~12% and three-dimensional islands are formed directly on the matrix (substrate);

(c) Stranski-Krastanow (SK) mode: this is an intermediate regime between the FM and VW modes, where initially several monolayers (called the wetting layer) are

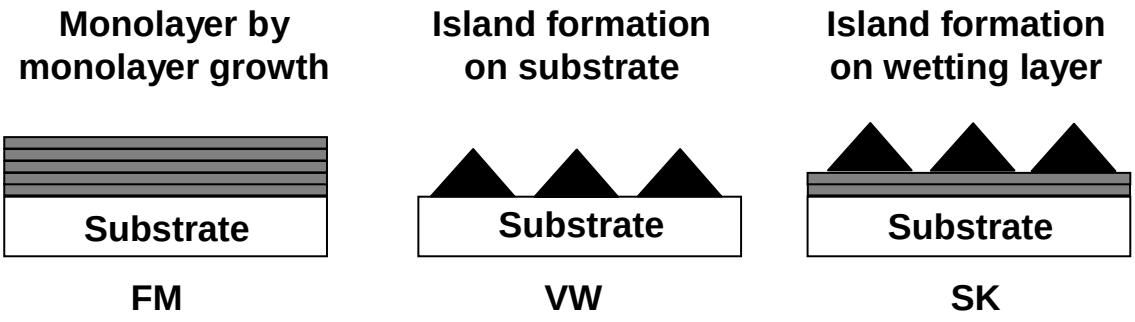

Fig 2.2: Three growth modes on a substrate: (a) Frank-van der Merwe (FM); (b) Volmer-Weber (VW); (c) Stranski-Krastanow (SK). The thin, gray layers represent one monolayer of deposition.

grown layer-by-layer, followed by the formation of three-dimensional islands (quantum dots).

Thermodynamically, in the VW and SK modes, after a critical amount of growth of strained material, a morphological instability results in the formation of strained islands. This island formation leads to a reduction of the strain energy and an increase in the surface energy as compared to the FM mode. The strain energy is proportional to the dot volume and the surface energy is proportional to the area of the QD. In the SK mode, if the size of the QD exceeds a critical value, island formation is energetically favorable and the islands are formed on the wetting layer.

In(Ga)As/GaAs QDs can be grown by MBE with precise control of temperature, and deposition rate of In, Ga, and As from heated solid sources. The QDs are typically grown at temperatures lower (from 480-530°C) than the standard GaAs growth in order to avoid problems associated with surface migration of In adatoms. The flux of As_4 is kept at least one order of magnitude higher than the group III elements fluxes. The electronic bandstructure of In(Ga)As QDs was discussed in the previous section (Fig. 2.1). Typically, these QDs have a ground state transition from ~ 950 to ~ 1400 nm,

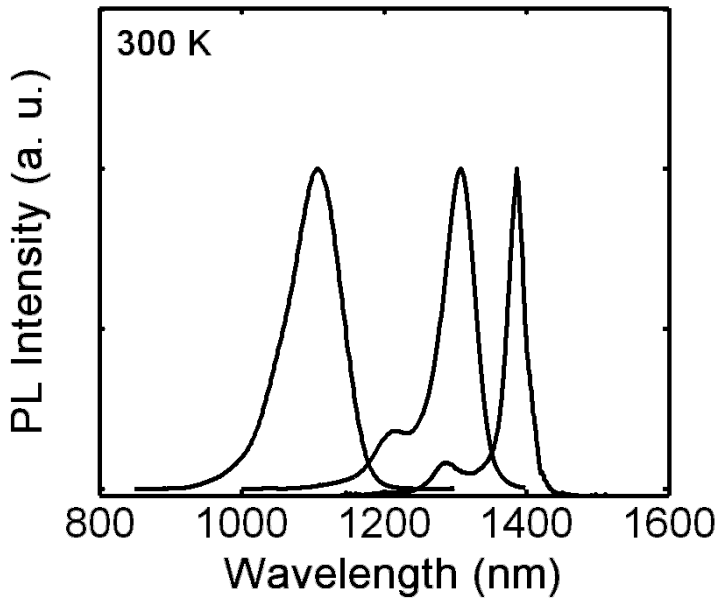

Fig. 2.3: Room-temperature photoluminescence spectra of three quantum dot samples with ground state transitions at 1100, 1320, and 1400 nm.

depending on the composition, number of deposited monolayers and growth rate of $In_xGa_{1-x}As$, as well as the choice of material that is used to cap the dots. Measured photoluminescence spectra of three samples with different peak wavelengths of the ground transition are presented in Fig. 2.3. Two types of QDs, 1.0-1.1 μm and 1.3 μm QDs, are mainly discussed in this work. 1.0-1.1 μm QDs are achieved by growing $In_xGa_{1-x}As$ with $0.4<x<0.5$ at a rate of 0.25 monolayers per second (ML/s), where the wetting layer thickness is ~5-6 ML and the dots are formed after the deposition of 1-2 MLs of $In_xGa_{1-x}As$. InAs is the material of choice for growing QDs with ground state transition at about 1.3 μm. The wetting layer is ~1.8 ML in this case and the InAs dots are capped with ~40Å-thick $In_{0.15}Ga_{0.85}As$. Self-assembled QDs have near pyramidal shapes, as the high-resolution cross-sectional transmission electron microscopy (XTEM) image in Fig. 2.4(a) shows for $In_{0.40}Ga_{0.60}As$ QDs. A single pyramid has a base length of 15-

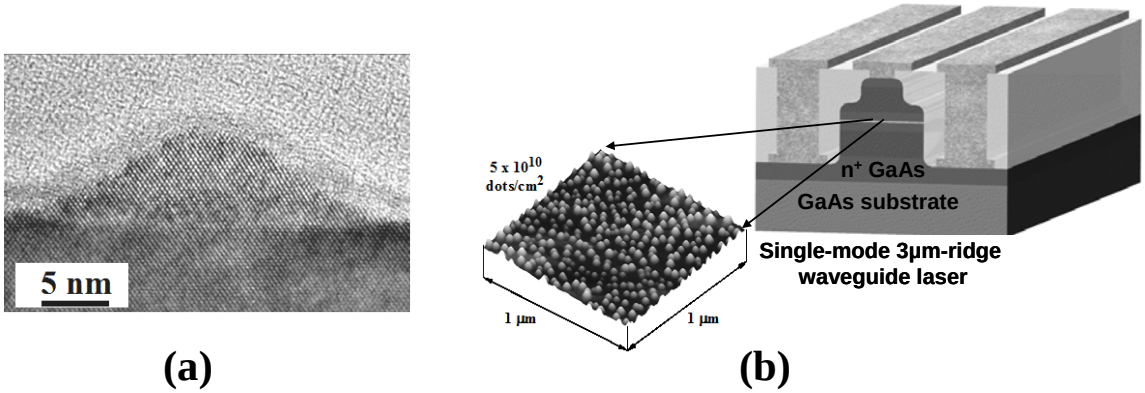

Fig 2.4: (a) High-resolution cross-sectional transmission electron microscopy (XTEM) image of a pyramidal $In_{0.40}Ga_{0.60}As$ quantum dot (obtained in collaboration with Y. Lei at Argonne National Laboratory, Argonne, IL); (b) schematic of the single-mode ridge waveguide quantum dot lasers fabricated throughout this work with ground-signal-ground contacts, also showing an atomic force microscopy (AFM) image of $In_{0.40}Ga_{0.60}As$ quantum dots.

20 nm and a height of 6-9 nm. As can be seen in the atomic force microscopy image of Fig. 2.4(b), a typical density for self-assembled QDs is ~5×10^{10} dots/cm^2. It is noteworthy that 1.3 μm QDs are larger in size and usually have lower dot density and consequently lower optical gain for laser applications.

Finally, as depicted in Fig 2.4(b), ridge waveguide lasers with a QD active region can be grown and fabricated by standard lithography, wet and dry etching, metallization and passivation techniques. The exact processing recipe for single-mode ridge waveguide laser fabrication is presented in the Appendix of this thesis.

2.4 Factors Limiting High-Speed Operation of Conventional QD Lasers

Low modulation bandwidth was theoretically predicted in QD lasers and attributed to the *phonon bottleneck* [66] long before the first experimental reports on the small-signal modulation response of the lasers [24]. It was argued that since the energy separation of the ground and first excited state in QDs (see Fig. 2.5) is typically larger

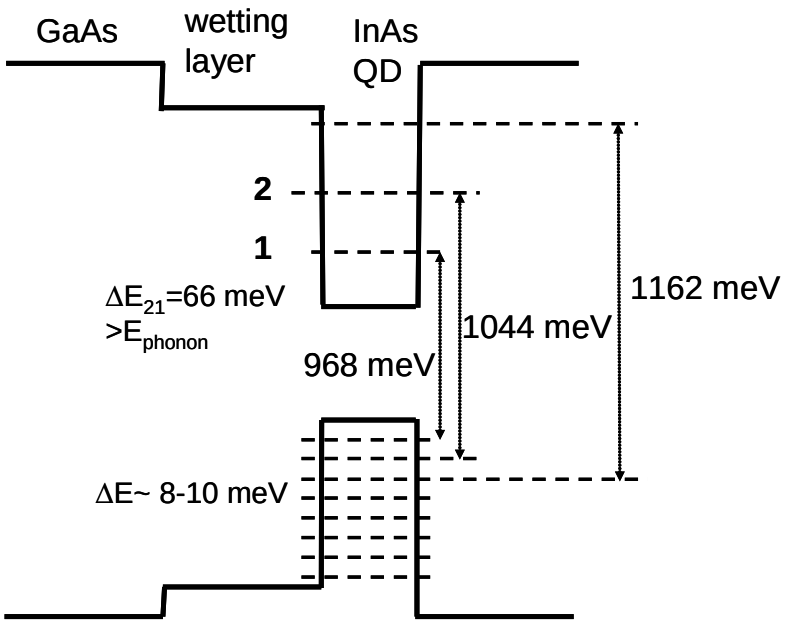

Fig. 2.5: Energy levels of 1.3 μm quantum dots showing the large energy spacing between the ground and first excited state in the conduction band and many (~10) levels with small spacing (8-10 meV) in the valence band.

than the optical phonon energy (~36 meV), single-phonon-assisted scattering (relaxation) into the ground state is forbidden, and since multiple-phonon scattering is a very unlikely slow process, QD lasers should suffer from this phonon bottleneck, resulting in low modulation bandwidths. The phonon bottleneck was indeed observed by time-resolved differential transmission spectroscopy (DTS) where non-geminate carriers are not captured in the same dot, which can only happen at very low levels of injection [67]. However, similar three-pulse DTS measurements showed very fast (~130 fs) gain recovery of the ground state of QDs at high levels of injection (lasing conditions) [68], which is due to strong carrier-carrier scattering in geminate captures and provide an indication that a bottleneck other than the slow phonon-carrier interaction has to responsible for the low speed of QD lasers.

It is now recognized that the limitations to high-speed modulation of conventional SCH QD lasers is due to the electronic properties of the quantum dots arising from the nature of self-assembled growth. As discussed before, in the Stranski-Krastanow growth mode, zero-dimensional islands (QDs) are formed on top of a wetting layer (Figs. 2.2 and 2.5), which can be treated as a 2-D electron-gas). The QDs and the wetting layer form a coupled electronic system, whose statistics cannot be described by quasi-Fermi equilibrium at high biases. Due to the large number of the states in the 2-D electron-gas as compared to the number of states in the dots, injected carriers predominately reside in the higher energy states in the wetting layer. Consequently, QD lasers suffer from this undesired *hot carrier* effect and associated gain saturation. DTS measurements have indeed shown that electrons captured in the wetting layer/barrier states tend to remain there at temperatures above 180 K, i.e., they undergo very slow relaxation to the lasing energy state [69]. Matthews *et al.* [42] also observed severe gain saturation in QDs at temperatures above 150 K and showed that it can be explained by incomplete population inversion in the ground state of the QDs due to the occupancy of the wetting layer states. The gain saturation leads to low modulation bandwidth. Stated differently, the entropy change of carriers relaxing from the two-dimensional wetting layer states to the zero-dimensional QDs is responsible for the low modulation bandwidths measured in QD lasers [70].

Furthermore, an ideal QD laser should preferably have only one electron and one hole energy level. Due to strong anisotropy and band mixing, there is a multiplicity of hole states and the energy spacing between these states is very small. As shown in Fig. 2.5, the inevitable existence of multiple hole energy levels with small energy spacing (8-

10 meV) results in thermal broadening of the hole population in energy. Consequently, the ground state hole population is depleted, leading to a decrease in gain. Higher injection of holes, to compensate for this effect, necessitates increased injection of electrons due to charge neutrality requirements. The excess carriers lead to leakage, non-radiative recombination outside the core, increased threshold current and reduced differential gain.

2.5 Tunnel Injection and Acceptor Doping in Quantum Dot Lasers

Tunneling injection and p-doping have been suggested and studied as two promising techniques to solve the hot-carrier related problems in QD lasers [43]-[46]. Tunnel injection was originally proposed and demonstrated more than a decade ago to reduce hot carrier effects in quantum well lasers [71]-[73]. In this scheme, *cold carriers* are directly injected into the lasing energy state from an adjoining injector layer, thus hot carrier effects can be bypassed and the performance of the lasers would improve. High-performance GaAs- and InP-based quantum well lasers with high T_0, reduced chirp and improved modulation bandwidths have been reported [72],[73]. Tunneling injection, however, is more useful for enhancing the modulation bandwidth of quantum dot lasers. As shown in Fig. 2.6(a), cold electrons injected into the ground state of the QDs by phonon-assisted tunneling can bypass the hot carrier problems associated with the capture of electrons into the wetting layer/barrier energy states. Femtosecond DTS measurement of phonon-assisted tunneling confirms fast (~1.7 ps) temperature-independent tunneling times [74]. Tunneling injection also decreases carrier radiative recombination in the wetting layer/barrier regions, prompting Asryan and Luryi's theoretical prediction of a

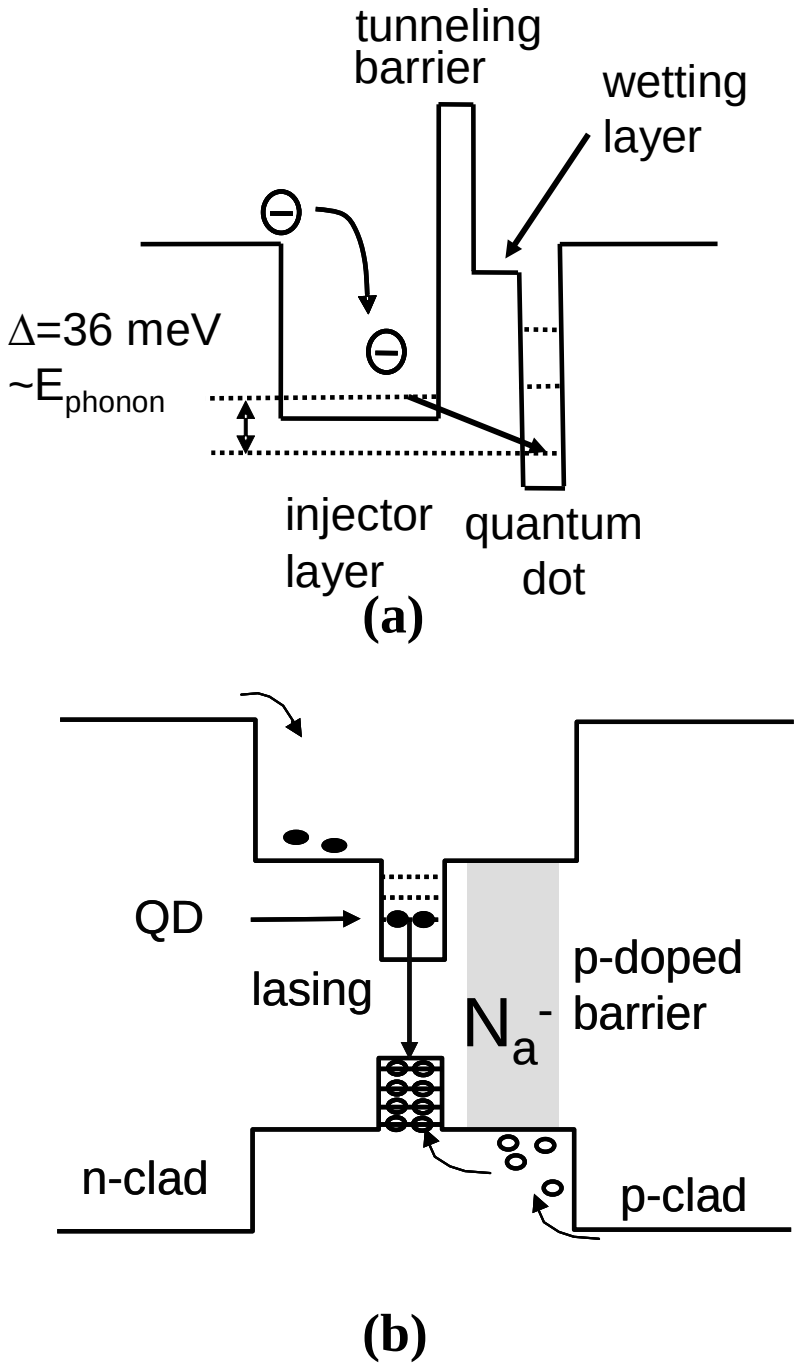

Fig. 2.6: (a) Injection of cold carriers into the ground state of the dot by tunneling from an adjoining injector layer; (b) modulation p-doping of the quantum dot barrier in order to increase the gain through the increase of hole ground state occupancy.

significant increase of T_0 [43]. A large increase in modulation bandwidth (~15 GHz) was demonstrated in the first tunnel injection QD lasers [44] and, as will be seen in Chapter VI, the characteristics of our lasers have steadily improved since then [74]-[78].

In the p-doping scheme, the thermally broadened hole distribution is compensated by providing extra holes. P-doping of QD lasers can be achieved by either direct or modulation doping of the dots. As shown in Fig. 2.6(b) for the modulation doping case, the holes of the p-doped barrier are transferred into the hole ground state with lower energy in the adjacent QD layer, thus fewer electron-hole pairs are required to be injected from the contacts to compensate for the thermal broadening of the hole distribution. This would decrease f_p, leading to a gain increase from Eqn. 2.7. Vahala and Zah [79] predicted an increase of gain in p-doped QW lasers, which was followed by the prediction of relaxation oscillation frequency enhancement and reduction of linewidth enhancement factor in multi-quantum-well lasers [80]. P-doping is expected to be more beneficial in QD lasers due to the more pronounced thermal broadening of holes in the valence band with smaller energy spacing in QDs than in QWs.

Miyamoto *et al.* [45] proposed p-doping for increasing gain and reduction of threshold current. Deppe *et al.* [46],[81],[82] have modeled the impact of p-doping on the modulation response and characteristic temperature, T_0, of QD lasers and have experimentally demonstrated T_0 as high as 213 K in p-doped InAs QD lasers. There are also theoretical studies on the excitonic effects of p-doping on T_0 of p-doped InAs/GaAs QD lasers [83], as well as the role of the wetting layer in limiting the gain of p-doped InP-based 1.55 μm quantum dash lasers [84]. As will be discussed in more detail in Chapter IV, we have measured temperature invariant operation ($T_0=\infty$) of p-doped 1.3

μm QD SCH lasers and have attributed this result to a significant role of Auger recombination and its unique temperature dependence [77],[85]. However, contrary to previous theoretical predictions [82], we observed only a slight improvement in modulation bandwidth in p-doped lasers. The low bandwidth can be attributed to the inefficiency of p-doping due to the wetting layer states [84], inadequate enhancement of gain and differential gain, and the increased damping effect of Auger recombination in the modulation response. All of these will be discussed in detail in Chapter V. These observations confirm that, although p-doping may be beneficial in enhancing T_0, tunnel injection appears to be a better approach to achieve high-speed QD lasers.

2.5 Summary

The theory of quantum dot lasers and growth of self-assembled quantum dots was reviewed. The problems related to the existence of wetting layer and hole energy multi-states in conventional quantum dot lasers were discussed. The proposed unique solutions to these special problems are tunneling injection and p-doping schemes which were explained in this chapter.

CHAPTER III

QUANTUM DOT DISTRIBUTED FEEDBACK LASERS

3.1 Introduction

Self-assembled quantum dot (QD) lasers with ultra-low threshold currents, large differential gain, low chirp and linewidth enhancement factor, and suppressed filamentation have been reported [26]-[30]. For optical communication applications, a single-mode spectral output with narrow linewidth is essential. An ideal QD Fabry-Perot laser is expected to be single-mode since the atom-like density of states should be singular. However, there is a stochastic size distribution associated with the self-assembled QDs grown by MBE. The inhomogeneous broadening of 40-60 meV in the photoluminescence and gain spectra in quantum dots makes the output spectrum of Fabry-Perot QD lasers multi-mode and unstable [86]. The distributed feedback (DFB) scheme is a well-known technique to obtain narrow linewidth single-mode lasers, and is the subject of this Chapter.

First, it should be noted that in following the epitaxy and processing steps of standard index-coupled QD DFB lasers, degradation of the active QDs was observed after etching of the grating and regrowth of the top cladding and contact layers. While the reason for this is not entirely clear, a probable cause is strain relaxation and defect formation during the high-temperature surface cleaning before regrowth and the high-

temperatures used for regrowth of these layers. On the other hand, loss-coupled DFB lasers with external lateral gratings avoid regrowth and rely on the evanescent coupling of the electromagnetic field to a metal, e.g., chromium, grating [87]. The strong absorption associated with the imaginary part of the complex refractive index of Cr results in a high coupling coefficient and compensates for the decrease of the light field in the grating regions, while the real part provides index-coupled feedback. An added advantage of loss-coupled DFB device structure is the elimination of degenerate modes around the Bragg condition, without the necessity of asymmetric tapering [88]. By progressively changing the grating parameters in an array of lasers, a multi-wavelength source can be easily obtained. Such devices with QD active regions have also been reported [89]. Here, the performance characteristics of $In_{0.40}Ga_{0.60}As$/GaAs self-organized QD loss-coupled DFB lasers with a nominal lasing wavelength of 1.0 μm are discussed.

3.2 Molecular Beam Epitaxial Growth and Fabrication

Figure 3.1 shows the QD laser heterostructure consisting of four coupled layers of $In_{0.40}Ga_{0.60}As$ QDs buried in a GaAs guide layer and surrounded by 1.0 μm $Al_{0.30}Ga_{0.70}As$ claddings. The heterostructure was grown by solid-source molecular beam epitaxy (MBE) on a (001) n-GaAs substrate, as described in Section 2.3. The QDs were grown at 520°C and the GaAs and AlGaAs layers were grown at 620 and 650°C, respectively. Room-temperature photoluminescence from the QDts exhibit a peak at 1.02 μm. After depositing 3.0 μm wide p-metal contacts, a combination of self-aligned dry and wet etching techniques were used to define mesas from approximately 0.2 μm above the active region. The etch depth was optimized to achieve the desired coupling coefficient

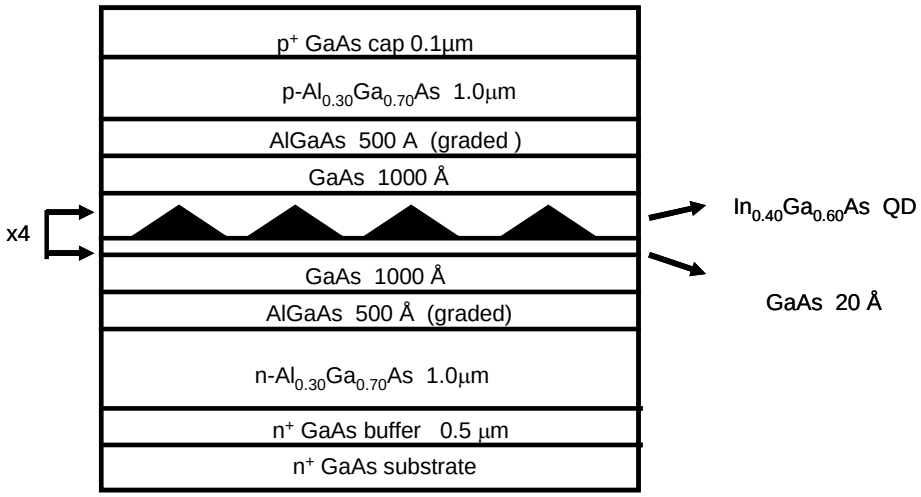

Fig. 3.1: Schematic of $In_{0.40}Ga_{0.60}As/GaAs$ quantum dot distributed feedback laser heterostructure grown by molecular beam epitaxy.

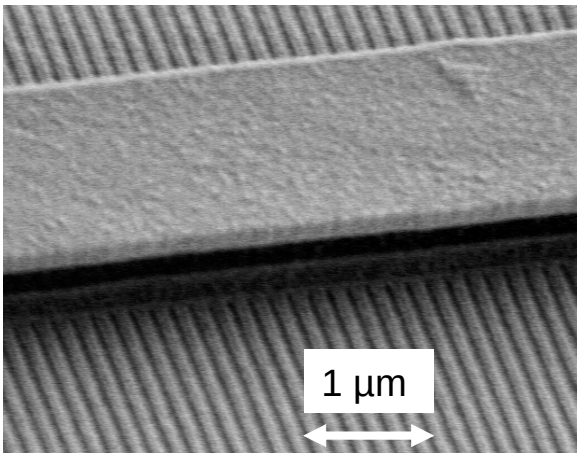

Fig. 3.2: Scanning electron microscopy image of a section of the Cr gratings and the waveguide ridge.

and optical loss in the metal grating, to be subsequently formed. Electron-beam (e-beam) lithography was used to define second order gratings with 0.3 μm period and 50% duty cycle, in order to obtain a lasing wavelength of 1.0 μm. Due to the non-planar surface of the e-beam sample, high electron energies are required to ensure the extension of the

lateral grating to the edge of the mesa. A 100 keV Leica VB6 electron beam system at Cornell University, Ithaca, NY with 1 nA beam current was used to expose and define the grating pattern on 150 nm e-beam resist. 45 nm of chromium was next evaporated and lifted off to create the metal grating. Figure 3.2 shows a scanning electron microscopy image of a section of the metal grating and ridge. Finally, single-mode ridge waveguide lasers were fabricated with standard optical lithography, wet and dry etching, silicon dioxide passivation and planarization, and contact metallization techniques, similar to the fabrication of Fabry-Perot lasers in the Appendix of this thesis. 1-mm long DFB lasers were formed and the end facets were left uncoated.

3.3 Static Characteristics

The lasers were mounted on a Peltier cooler and were biased through ground-signal-ground probes and RF cables. Light-current characteristics of the QD DFB lasers were measured under pulsed bias conditions (1μs, 10 kHz) and are presented for different temperatures in Fig. 3.3. At room temperature, the threshold current is 60 mA and the differential quantum efficiency is ~0.1 W/A. The relatively high threshold current compared to Fabry-Perot lasers is due to the loss in the optical metal grating for the long cavities used. The temperature dependence of the threshold current and the peak wavelength of the output spectrum were also measured and are presented in Fig. 3.4. An important figure of merit of semiconductor laser is the characteristic temperature, T_0, which is defined from the empirical exponential dependence of the threshold current, i.e.,

$$I_{th}(T) = I_{th}(T_0)e^{T/T_0} \qquad (3.1)$$

in a certain temperature range. From the data shown in Fig. 3.4, T_0 derived to be 64 K

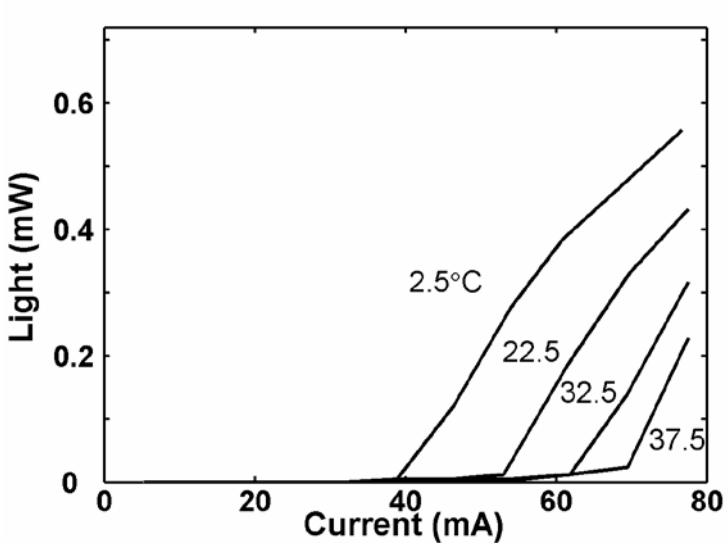

Fig. 3.3: The temperature-dependent light current characteristics of the InGaAs/GaAs quantum dot distributed feedback laser.

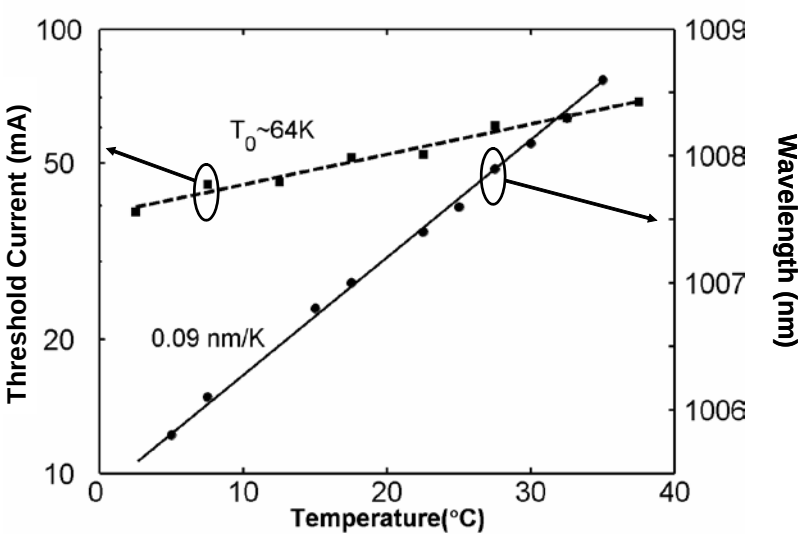

Fig. 3.4: Measured temperature dependence of the threshold current (squares) and lasing wavelength (circles) of the InGaAs/GaAs quantum dot distributed feedback laser. The dashed and solid lines are fits to the data.

around room temperature and the wavelength is found to shift linearly with a slope of 0.09 nm/K. In comparison, this shift is typically >0.25 nm/K for a Fabry-Perot QD laser [90]. Figure 3.5 depicts the room temperature output spectrum of the laser at $1.2\times I_{th}$,

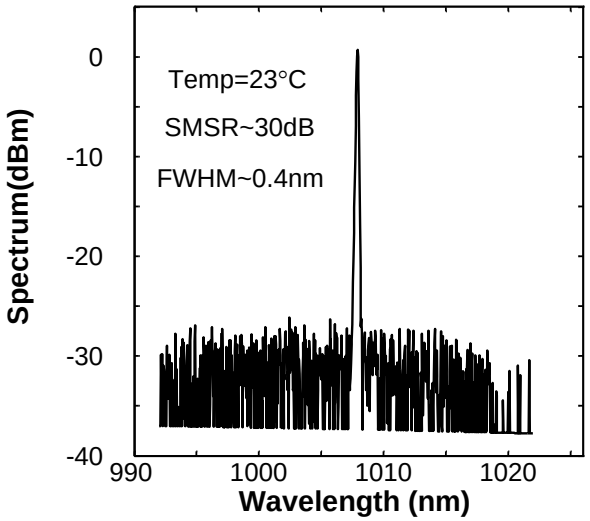

Fig. 3.5: The output spectrum of the InGaAs/GaAs quantum dot distributed feedback laser at room temperature.

measured with a HP 70952B optical spectrum analyzer. The side-mode suppression ratio is 30 dB and the linewidth (full-width at half maximum) is 4 Å. Upon comparing with Fabry-Perot QD lasers, the small shift of wavelength with temperature, high side-mode suppression ratio and the very small linewidth of the output spectrum in the present lasers are strong indications that the distributed feedback mechanism indeed functions in these lasers.

3.4 Small-Signal Characteristics

The dynamic performance of the lasers was measured with a high-speed photoreceiver, MITEQ low-noise amplifier and a HP 8593A electrical spectrum analyzer after collecting the output light with a cleaved fiber. The measurement setup is schematically shown in Fig. 3.6. The measurements were made under pulsed bias conditions similar to the static characteristics. The measured modulation response was corrected by taking into account amplifier gain and loss in the microwave cables. The

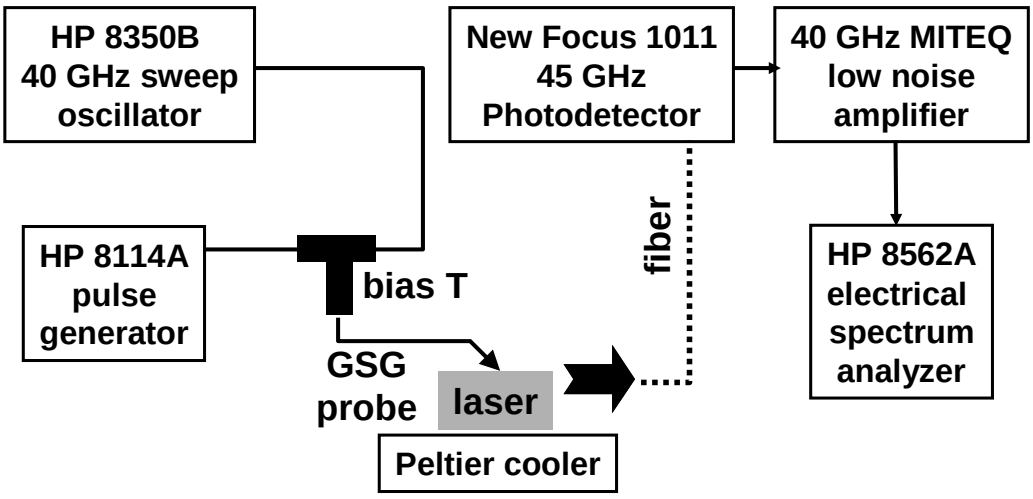

Fig 3.6: Equipment setup for measurement of modulation bandwidth of high-speed lasers.

corrected modulation response for the lasers at room-temperature and at different injection currents is shown in Fig. 3.7. The maximum 3-dB bandwidth, measured for an injection bias of 78 mA is about 5 GHz. Device heating prevented doing measurements at higher injection currents. The measured bandwidth is similar to what has been recorded for separate confinement heterostructure (SCH) Fabry-Perot ridge waveguide QD lasers [24]. As described in Section 2.4, the higher density of states in the wetting layer and barrier states of the quantum dots at room temperature and carrier heating cause a significant gain compression in quantum dot lasers [74]. Alternate techniques of carrier injection need to be employed and it has been shown that tunnel injection of electrons into the lasing quantum dots substantially alleviates such problems, which is the subject of Chapter VI.

Finally, the chirp in the DFB lasers was measured during direct modulation at room temperature by measuring the broadening of a single longitudinal mode using an optical

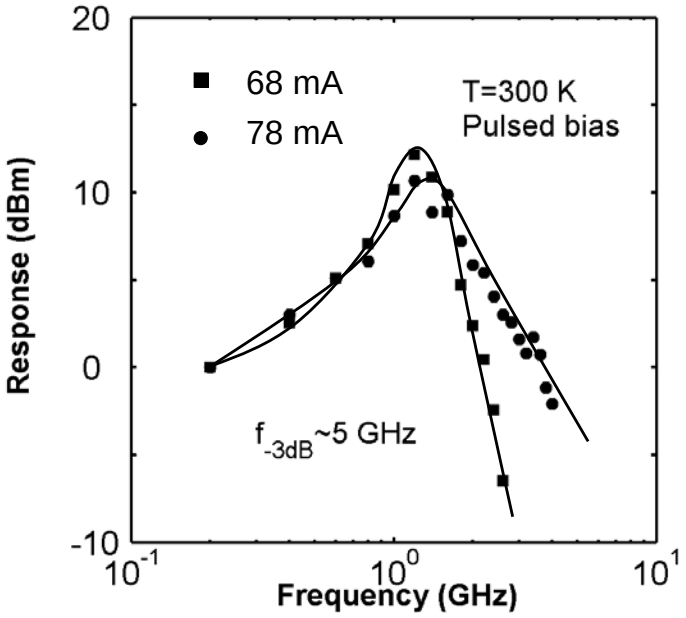

Fig. 3.7: Modulation frequency response of the quantum dot distributed feedback laser at different injection currents. Solid lines are guides to the eye.

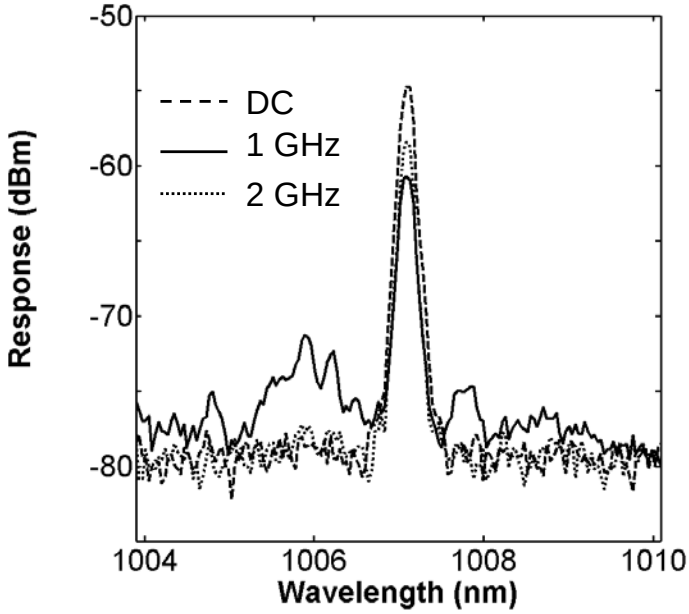

Fig. 3.8: Output optical spectrum of the quantum dot distributed feedback laser at 82 mA DC bias and 40 mA AC signal for 1.0 and 2.0 GHz modulation frequencies.

spectrum analyzer with a resolution of 0.8 Å. The measured technique and procedure is explained in more detail in Section 6.3.3. The sinusoidal modulation current was superimposed on a pulsed DC bias current. The DC bias is 82 mA , the peak-to-peak modulation current was varied from 0 to ~40 mA and the modulation frequency was varied upto 2 GHz. The measured data are shown in Fig. 3.8. No measurable chirp was observed in these devices even under large signal modulation conditions. The chirp in a semiconductor laser is directly proportional to the linewidth enhancement factor, α, which has been measured to be <1 in QD lasers [28],[29].

3.5 Summary

In summary, loss-coupled quantum dot distributed feedback lasers with chromium lateral gratings were fabricated and characterized. Single mode emission is recorded at 1.006 μm with a 30 dB side-mode suppression ratio and linewidth of 4 Å at room temperature. The differential quantum efficiency at room temperature is ~0.1 W/A and T_0 is 64 K around room temperature. The highest measured bandwidth is ~5 GHz at 300 K and it is believed that hot carrier effects and associated gain compression make it impossible to modulate these devices at higher frequencies. No measurable chirp could be recorded upto biases of ~40 mA and modulation frequency of 2 GHz.

CHAPTER IV

P-DOPED QUANTUM DOT LASERS: STATIC PROPERTIES

4.1 Introduction

As discussed in the previous Chapters, self-organized quantum dot (QD) lasers have been the subject of extensive research in the last decade and a steady improvement in their characteristics has been reported [21]-[30]. This has been brought about through a good understanding of the unique hot-carrier dynamics in QDs [74],[91] and through improved techniques of QD epitaxy [92],[93]. As described in Section 2.4, it is evident that important and unique limitations arise from the electronic structure of self-organized QDs. It is restated briefly herein that one unique characteristic which potentially limits QD laser performance is related to hole injection into the dots. As shown in Fig. 2.5, the inevitable existence of multiple hole energy levels with small energy spacing (8-10 meV) [82],[83] results in thermal broadening of the hole population in energy. Consequently, the ground state hole population is depleted, leading to a decrease in gain. A higher injection of holes to compensate for this effect necessitates increased injection of electrons due to charge neutrality requirements. The excess carriers lead to leakage, non-radiative recombination outside the core, increased threshold current and reduced differential gain. As shown in Fig. 2.6(b), a solution to this problem is offered by

intentionally providing additional holes to the dots, so that the ground state remains filled with holes [42],[82]. T_0 as high as 213 K have been measured in p-doped InAs QD lasers [46]. We have recently demonstrated temperature invariant output characteristics ($T_0=\infty$) in p-doped 1.3 μm InAs/InGaAs QD lasers, the *first* in any semiconductor laser [77],[85].

The intent in this and the next Chapters is to report our findings from experimental and theoretical studies on static and dynamic properties of p-doped 1.1 and 1.3 μm In(Ga)As/GaAs QD lasers. We have made an attempt to evaluate the true potential of acceptor doping and, in particular, to determine its impact on the high-speed characteristics of lasers. This is the first experimental study of the modulation properties of p-doped QD lasers. We present a self-consistent model of the contributing radiative and non-radiative threshold current components in order to explain the observed temperature variation of the threshold current. In what follows, Section 4.2 describes the molecular beam epitaxial growth and fabrication of the p-doped QD lasers. Section 4.3 describes the results obtained from light-current measurements. Section 4.4 presents the model for calculating threshold current components p-doped lasers. The following Chapter focuses on the small-signal modulation response and other dynamic properties of the same lasers.

4.2 Laser Growth and Fabrication of p-Doped and Undoped Lasers

First, I would acknowledge and thank Dr. Alexey Kovsh and his colleagues at NL Nanosemiconductor GmbH, Dortmund, Germany for the growth of the 1.3 μm p-doped laser heterostructures. The 1.3 μm QD laser heterostructures, shown in Fig. 4.1(a), were grown on (001) n-GaAs substrates in a solid-source molecular beam epitaxy (MBE)

reactor and consist of a 0.36 μm GaAs waveguide region, in which 10 stacks of InAs/InGaAs QD layers - separated by 33 nm thick GaAs spacers - are inserted. The waveguide region is surrounded by 1.5 μm $Al_{0.35}Ga_{0.65}As$ cladding layers doped n- and p-type with Si and Be, respectively. A 0.4 μm thick p-type GaAs contact layer is also incorporated on top. The modulation doping of the dots with holes is accomplished with a 10 nm-thick delta-doping with a C-doped layer in the GaAs waveguide region separated from the quantum dots by 14 nm. The doping concentration was varied to provide sheet acceptor concentrations per QD layer varying in the range $(0\text{-}2)\times10^{12}$ cm^{-2}. The optimum doping level was determined by studying the luminescence of the dots and the device characteristics. The room temperature photoluminescence (PL) from a laser heterostructure in which the QDs are modulation doped at 5×10^{11} cm^{-2} is shown in Fig. 4.1(b). In addition to the strong luminescence from the ground state transitions, those from the first excited states are also present. The heterostructure for the 1.1 μm lasers grown in our own laboratory is very similar, except the active region consists of 10 layers of $In_{0.5}Ga_{0.5}As$/GaAs quantum dots, separated by 30 nm GaAs barrier layers. The modulation p-doping is accomplished in this case with Be at a level of 5×10^{11} cm^{-2}.

Mesa-shaped broad area (100 μm-wide) and single-mode ridge waveguide (3-5 μm ridge width) lasers were fabricated by standard n- and p-contact metallization, photolithography, and wet and dry etching techniques, the processing recipes of which can be found in the Appendix of this thesis. Lasers of various lengths were obtained by cleaving into bars, and contact to the devices was made with high-frequency probes. Measurements were made both on devices with as-cleaved facets and with high-reflectivity facets obtained by deposition of appropriate MgF/ZnSe dielectric mirrors.

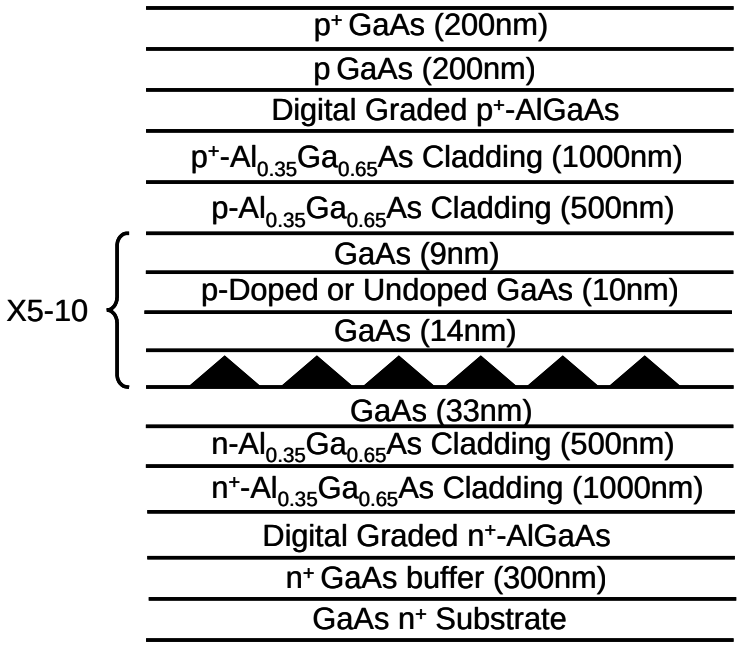

(a)

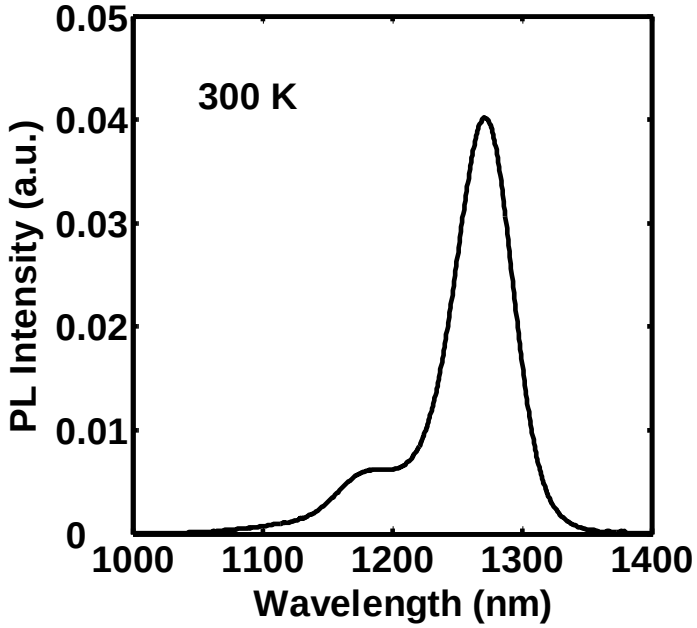

(b)

Fig. 4.1: (a) Schematic of the heterostructure of 1.3 μm p-doped and undoped self-organized quantum dot lasers grown by molecular beam epitaxy; (b) room temperature photoluminescence spectrum of the laser heterostructures with a p-doping level of 5×10^{17} cm^{-3}.

4.3 Static Characteristics

The characteristics of 1.3 μm lasers are described first. The results reported here are for p-doped lasers with an optimum sheet concentration of 5×10^{11} cm^{-2} (corresponding to 5×10^{17} cm^{-3} bulk doping) and with facet reflectivities of 95%/32%. Light-current characteristics were measured both in continuous wave (CW) and pulsed mode (1μs, 10 kHz) of biasing with the devices mounted on a heat-sink with a stabilized temperature of 15°C. From the light-current characteristics of broad area lasers of varying cavity length, we determine the value of internal quantum efficiency, η_i, and cavity loss, γ, by plotting the inverse of differential efficiency, η_d, against cavity length. As depicted in Fig. 4.2, the values of η_i and γ are 0.62±0.04 and 6.6±0.5 cm^{-1}, respectively. The shortest cavity length has been excluded from this extraction, since it represent a region where higher-order effects result in an incomplete clamping of the carrier density above threshold, resulting in an apparent decrease in internal quantum efficiency [94]. The value of J_{th} is ~350 A/cm^2 for 1000 μm-long broad area lasers. The device parameters and bias conditions of the measurements on the single-mode lasers are summarized in Table 4.1. The light-current characteristics of a 3 μm-wide and 400 μm-long single mode laser, measured with a pulsed bias at various temperatures, are shown in Fig. 4.3(a). The inset shows the output optical spectrum at 15°C. Plotted in Fig. 4.3(b) are the threshold current and differential efficiency as a function of temperature, as derived from the data of Fig. 4.3(a). It is evident that I_{th} is independent of temperature in the range 5-75°C and so is the differential efficiency. In other words, according to the definition of characteristic temperature (Eqn. 3.1), $T_0=\infty$ in these devices, the first report in any semiconductor laser. This is the crucial temperature range in which extreme stability of these parameters, I_{th}

Laser type	1.3 μm lasers	1.1 μm lasers
Cavity length	400 μm	800 μm
Ridge width	3 μm	8 μm
Mirror reflectivities	95%/32%	32%/32%
Frequency of pulsed bias	10 kHz	10 kHz
Width of pulsed bias	1 μs	1 μs

Table 4.1: Device geometries and bias conditions for the DC and small-signal measurements on the single-mode 1.3 and 1.1 μm p-doped and undoped lasers.

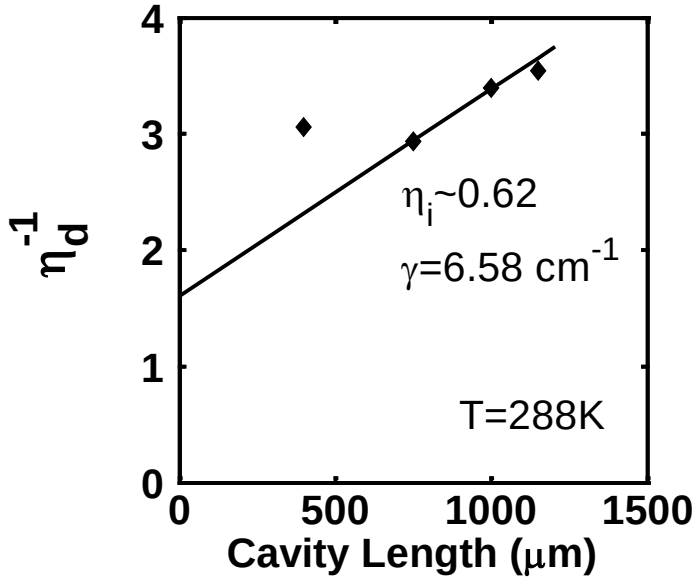

Fig. 4.2: Inverse of differential efficiency, η_d, versus cavity length in broad area p-doped 1.3 μm quantum dot lasers.

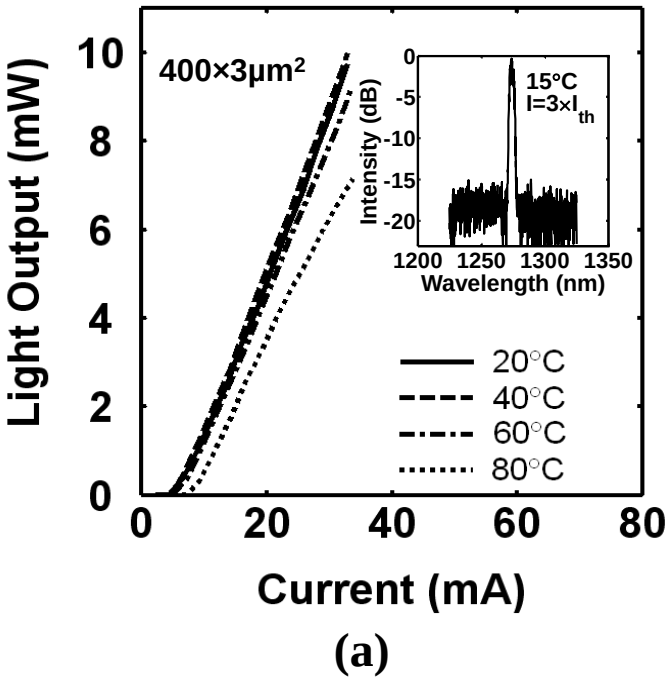

(a)

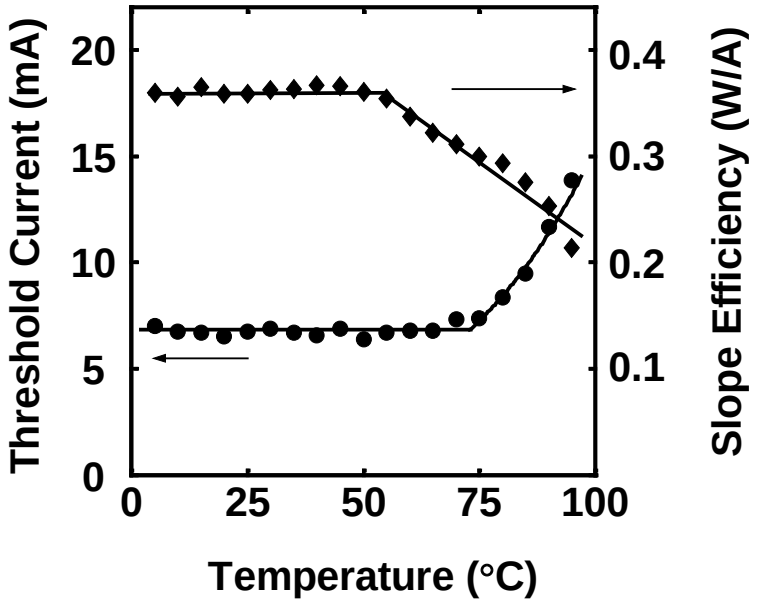

(b)

Fig. 4.3: (a) Light-current characteristics of 400×3 μm^2 single-mode p-doped 1.3 μm quantum dot lasers at different temperatures. The inset shows the output optical spectrum at three times threshold and at 15°C; (b) threshold current and slope efficiency of the same laser versus temperature.

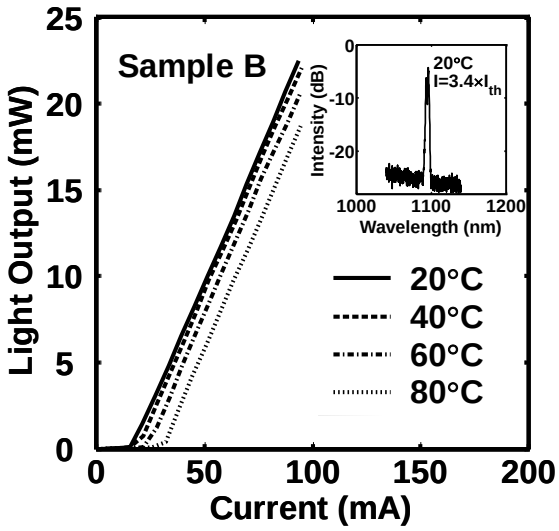

Fig. 4.4: Light-current characteristics of a 800×8 μm^2 p-doped 1.1 μm quantum dot laser at different temperatures with a doping level of 2×10^{18} cm^{-3}. The inset shows the output optical spectrum of the same laser.

and η_d, is desired for the most demanding applications. Similar results were obtained for the broad area lasers and under continuous-wave bias from 5-50°C. In contrast, the conventional undoped QD lasers exhibit T_0=68 K in the same temperature range (5-75°C). This value is very close to the reported value for undoped QD DFB lasers in Chapter III. The respective values of η_i and γ are 0.85±0.03 and 4.3±0.3 cm^{-1} in the undoped laser with a threshold current density of ~110 A/cm^2 for 1000 μm-long broad area lasers. So, it is evident that p-doping increases the threshold current. It may be noted that values of η_i =0.81±0.05 and γ=4.1±0.4 are also determined from the measured differential gain (from modulation data in Section 5.2) in the undoped lasers, which are in good agreement with the above values.

Although a high T_0 has been predicted and previously reported in p-doped QD lasers [45],[46],[81],[82], a value of $T_0=\infty$ is unlikely since the inhomogeneous linewidth broadening of the gain would limit the performance of QD lasers. The observed

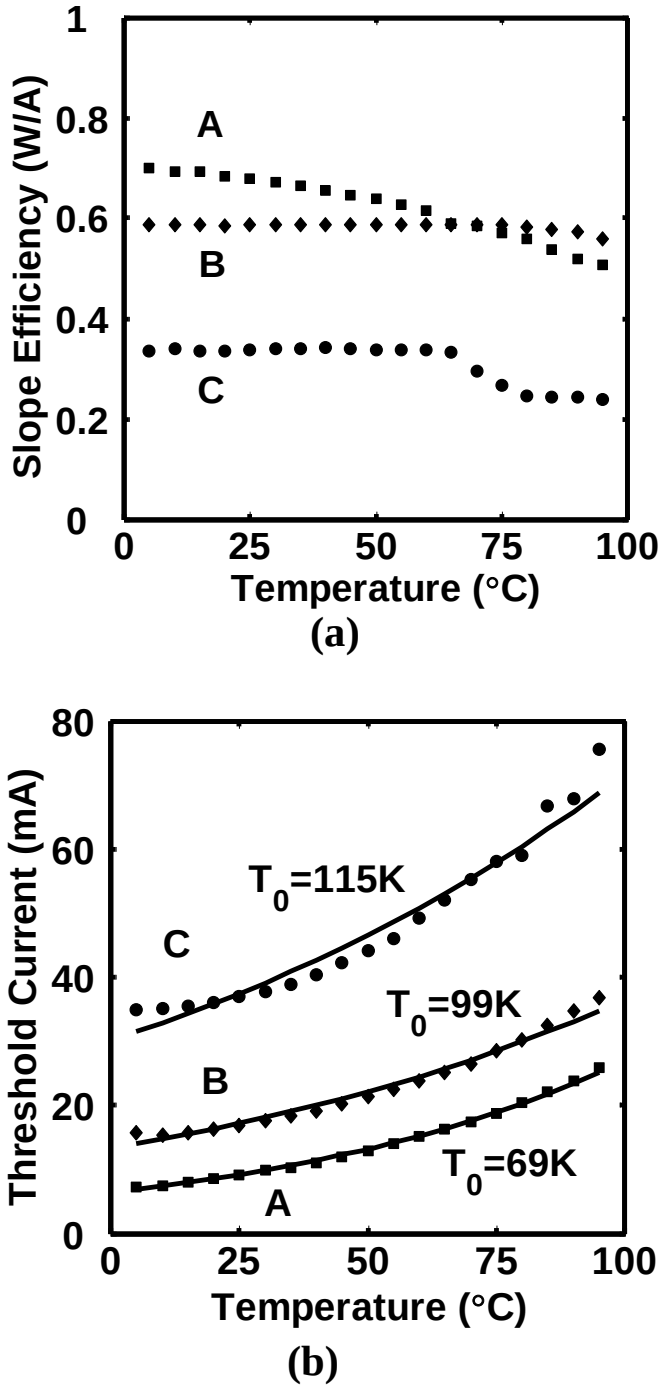

Fig. 4.5: (a) Slope efficiency and (b) threshold current of 800×8 μm^2 p-doped 1.1 μm lasers versus temperature for different beryllium doping levels. A, B, and C denote doping levels of 0, 2×10^{18}, and 8×10^{18} cm^{-3}, respectively. The solid lines are exponential fits to the data, from which the indicated values of characteristic temperature are derived.

behavior is due to the dominance of Auger recombination in the QDs and its temperature dependence, as will be discussed in the next Section.

The measured light-current characteristics and the variation of output slope efficiency and threshold current with temperature of 1.1 μm devices are shown in Figs. 4.4, 4.5(a) and (b) where lasers A, B, and C have increasing p-doping levels of 0, 2×10^{18}, and 8×10^{18} cm^{-3}, respectively. As with the 1.3 μm devices, the threshold current increases with p-doping and so does the value of T_0. However, $T_0=\infty$ is not observed. Auger recombination contributes to the threshold current to a lesser extent in these shorter wavelength lasers than in 1.3 μm devices.

4.4 Threshold Current Model and Analysis

The fundamental theory of the DC characteristics of QD lasers was presented in Section 2.2. In order to analyze the measured temperature variation of the threshold current in undoped and p-doped QD laser, a more involved self-consistent model is developed to calculate the position of the quasi-Fermi levels at threshold. The simple algorithm of the model is presented in Fig. 4.6. Flat-band quasi-Fermi levels across the active region were assumed at threshold [82],[83]. Fermi-Dirac statistics and complete ionization of dopants were also assumed. Charge neutrality amongst the QDs, the wetting layer, the GaAs barrier, and the immobile dopants in the modulation doped barrier was used to find the quasi-Fermi levels at incremental levels of carrier injection into the active region:

$$\rho_{dot}\int_0^{\infty} dE \sum_i \frac{2}{\sqrt{2\pi}\sigma}\exp\left(\frac{-(E-E_e^i)}{2\sigma^2}\right) f_n(E_e^i)$$
$$+ t_d \int_{E_{C,GaAs}}^{\infty} \frac{dE}{2\pi^2}\left(\frac{2m_{e,GaAs}}{\hbar^2}\right)^{3/2} \sqrt{E-E_{C,GaAs}}\, f_n(E_{C,GaAs})$$
$$+ \frac{m_{e,WL}}{\pi\hbar^2}\int_{E_{C,WL}}^{\infty} dE f_n(E_{C,WL}) + N_a^-$$
$$= \rho_{dot}\int_{-\infty}^{0} dE \sum_j \frac{2}{\sqrt{2\pi}\sigma}\exp\left(\frac{-(E-E_h^j)}{2\sigma^2}\right)\left(1-f_p(E_h^j)\right)$$
$$+ t_d \int_{-\infty}^{E_{V,GaAs}} \frac{dE}{2\pi^2}\left(\frac{2m_{h,GaAs}}{\hbar^2}\right)^{3/2} \sqrt{E_{V,GaAs}-E}\left(1-f_p(E_{V,GaAs})\right)$$
$$+ \frac{m_{h,WL}}{\pi\hbar^2}\int_{-\infty}^{E_{V,WL}} dE\left(1-f_p(E_{V,WL})\right) \qquad (4.1)$$

where the first, second and third terms on both sides relate to the QDs, GaAs barrier, and wetting layer, respectively. ρ_{dot} is the dot density, N_a^- is the sheet density of the ionized dopants in the barrier and t_d is the thickness of the GaAs barrier adjacent to each dot layer. f_n and f_p are the Fermi-Dirac distribution function for electrons and holes in the conduction and valence bands, respectively. It is implied in Eqn. 4.1 that the wetting layer is modeled as a two-dimensional electron gas with $m_{e,WL}$ and $m_{h,WL}$ representing the effective masses in the conduction and valence bands, respectively [42]. As will be evident later, carrier occupation of the wetting layer states plays an important role in determining the properties of self-organized QD lasers. The material gain in the QD can be calculated from Eqn. 2.7 for pyramidal-shape dots with a base length of 12 nm and a height of 7 nm for 1.3 μm InAs QDs. Size non-uniformity amongst the dots is accounted for by an inhomogenous Gaussian broadening with linewidth σ_E=50 meV. Three interband transitions, E_{ij}, were included in the modal gain calculation of the dots. The

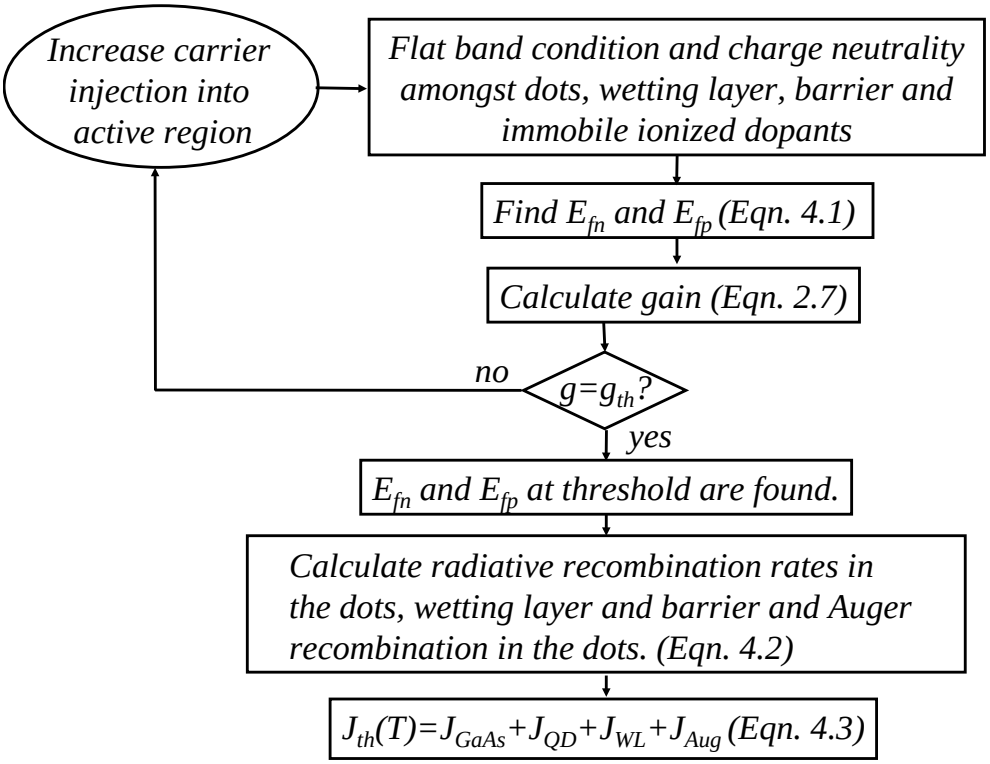

Fig. 4.6: Algorithm of the self-consistent model for calculating gain, and threshold current components in undoped and p-doped QD lasers.

transition energies of the ground state and the first two excited states are 968, 1044, and 1162 meV at room temperature, respectively, according to our photoluminescence measurements. The temperature-dependent bandgaps are calculated with the Varshni equation [95]. A second harmonic oscillator model for 10 degenerate hole states with 10 meV spacing was used [82],[83]. The optical matrix element of different transitions in the QDs and can be calculated with a 8×8 **k.p** model [51],[52].

The threshold gain calculated with Eqn. 4.3 is equated to the sum of the measured cavity loss and the mirror losses (Eqn. 2.9), taking into account an average dot density of 5×10^{10} cm^{-2} and an optical confinement factor $\Gamma=4\times10^{-3}$, which accounts for 10 layers of dots and the areal coverage (fill factor). After determining the position of quasi-Fermi

levels at threshold, the spontaneous radiative recombination terms and corresponding current densities can be calculated. The expressions for R_{sp}^{QD} and J_{QD} were presented in Eqn. 2.10 to 2.12. Similarly, the radiative recombination rate and current in the wetting layer and the GaAs barrier/waveguide region are calculated from:

$$R_{sp}^{k}(\hbar\omega) = \frac{1}{\hbar\omega}\left|M_{ave}\right|^2 \rho_{red}^{k}(\hbar\omega, E^k)\rho_{opt}(\hbar\omega) f_n(1-f_p), \qquad (4.2)$$
$$J_{th}^{k} = qd_{eff}^{k}\int R_{sp}^{k}(\hbar\omega)d(\hbar\omega)$$

where the index k =1 and 2 corresponds to the contribution from the wetting layer and the GaAs barrier/waveguide regions, respectively. ρ_{opt} is the optical mode density (Eqn. 2.11), and ρ_{red}^{k} is the 2-D and 3-D reduced density of states, respectively [47].

Radiative recombination in all three regions described above give rise to threshold current components which increase with temperature. Therefore, a recombination process whose rate decreases with temperature has to be also considered in order to explain the experimentally observed temperature invariant threshold current. The temperature-dependent Auger recombination coefficients in $In_{0.4}Ga_{0.6}As$/GaAs quantum dot lasers have been measured and it was observed that the Auger coefficient *decreases* with increase of temperature [96], which is a direct consequence of the temperature dependence of electron-hole scattering in the dots [51], [96]-[98]. In the present study, the measured variation of the Auger coefficient with temperature is incorporated, but with slightly altered values. An Auger recombination rate in the quantum dots, $R_{Aug}(T) = C_{Aug}(T)(n^2 p + np^2)/2$ was used, where n and p are the total densities of electrons and holes in the dots, respectively. It is important to use this form rather than the common form $C_{Aug}(T)n^3$, since the charge neutrality condition n=p is violated in p-

doped lasers and as formulated in Eqn. 4.1, charge neutrality amongst the dots, wetting layer and barrier states has to be maintained. J_{Aug} is calculated from $d_{dot}R_{Aug}(T)/V_{dot}^3$, where $d_{dot} = N_{stack}\rho_{dot}V_{dot}$ is the nominal thickness of the stacked dot layers.

Other non-radiative recombination terms have been neglected in our model. The possible candidates for threshold current components are recombination in the AlGaAs cladding layers, and thermal excitation from the dots and their subsequent non-radiative recombination in the GaAs waveguide region. AlGaAs recombination is unlikely to be important since the carrier concentration in the cladding layer is very low. Hydrostatic pressure dependence measurement of the threshold current and calculated variation of the dots energy states with pressure have shown that thermal excitation of carriers from the dots may be an important non-radiative term in 1.0 μm QD lasers, but compared to the Auger term, its contribution is insignificant in longer wavelength lasers [99]. Therefore, the total threshold current density is expressed as:

$$J_{th} = \sum_k J_{th}^k + J_{Aug} = J_{QD} + J_{WL} + J_{GaAs} + J_{Aug}. \qquad (4.3)$$

The calculated threshold current components are depicted in Figs. 4.7(a) and (b) for 400×3 μm^2 undoped and p-doped 1.3 μm lasers, respectively. The various parameters used in the calculations are summarized in Table 4.2. The total calculated threshold currents are also shown with the experimental values for comparison. The temperature variation of the Auger coefficients used in these calculations is shown in Fig. 4.8. As explained above, the trend is similar to that measured for 1.0 μm QD lasers, but the values are adjusted to fit the measured threshold currents. It is observed in Fig. 4.7 that for both undoped and p-doped lasers, it is the dominance of radiative recombination in

Parameter	1.3 μm lasers	1.1 μm lasers
Dot inhomogeneous broadening	50 meV	50 meV
Optical confinement factor	4×10^{-3}	5×10^{-3}
Dot density	5×10^{10} cm^{-2}	6×10^{10} cm^{-2}
Dot volume	3.4×10^{5} Å^{3}	2.1×10^{5} Å^{3}
Number of stacks	10	10
Thickness of GaAs waveguide	336 nm	336 nm
Doping level (p-doped lasers)	5×10^{17} cm^{-3}	2×10^{18} cm^{-3}
Cavity loss (doped)	6.6 cm^{-1}	4.8 cm^{-1}
Cavity loss (undoped)	4.3 cm^{-1}	3.0 cm^{-1}

Table 4.2: Parameters used in the modeling of threshold current components in 1.3 and 1.1 μm p-doped and undoped quantum dot lasers.

the wetting layer, J_{WL}, that limits T_0 at high temperatures and carrier recombination in the barrier/waveguide region, J_{GaAs}, is much less influential. This is expected as the conduction and valence band offsets in 1.3 μm QDs are large (ΔE_C=250 meV and ΔE_V=200 meV, respectively); consequently, carrier leakage into the barrier/waveguide region is small. J_{QD} becomes dominant at lower temperatures, which is expected due to the 3-D confinement of carriers. It is evident that it is the decrease of Auger recombination with temperature in the p-doped lasers which compensates the increasing J_{WL} term and explains the measured temperature invariant threshold current in the p-

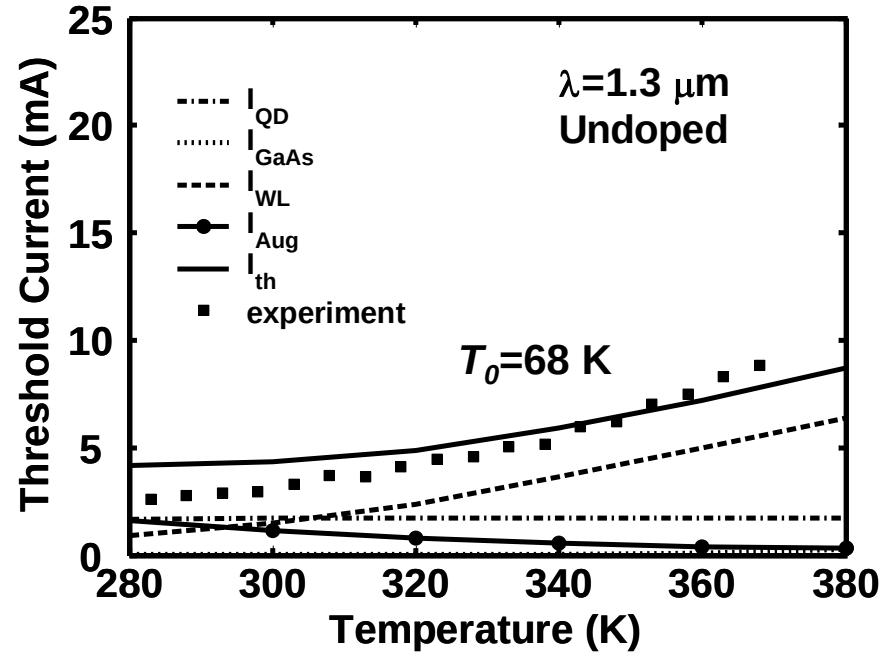

(a)

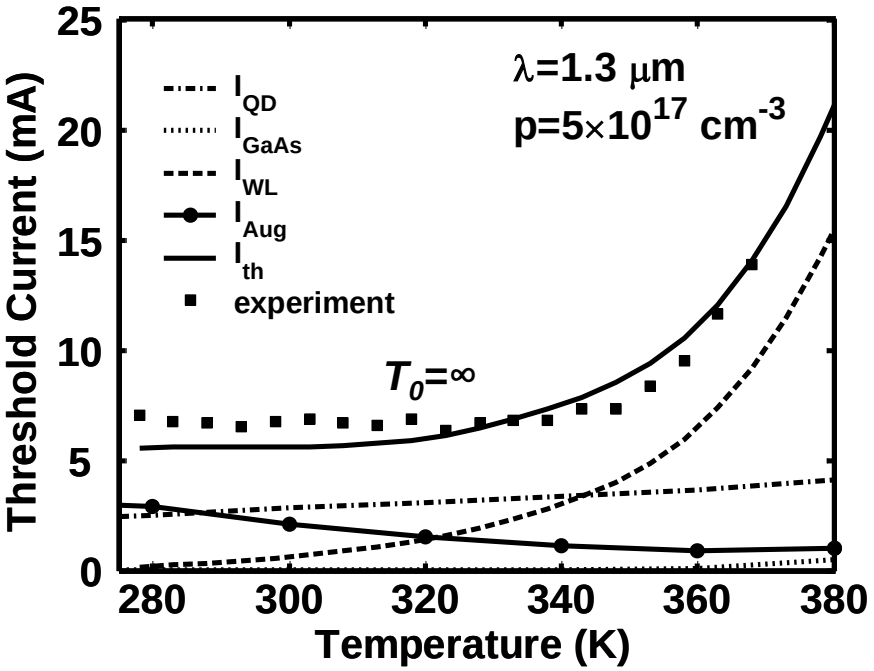

(b)

Fig. 4.7: Measured and calculated threshold current, I_{th}, in 400×3 μm^2 (a) undoped and (b) p-doped 1.3 μm quantum dot lasers. Also shown are the calculated contributing current components: radiative recombinations in the dots (I_{QD}), the barrier/waveguide regions (I_{GaAs}), wetting layer (I_{WL}), and Auger recombination in the dots (I_{Aug}).

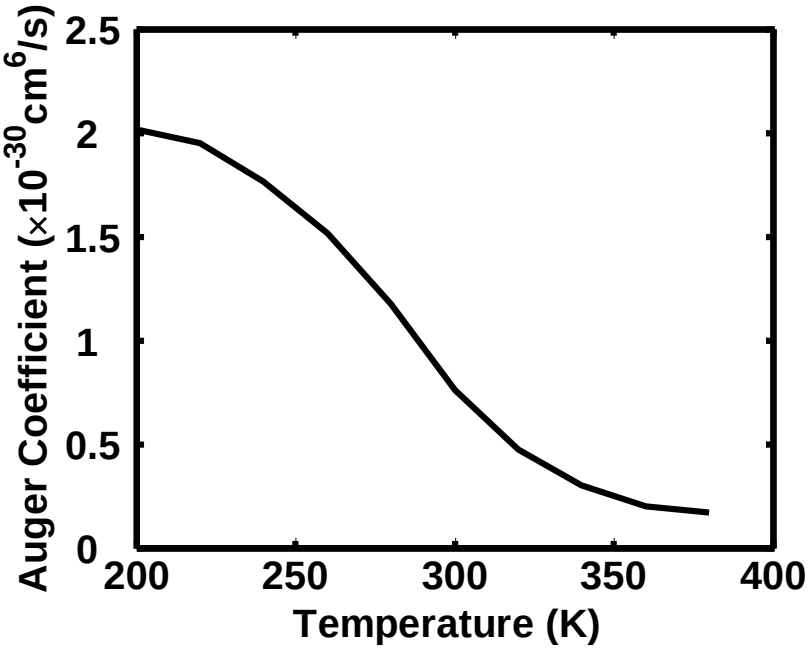

Fig. 4.8: Temperature dependence of the Auger coefficients used in the threshold current calculation of 1.3 μm quantum dot lasers.

doped lasers. However, the temperature invariant operation is achieved at the expense of an *increase* of the total threshold current. Acceptor doping is beneficial for improving the characteristic temperature of the lasers, but it increases the electron-hole scattering rate and, consequently, the Auger recombination rate.

For comparison, it is instructive to analyze the threshold currents measured in p-doped 1.1 μm lasers with the model described above and the parameters of Table 4.2. These are illustrated in Figs. 4.9(a) and (b) for two doping levels, A and B, given in the previous section. It is clear that for both samples the current component due to recombination in the dots is a small fraction of the total threshold current and is almost temperature invariant. The current component due to recombination in the GaAs barrier layer plays the dominant role and more so than in the 1.3 μm lasers due to the relatively

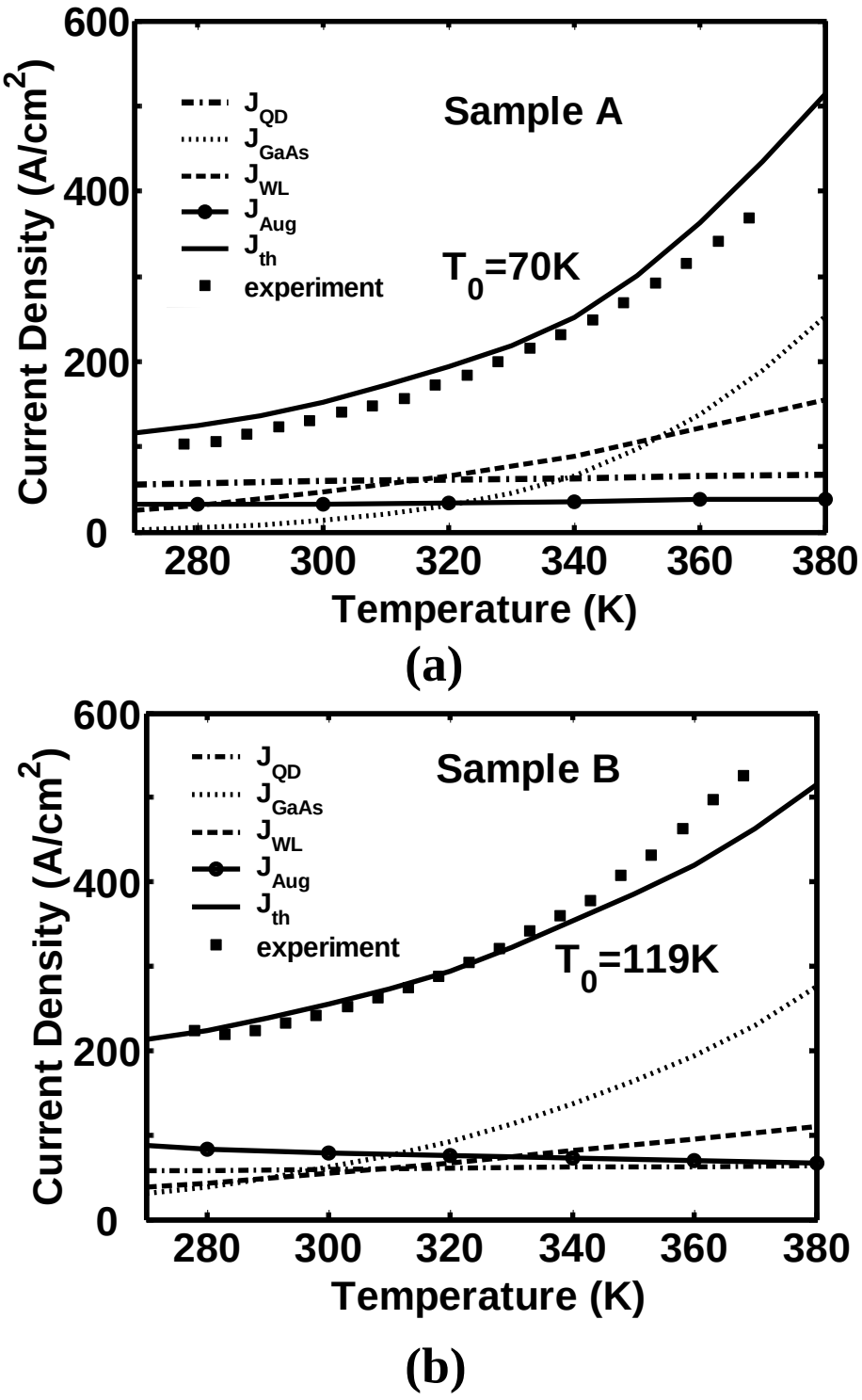

Fig. 4.9: Measured and calculated threshold current density in (a) undoped and (b) p-doped (p=2×10^{18} cm^{-3}) 1.1 μm quantum dot lasers. The values of T_0 are extracted from the calculated threshold current density, J_{th}. The contributing current components are the same as in Fig. 4.7.

shallow carrier confinement in 1.1 μm dots. For the same reason, the temperature dependence of this component is also stronger than in 1.3 μm lasers. The Auger recombination component, and its increase with doping, increases the overall threshold current and also helps to improve T_0. However, T_0 never approaches infinity in these devices.

4.5 Summary

Temperature invariant output slope efficiency and threshold current ($T_0=\infty$) in the temperature range of 5-75°C have been measured for 1.3 μm p-doped self-organized QD lasers with 5×10^{17} cm^{-3} p-doping level in the barriers. Similar undoped QD lasers exhibit T_0=68 K in the same temperature range with lower values of threshold current compared to the doped lasers. P-doping has a similar effect in increasing T_0 and threshold current in 1.1 μm lasers, but the highest observed T_0 is about 115 K for 8×10^{18} cm^{-3} doping level. The temperature dependence of threshold current and the effect of p-doping on gain and differential gain are studied with a self-consistent model that includes temperature-dependent radiative recombination in the dots, wetting layer and GaAs barrier regions and Auger recombination in the QDs. It is found that Auger recombination in the dots plays an important role in establishing temperature invariance of threshold current in the range 5-75°C in 1.3 μm p-doped QD lasers and the increase of T_0 with increase of p-doping level in 1.1 μm QD lasers.

CHAPTER V

P-DOPED QUANTUM DOT LASERS: DYNAMIC PROPERTIES

5.1 Introduction

The small-signal modulation response and other dynamic characteristics of p-doped QD lasers are discussed in this Chapter. These are the same lasers as in Chapter IV. The small energy spacing of hole levels in QDs and the consequent thermal distribution of holes into the many available excited states reduces the attainable gain in undoped QD lasers. Thus, differential gain, *dg/dn*, and modulation bandwidth - which is proportional to the square root of *dg/dn* - is limited in these lasers due to this effect. It has been suggested that p-doping can not only improve the static characteristics of QD lasers (as discussed in the previous Chapter), but can also enhance the modulation bandwidth of the lasers [82]. The extra holes provided at the ground state would increase the occupation probability of holes, f_p, in Eqn. 2.7 and therefore enhance the gain in the lasers. Consequently, it is expected that the differential gain and 3-dB modulation bandwidth should increase upon p-doping as well. Deppe *et al.* [82] theoretically predicted modulation bandwidths as high as 30 GHz in p-doped QD lasers. The present work is the first experimental study of the impact of p-doping on QD lasers. We will see in Section 5.2, that the modulation bandwidth would indeed increase upon p-doping. However, the increase is very slight, i.e., from 5.5 to 8 GHz in 1.3 μm and from ~7-8 to 11 GHz in 1.1

μm QD lasers. In order to analyze this experimental observation, a rate equation-based model has been developed. Gain and differential gain were calculated according to the self-consistent DC model of Section 4.4. It is observed that the improvement in *dg/dn* is modest (less than a factor of 8) upon p-doping due to the population of the wetting layer states whose density of states outnumbers the dot states. Furthermore, our rate equation model predicts even less improvement in the bandwidth due to second order effects such as the increase of Auger recombination in the p-doped lasers compared to the undoped devices.

5.2 Small-Signal Modulation of p-Doped and Undoped Lasers

The small-signal modulation response of single-mode lasers was measured with a high-speed photoreceiver, MITEQ low-noise amplifier and a HP 8593A electrical spectrum analyzer after collecting the output light with a cleaved fiber (see Fig. 3.6). The measured response was corrected by taking into account the amplifier gain and the loss in the microwave cables. The measurements were made under pulsed bias conditions similar to the DC measurements (1μs, 10 kHz). The modulation response of the 400×3 μm^2 single-mode 1.3 μm p-doped lasers at room-temperature and at different injection currents is shown in Fig. 5.1(a). The maximum 3-dB bandwidth, f_{-3dB}, of the p-doped laser measured for an injection bias of 140 mA is ~8 GHz. A differential gain of $dg/dn=6.9\times10^{-15}$ cm^2 can be extracted from its relation with the resonance angular frequency of the modulation response:

$$\omega_r = \sqrt{\frac{c\Gamma S dg/dn}{n_r \tau_p}}, \qquad (5.1)$$

which is calculated with a photon lifetime, τ_p, of 6.6 ps obtained from the measured γ=6.6

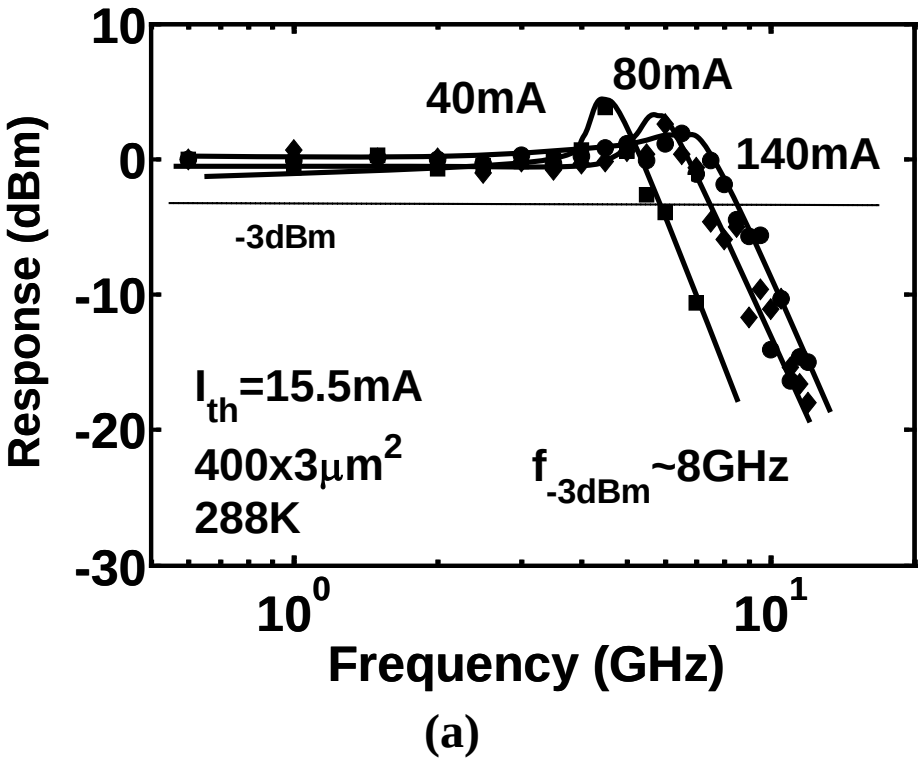

(a)

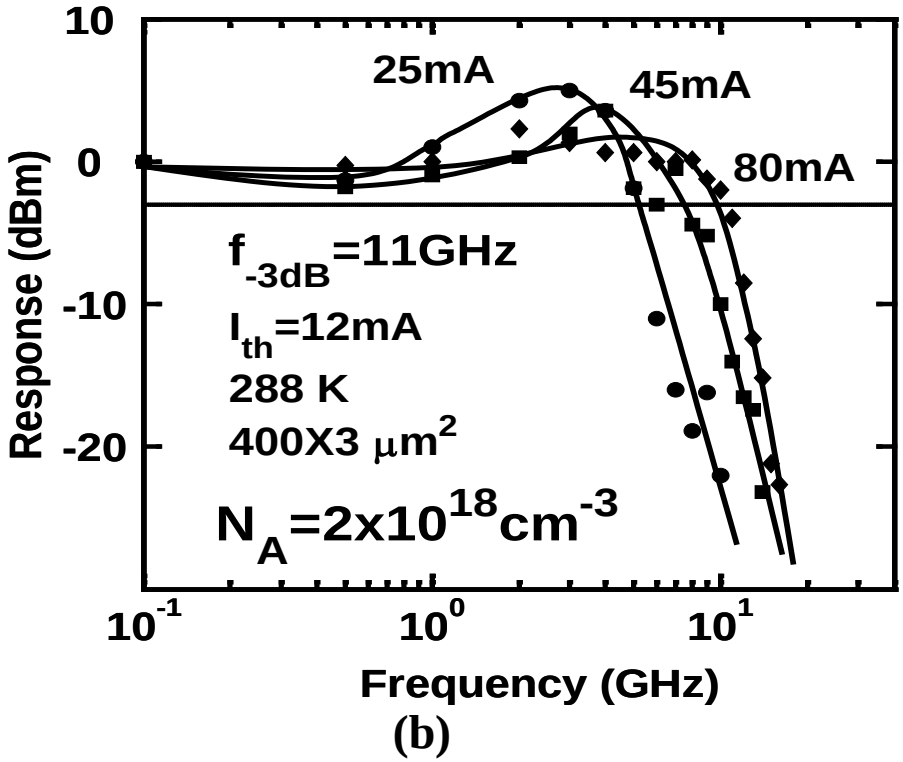

(b)

Fig. 5.1: (a) Measured small-signal modulation response of p-doped (a) 1.3 μm and (b) 1.1 μm quantum dot laser at room temperature for various injection currents.

cm^{-1}, mirror reflectivities of 95%/32% and an optical confinement factor of $\Gamma=4\times10^{-3}$. *S* is the photon density and is extracted from the light-current measurements. It is evident that the 3-dB bandwidth of the p-doped lasers is not substantially larger than that of the undoped lasers, which exhibit a maximum measured modulation bandwidth of ~6 GHz.

The measured modulation response of the 1.1 μm p-doped lasers at different biases is shown in Fig. 5.1(b). For brevity, a 3-dB bandwidth of 11 GHz was measured in these devices. In comparison, the maximum 3-dB bandwidth measured in an undoped 1.1 μm laser is 7-8 GHz.

5.3 Linewidth Enhancement Factor

The linewidth enhancement factor, or α-factor, was measured by the Hakki-Paoli method [100] under sub-threshold bias conditions. Techniques such as injection locking, which measure the α-factor above threshold have yielded values of α in agreement with those derived from the Hakki-Paoli method in quantum well lasers [101]. The results of the two techniques may be different in QD lasers if they exhibit lasing modes from the excited states at high biases [102]. Spectral measurements of our lasers show stable single-mode output spectra from ground state transitions in the QDs at all biases, and therefore it is expected that the subthreshold α-factors would be in agreement with the values above threshold. The net modal subthreshold gain can be expressed as:

$$g = 1/L \ln(R^{-1}(\sqrt{r_i}-1)(\sqrt{r_i}+1)^{-1}), \qquad (5.2)$$

where L is the cavity length, R is the facet reflectivity, and r_i is the peak to averaged-valleys ratio of competing modes in the output optical spectrum. From the resonant cavity condition, the refractive index, $n = i\lambda_i / 2L$, and the linewidth enhancement factor,

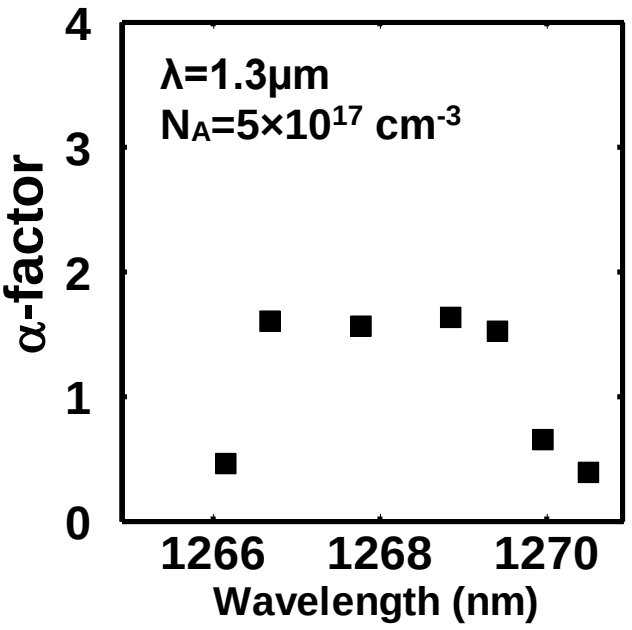

Fig. 5.2: Measured linewidth enhancement factor of the p-doped 1.3 μm quantum dot laser at subthreshold peak wavelengths of the output spectrum.

$\alpha = -4\pi / \lambda(\Delta n / \Delta N)(\Delta g / \Delta N)^{-1}$, can be experimentally determined from:

$$\alpha = \frac{2}{\partial\lambda} \frac{\Delta\lambda_i}{\Delta\{\ln[(\sqrt{r_i} - 1)(\sqrt{r_i} + 1)^{-1}]\}}, \qquad (5.3)$$

where $\partial\lambda$ is the mode spacing and ΔN is the incremental carrier density for two differential bias values. The subthreshold spectra were measured with a HP 70952B optical spectrum analyzer under 10 kHz pulsed bias with a duty cycle of 1% at room temperature. The voltage increment, ΔV, was kept below 0.1 V, which corresponds to less than ~1mA increase in the laser current, to ensure a differential increase of the laser bias. The measured linewidth enhancement factors are plotted against the peak wavelength of the subthreshold spectrum in Fig. 5.2. It is observed that $\alpha \sim 1.6$ at the lasing wavelength of ~1268 nm. Although this value is relatively low compared to those in quantum well lasers with typical values of $\alpha > 2$, it is higher than our reported values of

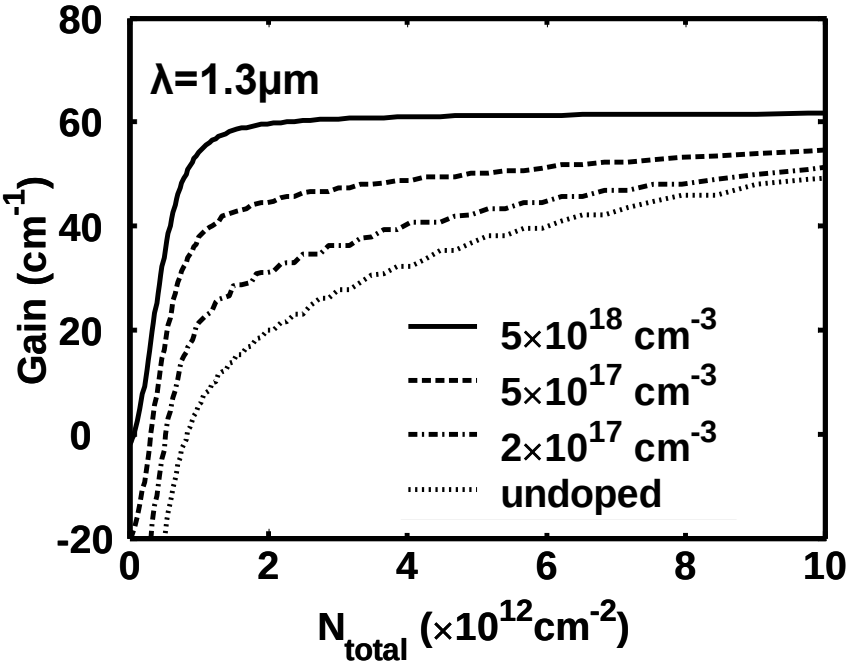

Fig. 5.3: Calculated peak modal gain versus total injected carrier density for various modulation doping concentrations in 1.3 μm p-doped quantum dot laser.

~0.7 in tunnel injection quantum dot lasers [76], as will be discussed in the next Chapter.

5.4 Gain and Differential Gain Analysis

In order to model the modulation response of p-doped QD lasers, it is necessary to calculate gain and differential gain in these devices. This can be readily achieved by the self-consistent model explained in Section 4.4. Figure 5.3 shows the calculated peak modal gain of 1.3 μm lasers versus total sheet density of electrons injected into the dots, the wetting layer and the adjacent barrier layer for varying p-type doping levels. It is evident that with increasing doping higher gain can be achieved, accompanied by a smaller electron transparency density. This is due to the occupation of higher energy hole states in the QDs with increased doping, leading to f_p approaching zero in Eqn. 2.7. The values of differential gain at threshold are approximately 1.1×10^{-9} and 8×10^{-9} cm for

doping levels of 0 and 5×10^{17} cm^{-3}, respectively. A larger increase in differential gain is not achieved because a fraction of the holes provided by the doped barriers will reside in the two-dimensional wetting layer valence band states, which have a higher density of states than that in the dots [42]. In fact, an increase of differential gain was calculated for p-doped quantum dash lasers when the effect of the wetting layer was excluded compared to when the effect was included in the simulation [84].

5.5 Modulation Response Model and Analysis

It has been suggested that use of carrier and photon rate equations are not valid for QD lasers because of the random distribution of injected carriers amongst the dots [103]. However, reported agreement between Monte Carlo simulations and rate equations with *averaged* population densities suggest that standard rate equations could be used for QD lasers [104], particularly at high temperatures. The rate equations for the 2-D population of carriers in the dot ground state, N_1, the dot excited state, N_2, and the 3-D population in the GaAs barrier/waveguide region, N_C, are expressed as:

$$\frac{\partial N_1}{\partial t} = \frac{N_C}{\tau_{c1}}(1-\frac{N_1}{2N_d}) + \frac{N_2}{\tau_{21}}(1-\frac{N_1}{2N_d}) - \frac{N_1}{\tau_{12}}(1-\frac{N_2}{2N_d}) - \frac{N_1}{\tau_{e1}} - \frac{J_{Aug}}{q} - R_{sp1}^{QD}(N_1)$$
$$-\frac{c}{n_r}\Gamma g(N_1)S$$
$$\frac{\partial N_2}{\partial t} = \frac{N_C L_{SCH}}{\tau_{c2}}(1-\frac{N_2}{2N_d}) + \frac{N_1}{\tau_{12}}(1-\frac{N_2}{2N_d}) - \frac{N_2}{\tau_{21}}(1-\frac{N_1}{2N_d}) - \frac{N_2}{\tau_{e2}} - R_{sp2}^{QD}(N_2)$$
$$\frac{\partial N_C}{\partial t} = \frac{J}{qL_{SCH}} + \frac{N_2}{\tau_{e2}L_{SCH}} + \frac{N_1}{\tau_{e1}L_{SCH}} - \frac{N_C}{\tau_{c2}}(1-\frac{N_2}{2N_d}) - \frac{N_C}{\tau_{c1}}(1-\frac{N_1}{2N_d}) - \frac{R_{sp}^{SCH}(N_C)}{L_{SCH}}$$
$$\frac{\partial S}{\partial t} = \frac{c}{n_r}(\Gamma g(N_1) - \gamma)S + \beta R_{sp1}^{QD}(N_1), \qquad (5.4)$$

where S is the photon density, β=10^{-5} is the spontaneous emission factor, N_d is the QD density times the number of dot stacks, L_{SCH} is the thickness of the separate confinement

heterostructure (SCH) region, and J is the injected current density into the SCH region. τ_{c1}, τ_{c2}, τ_{e1}, and τ_{e2} are the capture and escape lifetimes between the barrier/waveguide region and the ground and excited dot states, respectively. τ_{21} and τ_{12} denote the capture and escape lifetimes between the two dot states. The values used for all these lifetimes in our analysis can be found elsewhere [74]. It is noteworthy that a more detailed analysis of the problem includes the rate equations for the nonequilibrium population of the wetting layer and the entropy change of carriers relaxing from this state into the dot states [70]. However, it has been shown that at room temperature the quasi-equilibrium effects associated with the close spacing of the hole states can be taken into account with simpler models that neglect the influence of the entropy change in the rate equations [82].

By substituting $N_{1,2,C} = N_{1,2,C}^0 + n_{1,2,C}e^{i\omega t}$, $J = J^0 + je^{i\omega t}$ and $S = S^0 + se^{i\omega t}$, the steady-state and small signal solutions can be separated. We also assume that J_{Aug}, g, and the three R_{sp} terms in the rate equations can be linearized around their corresponding DC values. If we further make the reasonable assumptions that n_1, $N_2 << N_d$, the small signal equations are linearized and the modulation response transfer function can be expressed as:

$$F(i\omega) = \frac{s(i\omega)}{j(i\omega)} = \frac{-a_{41}(a_{12}a_{23} - a_{13}(a_{22} + i\omega))}{qL_{SCH} \times D}$$
$$D = [(a_{11} + i\omega)i\omega - a_{41}a_{14}][(a_{22} + i\omega)(a_{33} + i\omega) - a_{32}a_{23}] +$$
$$[a_{12}(a_{31}a_{23} - a_{21}(a_{33} + i\omega) + a_{13}(a_{32}a_{21} - a_{31}(a_{22} + i\omega)]i\omega, \qquad (5.5)$$

where

$$a_{11} = \frac{1}{\tau_{12}} + \frac{1}{\tau_{e1}} + \frac{\partial J_{Aug}}{q\partial N_1} + \frac{c\Gamma S^0}{n_r}\frac{\partial g}{\partial N_1} + \frac{\partial R_{sp1}^{QD}}{\partial N_1}, a_{22} = \frac{1}{\tau_{e2}} + \frac{1}{\tau_{e1}}(1 - \frac{N_1^0}{2N_d}) + \frac{\partial R_{sp2}^{QD}}{\partial N_2},$$

$$a_{33} = \frac{1}{\tau_{c2}} + \frac{1}{\tau_{c1}}(1 - \frac{N_1^0}{2N_d}) + \frac{1}{L_{SCH}} \frac{\partial R_{sp}^{SCH}}{\partial N_C}, a_{12} = (\frac{N_1^0}{2N_d} - 1) \frac{1}{\tau_{21}},$$
$$a_{13} = (\frac{N_1^0}{2N_d} - 1) \frac{L_{SCH}}{\tau_{c1}}, a_{14} = -\frac{1}{\tau_{12}}, a_{23} = -\frac{L_{SCH}}{\tau_{c2}}, a_{31} = -\frac{1}{\tau_{e1} L_{SCH}},$$
$$a_{32} = -\frac{1}{\tau_{e2} L_{SCH}}, a_{41} = -\frac{c\Gamma}{n_r} \frac{\partial g}{\partial N_1} S^0 - \beta \frac{\partial R_{sp1}^{QD}}{\partial N_1}. \qquad (5.6)$$

Two other valid approximations further simplify *F(iω)*. First, inspection of typical values for a_{ij} reveals that $i\omega << a_{22}$, therefore the zero of the polynomial in the numerator of Eqn. 5.5 can be ignored. Second, in the "steady state approximation" we set $i\omega n_c \approx 0$ [105]. This is valid since the 3D carriers in the waveguide do not interact directly with photons and eliminating their AC term is a second order effect. Consequently,

$$F(i\omega) = \frac{s(i\omega)}{j(i\omega)} = \frac{-a_{41}(a_{12}a_{23} - a_{13}a_{22})}{qL_{SCH}(iA_3\omega^3 + A_2\omega^2 + A_1\omega + A_0)},$$
$$A_0 = a_{14}a_{41}a_{23}a_{32} - a_{41}a_{14}a_{22}a_{33},$$
$$A_1 = a_{11}a_{22}a_{33} - a_{23}a_{14}a_{32}a_{11} - a_{41}a_{14}a_{33} + a_{12}a_{31}a_{23},$$
$$A_2 = -a_{11}a_{33} - a_{22}a_{33} + a_{13}a_{31} + a_{23}a_{32}, A_3 = -a_{33}. \qquad (5.7)$$

The form of Eqn. 5.7 is mathematically similar to that expressed by Nagarajan *et al.* [106] for quantum well lasers. The denominator in Eqn. 5.7 is a third-order polynomial , and the poles of the modulation response can be determined analytically. Comparison with the results obtained from Eqn. 5.5 confirmed that the approximate form in Eqn. 5.7 is accurate and therefore the latter is used in our analysis.

In calculating the modulation response of 1.3 μm p-doped QD lasers, the photon density, *S*, was estimated from the DC solution of the rate equations (Eqn. 5.4) and the values of N_1, N_2, N_C, *g*, and the partial derivative of radiative and Auger recombination rates were calculated from the self-consistent model for threshold current discussed and described in

the previous Chapter. The modulation responses of the undoped and p-doped lasers, for different levels of injection, are shown in Figs. 5.4(a) and (b), respectively. The maximum 3-dB bandwidths of the undoped and p-doped lasers are 6.5 and 11 GHz, respectively, which are in reasonable agreement with the measured values presented in Section 5.2. The resonance angular frequency, ω_r, is proportional to the square root of the differential gain (see Eqn. 5.1). Therefore, considering the calculated increase of differential gain from 1.1×10^{-9} to 8×10^{-9} cm after increasing p-doping from 0 (undoped) to 5×10^{17} cm^{-3}, an increase of the modulation bandwidth by a factor of 2.7 might be expected. The calculated and experimentally observed increase is less than this value. This is because the modulation bandwidth can be reduced by other related effects, which are accounted for in our model. For example, the increase of Auger recombination in p-doped lasers can play a limiting role in the modulation response of the devices. It can not only decrease the modulation efficiency by increasing the threshold current, but can also contribute to a larger effective damping factor through the $\partial J_{Aug}/\partial N_1$ term, as included in the rate equations. The transfer function of Eqn. 5.7, including this effect, predicts a modest increase of modulation bandwidth, by a factor of ~1.7, which is closer to our observation. Similar reduction of modulation bandwidth due to second order effects, such as carrier transport across the SCH region, has been reported in quantum well lasers [106].

The small-signal modulation response of the 1.1 μm p-doped QD lasers was also calculated using the model described above. The maximum 3-dB bandwidths for an undoped laser and for a QD laser doped with $p=2\times10^{18}$ cm^{-3} are 8.5 and 12.5 GHz, respectively. Again, the agreement with measured data is reasonable and the increase in

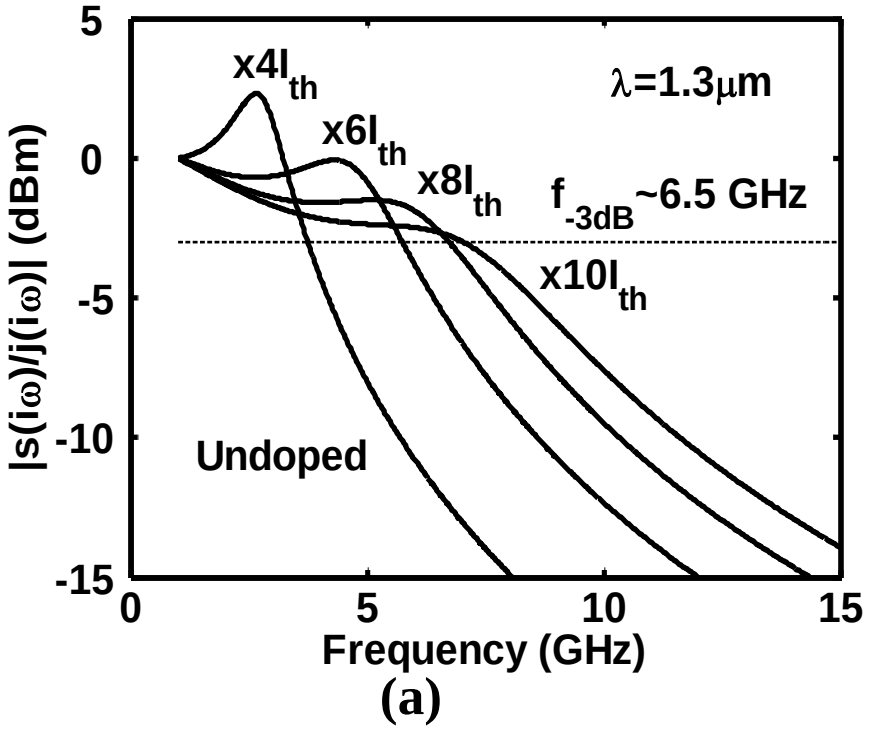

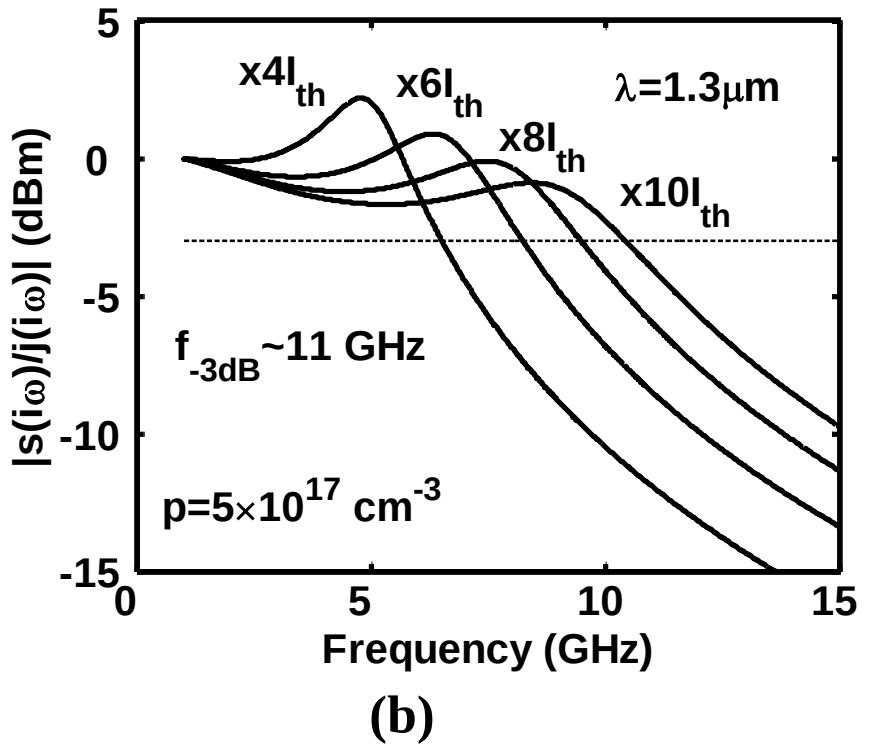

Fig. 5.4: Calculated room temperature small-signal modulation response at various current biases, obtained from Eqn. 5.7, for (a) undoped and (b) p-doped 1.3 μm quantum dot lasers.

bandwidth is by a factor of ~1.5. It is possible that slightly better performance may be extracted with higher levels of p-doping, but the related diffusion effects may actually degrade device performance.

5.6 Summary

The small-signal modulation response and linewidth enhancement factor of the p-doped lasers described in Chapter IV is presented. P-doped quantum dot lasers show slight improvement of 3dB modulation bandwidth compared to undoped lasers. The figure of merit improves from 5.5 to 8 GHz in 1.3 μm and from 8 to 11 GHz in 1.1 μm quantum dot lasers. The derived differential gain in 1.3 μm quantum dot lasers is about 6.9×10^{-15} cm^{-2} and α-factor is ~1.6 at lasing wavelength. An increase of differential gain from 1.1×10^{-9} to 8×10^{-9} cm^{-1} was calculated in these devices for doping levels of 0 and 5×10^{17} cm^{-3}, respectively, which translates to a factor of ~1.7 improvement in the 3dB modulation bandwidth from a rate equation model. The slight improvements in differential gain and modulation bandwidths are attributed to the limiting role of wetting layer states and Auger recombination in the dots.

CHAPTER VI

UNDOPED AND P-DOPED TUNNEL INJECTION QUANTUM DOT LASERS

6.1 Introduction

Demonstration of high-speed QD lasers can be envisioned as a breakthrough for their application as coherent light sources in 1.0-1.3 μm short-haul local area network and metropolitan area network 10 Gb/s communication systems. However, achieving high modulation bandwidths with conventional separate confinement heterostructure (SCH) QD lasers has not been possible [24]. As discussed in Section 2.3, there are unique problems that limit the modulation performance of conventional SCH QD lasers as compared to what is expected from an ideal QD laser with singular density of states. First, the inhomogenous linewidth broadening, associated with the stochastic size distribution of the dots, imposes a limit on the performance of QD lasers. More importantly, SCH QD lasers suffer from significant hot-carrier effects and associated gain compression due to the large density of states of the wetting layer and barrier states as compared with that in the QDs [42]. As a result, the conventional devices cannot be modulated at bandwidths above 6-8 GHz [24].

In Section 2.3, I described the intrinsic problems of QD lasers that determine the small-signal modulation bandwidth and the temperature dependence of the threshold current. This was followed by a description of tunnel injection and p-doping in QD lasers

as unique solutions to the problems in Section 2.4. It was concluded in Chapter IV and V that although p-doping is helpful for improving the characteristic temperature, T_0, of QD lasers - especially at 1.3 μm - it does not help in realizing high modulation bandwidth lasers. On the other hand, we will see in this Chapter that tunnel injection not only decreases the temperature sensitivity of QD lasers, but also significantly enhances the high frequency response of the devices. Static and small-signal properties of undoped 1.1 μm TI-QD lasers is reviewed in Section 6.3.1, which will be followed by near field pattern (filamentation), chirp and linewidth enhancement factor, and accelerated lifetime measurements. The filamentation effects and dynamic properties of the undoped TI-QD lasers will be compared to fabricated quantum well laser counterparts with otherwise identical structures. Then, the properties of 1.1 μm QD lasers, in which tunnel injection and p-doping are incorporated, are described in Section 6.4. The DC characteristics and high-speed modulation characteristics of these devices are described and discussed. Finally, data on chirp, α-factor and direct measurement of modal gain in these devices are presented. It will be evident that present high-speed QD lasers are promising candidates for applications in MAN and LAN systems.

6.2 Laser Design, Epitaxial Growth and Fabrication

The laser heterostructures were grown by molecular beam epitaxy (MBE) on (001) GaAs substrates. The heterostructure of a 1.1 μm InGaAs TI QD lasers is schematically shown in Fig. 6.1(a). The band diagram in the active region is shown in Fig. 6.1(b). The wavelength of the dot luminescence peak is controlled by adjusting the InGaAs dot charge during epitaxy. The active region consists of a 95 Å $In_{0.25}Ga_{0.75}As$ injector well, a

20 Å $Al_{0.55}Ga_{0.45}As$ tunnel barrier, and three coupled $In_{0.50}Ga_{0.50}As$ quantum dot layers. The $In_{0.25}Ga_{0.75}As$ injector layer is grown at 450°C and the QD layers are grown at 510°C. The energy separation in the conduction band between the injector layer state and the QD ground state is ~36 meV at room temperature. This energy separation ensures longitudinal optical (LO) phonon-assisted tunneling from the injector layer to the dot ground states through the AlGaAs barrier. It has to be noted that tunneling acts as a filtering process and selects the QDs whose ground state energy in the conduction band is resonantly coupled with the injector layer state, which results in a reduction of the inhomogenous linewidth broadening observed in photoluminescence spectra by a factor of two in TI QD heterostructures [75]. In the p-doped lasers, doping is provided by delta-doping (5×10^{11} cm^{-2}) of the 500 Å barrier/waveguide region grown on top of the three layers of coupled QDs. 50 nm of the GaAs waveguide above the three coupled QD layers are p-type doped with beryllium ($N_a=5\times10^{17}$ cm^{-3}), averaging about 20 holes per dot.

Mesa-shaped single-mode ridge waveguide lasers (3-5 μm ridge width) were fabricated by standard lithography, wet and dry etching, and metallization techniques, the details of which can be found in the Appendix of this thesis. 200-2000 μm long lasers were obtained by cleaving. Measurements were made on lasers with as-cleaved facets under pulsed bias conditions (1μs, 10 kHz).

6.3 Characteristics of 1.1 μm Undoped Tunnel Injection Lasers

6.3.1 Review of DC and Small-Signal Modulation Properties

The static and small signal characteristics are described elsewhere and are briefly reviewed here for completeness [44],[74]. The undoped 1.1 μm TI QD lasers exhibit

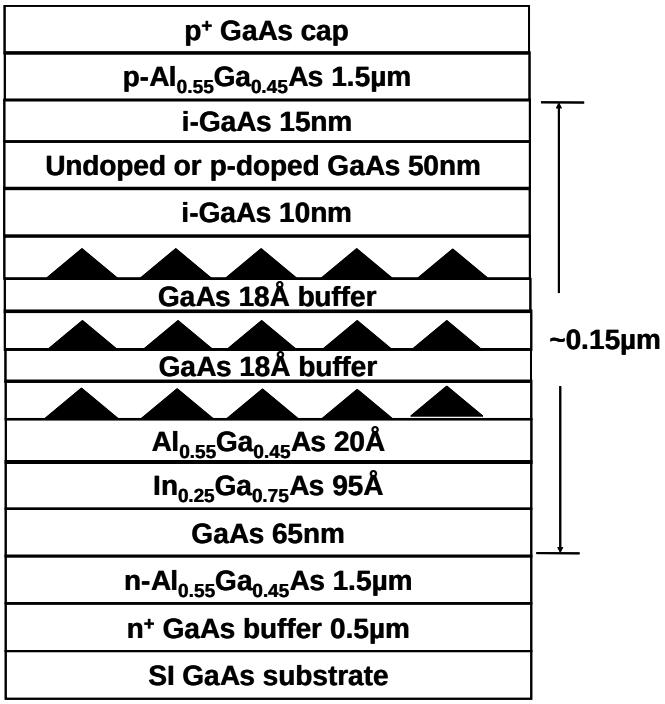

(a)

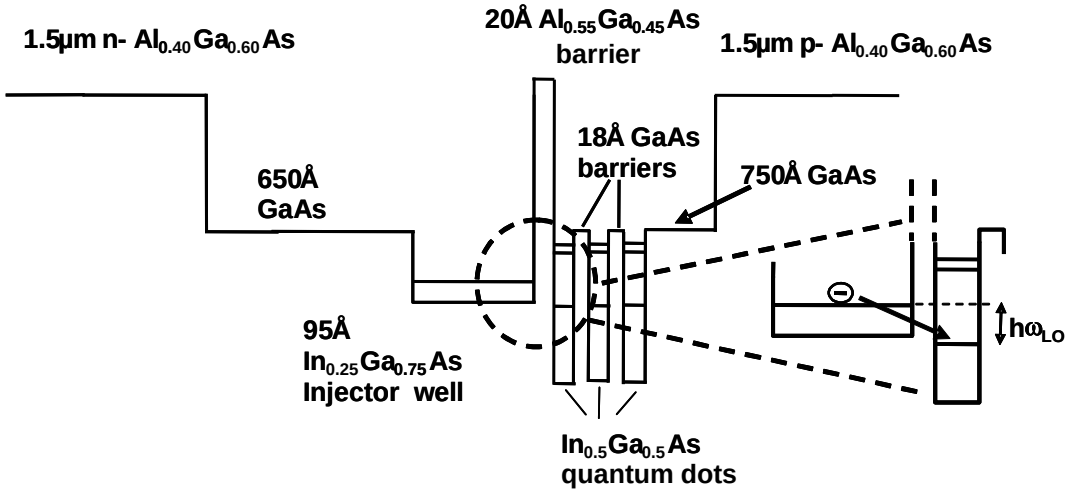

(b)

Fig. 6.1: (a) Heterostructure schematic of 1.1 µm undoped and p-doped tunnel injection quantum dot lasers; (b) conduction band diagram of 1.1 µm p-doped quantum dot tunnel injection laser.

T_0~237 K for 5°C<T<60°C and a threshold current of 8 mA at 288 K for a 400×3 μm^2 device. From the L-I characteristics of TI-QD lasers of varying cavity length, internal quantum efficiency η_i=85% and cavity loss γ=8.2 cm^{-1} were determined by plotting the inverse of differential efficiency, η_d, against cavity length, l. It is evident that the DC characteristic temperature of TI lasers is much higher than typical values in conventional QD lasers (T_0<100 K), which is due to efficient (direct) injection of cold carriers into the ground state of QDs, minimal occupation of wetting layer/barrier states, and the consequent reduction in the radiative recombination component of threshold current from these higher energy states. The undoped TI QD lasers have a maximum modulation bandwidth, f_{-3dB}, of ~22 GHz at a bias of 125 mA. By plotting the resonance frequency versus $(I - I_{th})^{1/2}$, a modulation efficiency of ~1.7 GHz/mA$^{1/2}$ is derived in these lasers. A differential gain, dg/dn=2.7×10^{-14} cm^{-2} in these devices is derived from the measured modulation efficiency and a calculated optical confinement factor of Γ=2.5×10^{-3}. From the damping factor of the best fit to the modulation response, a gain compression factor ε=8.2×10^{-16} cm^3 is also obtained for these devices.

6.3.2 Near-Field Pattern and Filamentation

Spatial coherence and lateral mode control of the output beam of semiconductor lasers at high power operation are important specifications for practical applications [30]. At high levels of carrier injection, filamentation occurs due to the increase of refractive index and self-focusing of the optical mode in the gain medium [107]. As a result, the laser output does not exhibit a Gaussian single-mode near-field pattern, and increase of the stripe width to enhance output power does not follow simple scaling rules [108]. The

degree of filamentation is strongly dependent on the linewidth enhancement factor, which itself is inversely proportional to the differential gain. Large differential gains have been demonstrated in QD lasers [24],[27]. It is therefore expected that filamentation will be greatly reduced in these devices and such reduction has been experimentally demonstrated in broad area InGaAs QD lasers [109]. Ribbat *et al.* [110] have also measured the near-field pattern and beam quality factor of narrow stripe InGaAs QD lasers. All these studies have been conducted with conventional separate confinement heterostructure (SCH) lasers. In this Subsection, a significant suppression of filamentation in undoped $In_{0.4}Ga_{0.6}As/GaAs$ TI-QD lasers is reported, which is associated with lowering of the α-factor in these devices, as will be discussed in the next Subsection.

The results are compared with a conventional SCH quantum well (QW) laser. The SCH QW laser heterostructures were also grown by MBE and consists of two 75 Å $In_{0.2}Ga_{0.8}As$ QWs in the center of a 250 nm GaAs waveguide region, surrounded by 1.45 μm cladding layers. The remainder of the heterostructure is identical to that of the QD lasers. Single-mode ridge waveguide lasers, with 3 μm ridge width, were fabricated by techniques similar to the TI-QD lasers. 400-800 μm long lasers were obtained by cleaving, and the cleaved facets were left uncoated.

The near-field pattern of the TI-QD and QW lasers were measured with a Spiricon system. The output beam at the laser facet was focused with a 60X objective and attenuated with neutral density filters of total 0.3% transmission in order to avoid signal saturation in the camera. The pixel width of the image was calibrated by illuminating the laser ridge with a 5145 Å He-Ne laser at the same focal position. The near field was measured as a function of injection current in 400 μm TI-QD and 800 μm QW lasers.

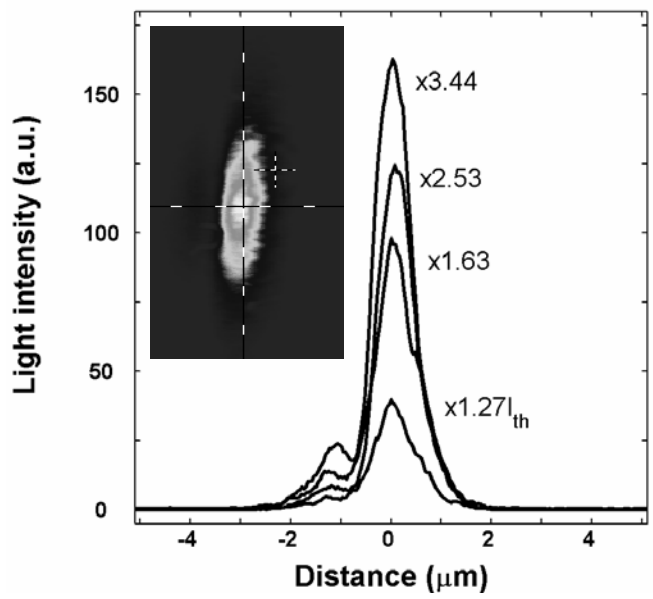

(a)

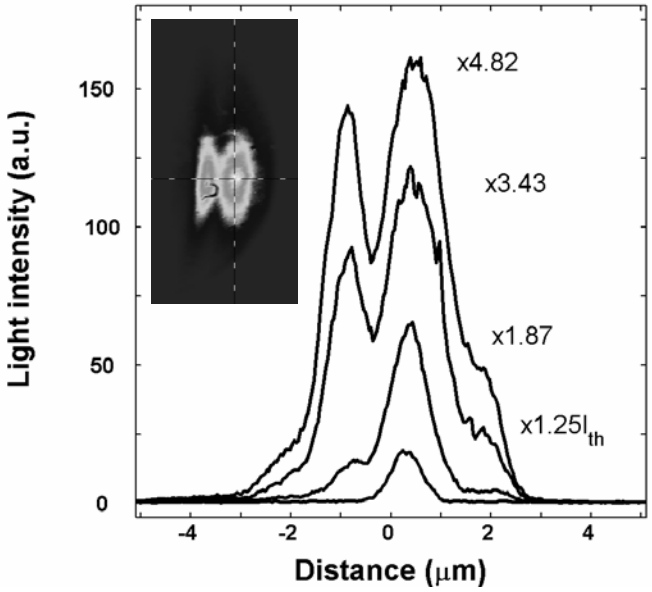

(b)

Fig. 6.2: Spatial intensity distribution of near-field mode pattern along junction plane at cleaved edge for different biases for (a) undoped tunnel injection quantum dot laser and (b) SCH quantum well laser. The distances are measured from the center of ridges. Insets show the near field images of the modes at the highest biases.

Examples of the spatial intensity through the center of the junction plane for different bias levels are shown in Figs. 6.2(a) and (b) for the TI-QD and QW lasers, respectively. The insets are the two-dimensional beam pattern at the corresponding highest shown biases. The QW laser remains single-mode upto an injection current of $1.87\times I_{th}$ but clearly suffers from filamentation for higher injection level and two distinct lobes are observed at higher biases. Such filamentation was previously reported in narrow ridge waveguide QW lasers [110]. In contrast, filamentation is not evident in the intensity distribution of the TI-QD laser and the near-field pattern maintains a Gaussian form upto a bias of $\sim 3.5\times I_{th}$. It is noteworthy that the QD laser exhibits a narrower near-field beam width than the QW laser. While lateral diffusion of carriers widens the beam to about 4 μm at high biases in the QW laser, the beam of the TI-QD device is confined within the 3-micron ridge. Current spreading in the active region is more pronounced in narrow-stripe lasers. However, since lateral carrier transport in QDs is dominated by the slow hopping process at high temperatures, QD lasers provide better confinement [111]. This evidence of lateral confinement in the near-field pattern is also consistent with reported lateral diffusion lengths obtained from cathodoluminescence measurements [112].

6.3.3 Linewidth Enhancement Factor and Chirp

The linewidth enhancement factors of the QW and TI-QD lasers of the previous Subsection were measured from the net modal sub-threshold spectrum [100]. The sub-threshold spectra were measured with an optical spectrum analyzer under pulsed bias. The details of the measurement were previously described in Section 5.3. The measured linewidth enhancement factors are plotted against the peak wavelength of the

subthreshold spectrum for the TI-QD and QW lasers in Figs. 6.3(a) and (b), respectively. The QW laser exhibits a value of $\alpha \cong 3.7$ at lasing wavelength, which is similar to previous reports [113]. In the undoped TI-QD laser, $\alpha \cong 0.73$ at the lasing wavelength and is as small as 0.1 at other wavelengths. These are amongst the smallest values of α-factor measured in any semiconductor laser [28], but even lower values are reported for p-doped TI QD lasers in Section 6.4.3. The low α-factor measured in the TI lasers is a reflection of the fact that the large differential gain and symmetric gain spectrum in quantum dots, together with minimization of carrier leakage, play important roles. The reduction of α by a factor of 5 in the QD lasers, compared to that of QW lasers, implies very small refractive index change in the lasing core. Consequently, there is a reduction of the self-focusing effect in these devices, which accounts for the absence of filamentation in the measured near-field pattern.

Since chirp is directly proportional to α, TI QD lasers are expected to have low chirp. We measured the chirp in these devices and compared it with QW lasers. The envelope of the dynamic shift in wavelength of the sinusoidal modulation signal was recorded with the HP 70952B optical spectrum analyzer and a resolution of 0.8 Å. As schematically shown in Fig. 6.4, the dynamic chirp was estimated from the difference of the linewidths of the lasing mode with and without superimposing a modulating current. The evaluated chirp for TI-QD and QW lasers versus peak-to-peak modulation current are shown in Fig. 6.5(a) at a modulation frequency of 5 GHz and a DC bias of 28 mA. The chirp of the QW lasers varies between 1.6 and 2.9 Å and is comparable to previously reported values [114]. Figure 6.5(b) shows the chirp on the TI QD lasers versus frequency at a constant AC bias of 36 mA. As expected, TI-QD lasers show much lower chirp of

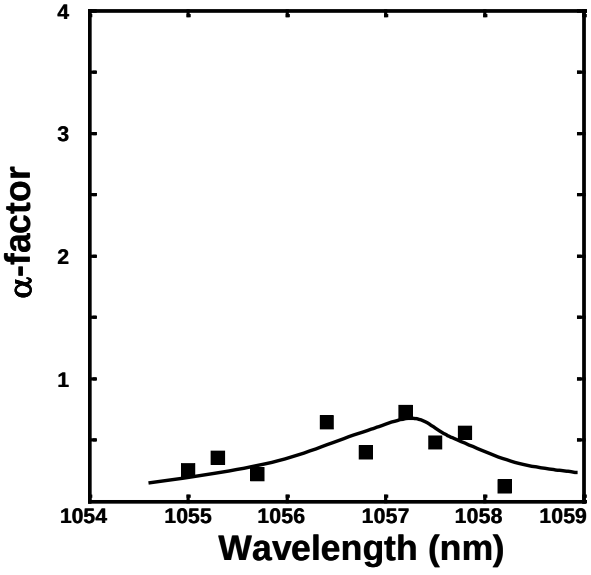

(a)

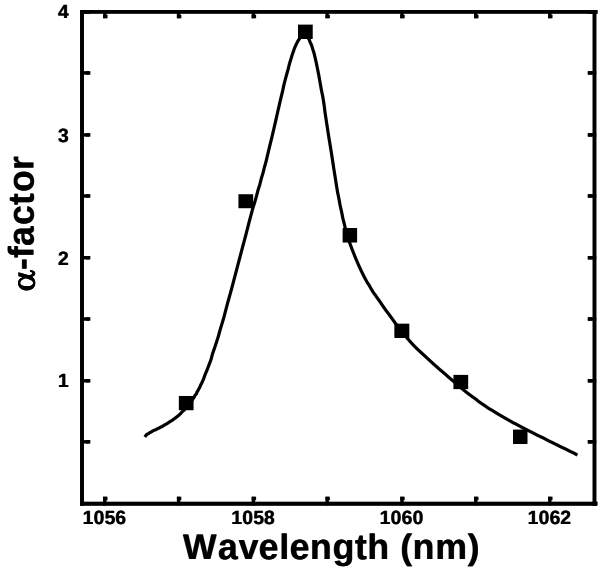

(b)

Fig. 6.3: Measured linewidth enhancement factor at subthreshold peak wavelengths of (a) undoped tunnel injection quantum dot laser and (b) SCH quantum well laser. The dashed lines are guides to the eye.

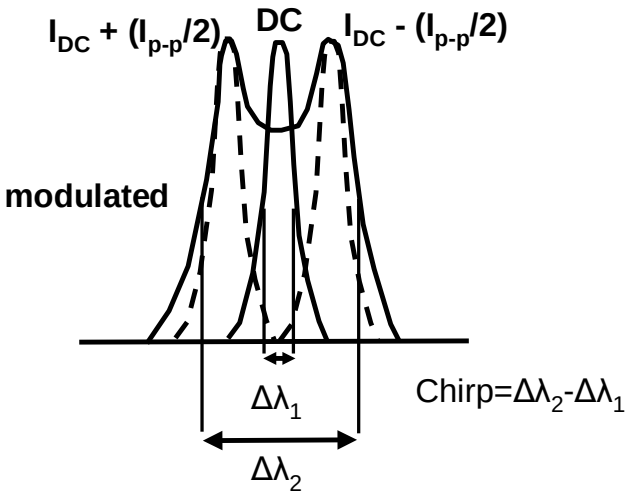

Fig. 6.4: Evaluation of chirp from the difference between the linewidths of modulated and DC lasing modes.

<0.6 Å at different AC biases and even at high frequencies.

6.3.4 Accelerated Lifetime Measurements

For any practical application of TI-QD lasers, long lifetime is a crucial subject of study. Lasers with high probability of catastrophic failure may not have any prospect of industrial and scientific applications. Very little work has been done on lifetime or reliability of QD lasers, in general, and of TI devices, in particular. Laser diode failures are generally attributed to three different mechanisms: (a) at 50-100% of *catastrophic optical damage* (COD), facet degradation is the cause of device failure; (b) at less than 50% COD, point defect gradually degrades the performance of the device; and (c) dark-line defects (DLD) are power independent sources of sudden failure [115]. In low-quality grown heterostructures, DLDs propagate into the active region in the first few hours of operation and dramatically decrease the efficiency of the devices.

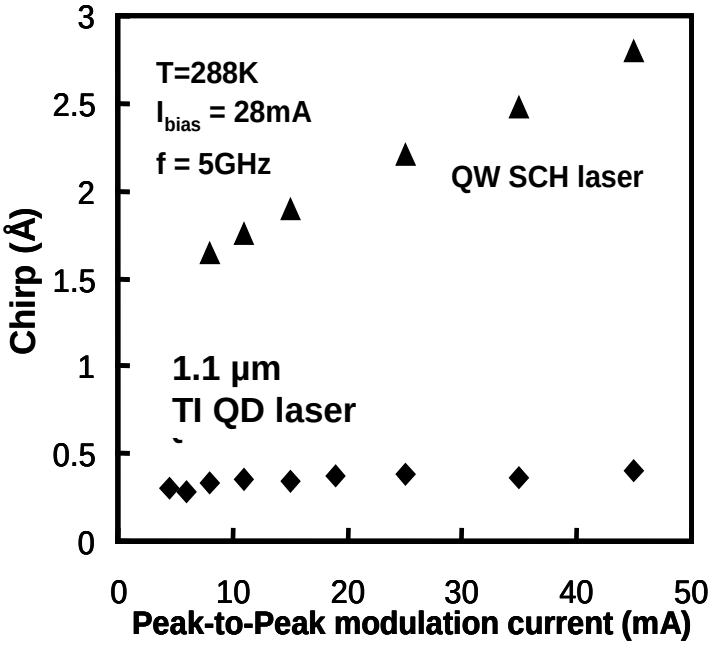

(a)

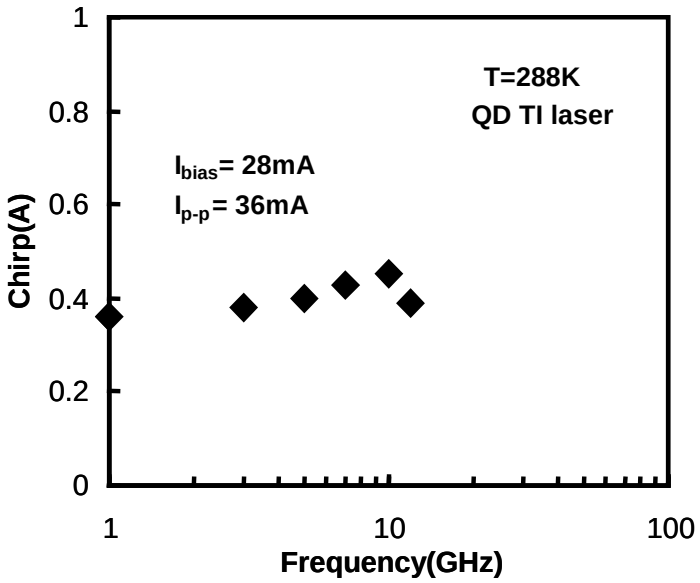

(b)

Fig. 6.5: (a) Measured chirp for undoped tunnel injection quantum dot laser and SCH quantum well laser at different peak-to-peak modulation currents; (b) chirp versus frequency in undoped tunnel injection quantum dot laser.

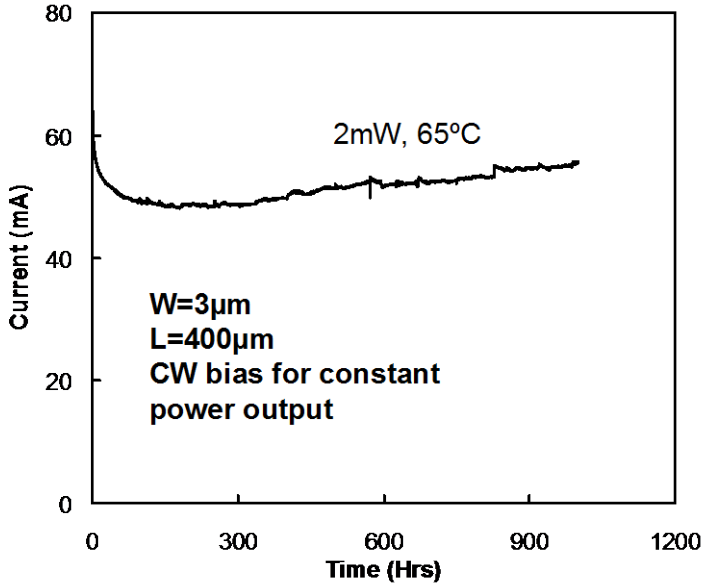

Fig. 6.6: 1000-hour lifetime measurements on ridge waveguide 1.1 µm undoped tunnel injection quantum dot lasers with constant continuous wave 2 mW power at 65°C.

Accelerated lifetime measurement with CW driving current at constant optical power is the standard method of studying lifetime of semiconductor lasers below half COD, where lifetime is defined as when the current becomes twice the initial value. Preliminary lifetime measurements on undoped TI-QD lasers was performed, and these measurements indicate the prospect for long lifetimes in QD lasers. 1000-hour measurements are done at 65°C to accelerate the degradation. The lasers are CW biased, and light output is fed into the feedback loop to keep the output power fixed. Fig. 6.6 shows the variation of the current with time for fixed output power at different ambient temperatures. During the initial period of the testing, annealing dominates degradation and,a reduction in current is observed during the first 50 hours.

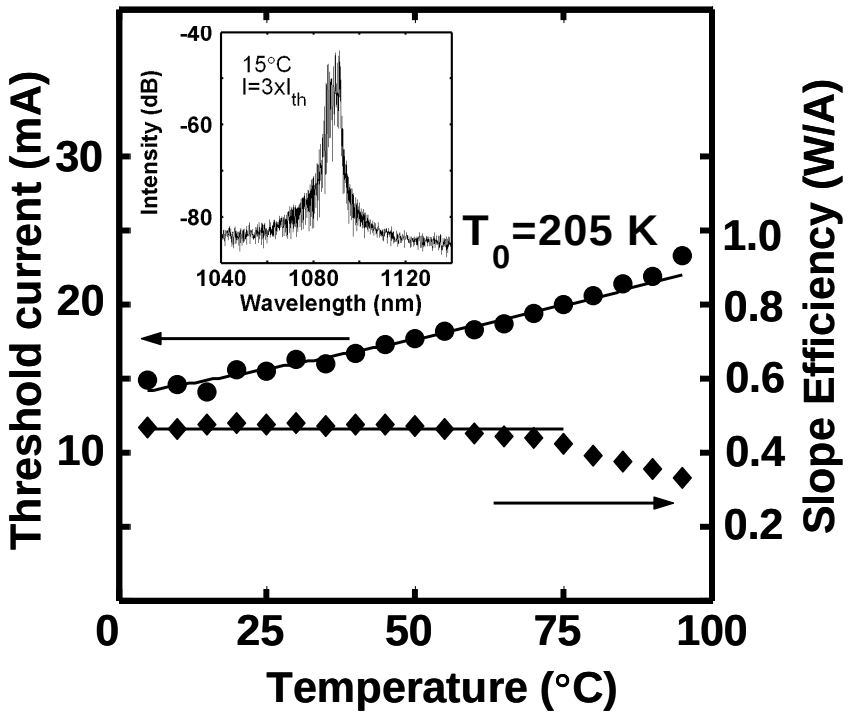

Fig. 6.7: Variation of the threshold current and slope efficiency of 200×3 μm^2 single-mode 1.1 μm p-doped tunnel injection lasers with temperature. The inset shows the output spectrum of the laser at 3 times the threshold current.

6.4 Characteristics of 1.1 μm p-Doped Tunnel Injection Lasers

6.4.1 DC Characteristics

Light-current (L-I) measurements were made with the devices mounted on a Cu heat-sink, whose temperature was stabilized with a Peltier cooler. Pulsed biased (1μs, 10 kHz) L-I measurements were performed on 1.1 μm TI-QD p-doped as-cleaved 200×3 μm^2 single-mode lasers. As the threshold current versus temperature plot in Fig. 6.7 indicates T_0~205 K from 5 to 95°C and slope efficiency of 0.465 W/A can be extracted for the devices. The inset shows the output spectrum of the device lasing at about 1090 nm.

6.4.2 Small-Signal Modulation Response

The small-signal modulation response of the lasers was measured with the high-speed measurement setup described in Section 3.4. The modulation response for the 1.1 μm p-doped TI QD lasers is shown in Fig. 6.8(a). The measurements were made under pulsed bias. The maximum f_{-3dB} measured for an injection bias of $6.7\times I_{th}$ is ~24.5 GHz, which is higher than the undoped sample and is indeed the highest modulation bandwidth reported to date in any QD laser. The resonance frequency of the devices is plotted versus $(I - I_{th})^{1/2}$ in Fig. 6.8(b), from which a modulation efficiency of 2 GHz/mA$^{1/2}$ is derived. A differential gain, $dg/dn=3\times10^{-14}$ cm^{-2} is derived in these devices from the measured resonance frequencies and a calculated optical confinement factor of $\Gamma=2.5\times10^{-3}$ (see Eqn. 5.1). From the damping factor of the best fit to the modulation response, a gain compression factor $\varepsilon=4\times10^{-16}$ cm^3 is also obtained for these devices. All of these parameters show improvement compared to the undoped samples, which may be attributed to the slight impact of p-doping in the modulation characteristics of gigahertz enhancement of modulation QD lasers. As discussed in Section 5.2, only slight bandwidth improvement was observed upon p-doping (from 8 to 11 GHz) in conventional 1.1 μm SCH lasers, which is due to the slight increase of gain and differential gain by the extra holes provided from the doped barriers.

6.4.3 Linewidth Enhancement Factor and Chirp

The modulation characteristics of p-doped TI lasers presented in the previous subsection indicate that these devices have enormous potential for high-speed fiber optic communication LAN and MAN systems. Therefore, important dynamic figures of

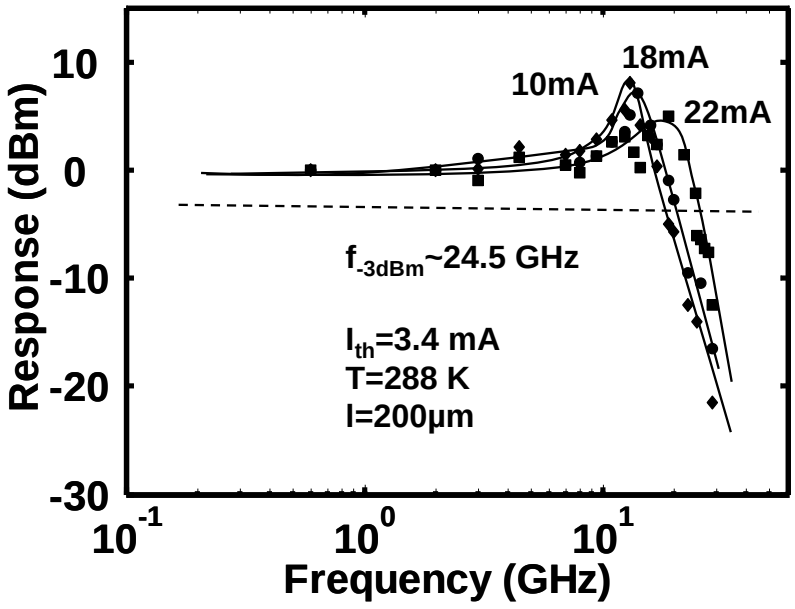

(a)

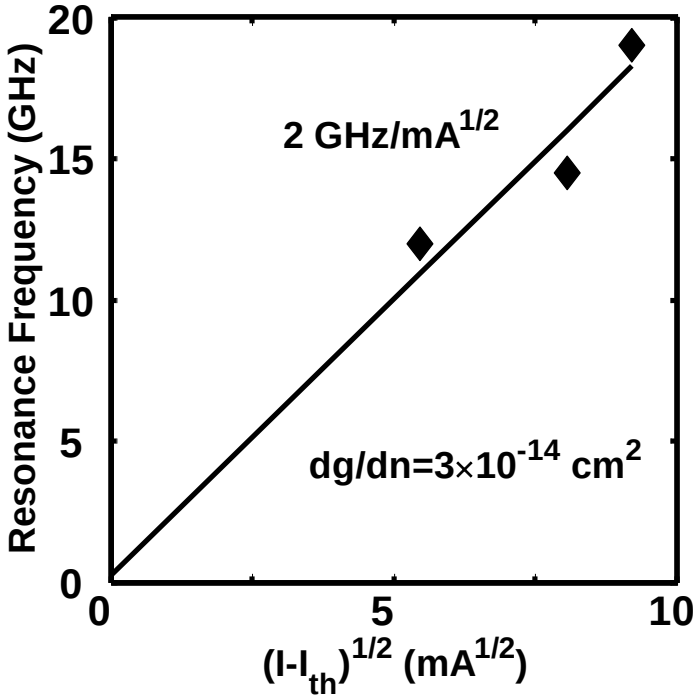

(b)

Fig. 6.8: (a) Modulation response of single-mode 1.1 μm p-doped quantum dot tunnel injection lasers at different biases; (b) resonance frequency of the lasers versus $\sqrt{I - I_{th}}$.

merit for such applications have been also studied in the present lasers, namely, linewidth enhancement factor, α, and dynamic chirp. The α-factor is a critical parameter in semiconductor lasers, since the laser linewidth is (1+ α^2) times larger than the Shawlow-Townes fundamental limit. α is inversely proportional to the differential gain, and it is evident that large differential gains are attainable in QD lasers. I described before that low α-factors can be expected and has indeed been reported in conventional QD lasers [28]. Similar to the description in Section 5.3, the linewidth enhancement factor of the TI lasers was measured by the Hakki-Paoli method below threshold by using the formula: $\alpha = \frac{2}{\partial\lambda} \frac{\Delta\lambda_i}{\Delta\{\ln[(\sqrt{r_i}-1)(\sqrt{r_i}+1)^{-1}]\}}$, where $\partial\lambda$ is the mode spacing, r_i is the peak-to-averaged valleys ratio of the *i*th competing mode in the optical spectrum, and ΔN is the incremental carrier density for two differential bias values [96]. As can be seen in Fig. 6.9(a), upon varying the voltage increment, ΔV, from a differential value of 0.1 to values as high as 0.5 V, no spectral differential shift of the longitudinal laser peaks, $\Delta\lambda_i$, was observed in p-doped 1.1 μm TI lasers. Therefore, α is virtually zero in these lasers (within the resolution of our spectrum analyzer).

Finally, since chirp is directly proportional to α, TI-QD lasers are expected to have ultra-low chirp. We measured the chirp in 1.1 μm p-doped TI-QD lasers similar to the description for undoped lasers in Section 6.3.3. As is evident from Fig. 6.9(b), for frequency ranging from 1 to 15 GHz and at a constant AC bias of 22 mA, the p-doped TI-QD lasers show a negligible chirp of <0.4 Å at all frequencies. It can be clearly concluded that TI-QD lasers have dynamic properties which surpass those of QW lasers for 1.0-1.3 μm optical communication systems.

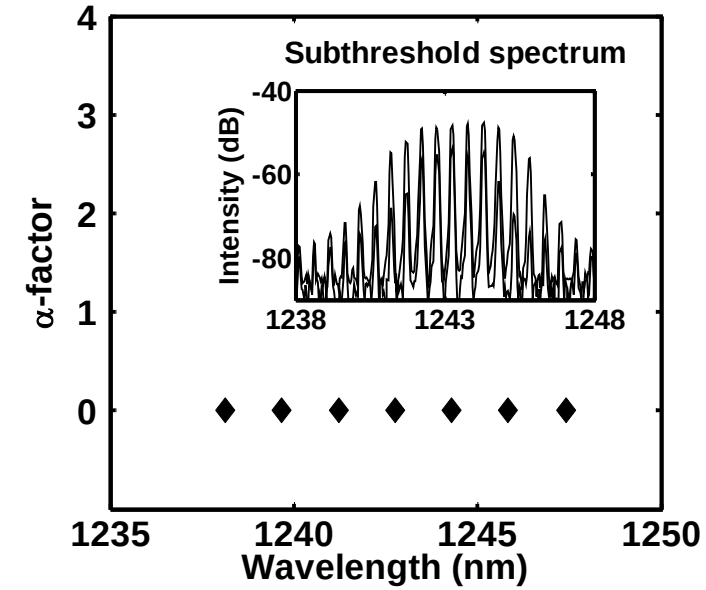

(a)

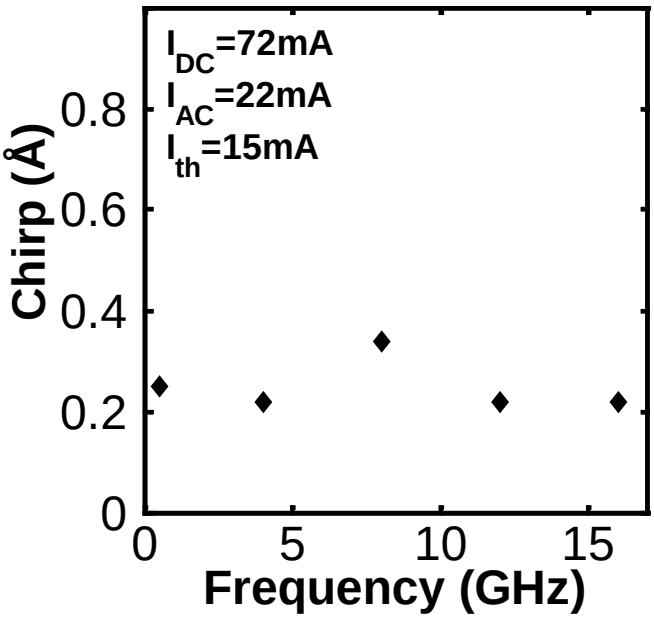

(b)

Fig. 6.9: (a) Linewidth enhancement factor at the peak wavelengths of the subthreshold spectrum of p-doped 1.1 μm tunnel injection quantum dot lasers. The inset shows two differentially close measured subthreshold spectra with bias voltage difference, ΔV ~0.1 V; (b) measured chirp for p-doped 1.1 μm tunnel injection quantum dot lasers versus frequency of the modulating AC signal.

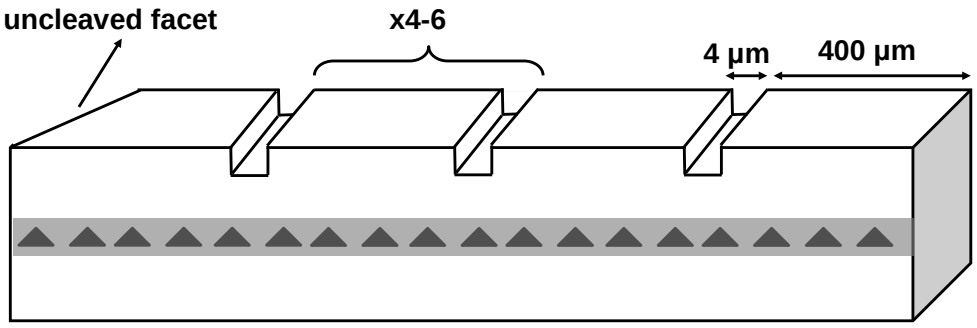

Fig. 6.10: Schematic of the fabricated multi-section device for optical modal gain measurements.

6.4.4 Measurement of Modal Gain

It is evident from the previous section that p-doped TI QD lasers have very promising modulation bandwidths and dynamic properties. A closely related quantity to assess in these lasers is the net modal gain, g. Net modal gain can be extracted from the Hakki-Paoli method [100], as expressed in Eqn. 5.2, from the peak to averaged-valleys ratio of competing modes in the optical spectrum. However, this method is only applicable below threshold. Extracting modal gain by transforming the spontaneous emission, known as the Henry technique [116], is another way of obtaining modal gain. The Henry technique is not only a subthreshold method, but also requires *indirect* calculation of the Fermi-level energy separation. Variable-stripe-length technique is an interesting method to directly acquire the absolute value of net modal gain spectrum from the amplified spontaneous emission (ASE) intensity [117],[118]. The ASE intensity, I, from a point source with distance L from the facet can be expressed in terms of g and the intensity of the spontaneous emission, I_{sp}, as:

$$I = \frac{I_{sp}}{g}(e^{gL} - 1). \qquad (6.1)$$

Eqn. 6.1 is valid for long stripes compared to stripe width and for a single-pass gain medium. The single-pass condition can be achieved by a long absorption region as well as antireflection coating [117]; growing on a misoriented substrate [118]; or, as has been performed in this work, by creating uncleaved facet at the end of the absorption region. If the ASE intensities of stripe lengths L and $2L$ are compared, it is straightforward to show from Eqn. 6.1, that the absolute value of g can be directly evaluated from:

$$g = \frac{1}{L}\ln\left(\frac{I_{2L}}{I_L} - 1\right). \qquad (6.2)$$

Schematic of the multi-section device for gain measurements is shown in Fig. 6.10. The heterostructure of the device is identical to the p-doped TI QD lasers in Fig. 6.1(a). 400×40 μm^2 p-contact sections, with 4 μm spacers between them, are created by metallization. The spacers are turned into trenches by self-aligned etching of the top p^+-GaAs contact layer in order to maximize the electrical isolation of the sections, while the AlGaAs cladding is not etched to minimize the damage to the ridge waveguide. According to Eqn. 6.2, only the two sections adjacent to the cleaved facet were biased, while 5-7 unbiased sections and the uncleaved facet are to minimize the optical feedback. The ASE intensity of lengths L and $2L$ (400 and 800 μm) were measured by a HP 70952B optical spectrum analyzer at 293 K and the net modal gain, g, was directly evaluated form Eqn. 6.2, which is presented in Fig. 6.11(a) versus wavelength for three different current densities with gain peaks around 1090 nm. The peak modal gain versus current is plotted in Fig. 6.11(b). It is evident that peak gains as high as 57 cm^{-1} are obtained in the TI lasers with three layers of quantum dots. Similar multisection device measurements on conventional lasers with three layers of dots have resulted in g~14 cm^{-1} at 300 K [42]. Other reported experimental and calculated values of modal gain in

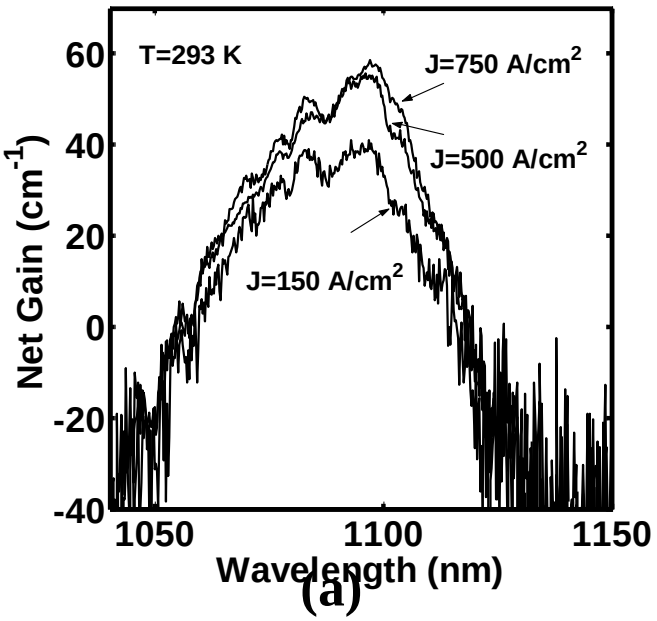

(a)

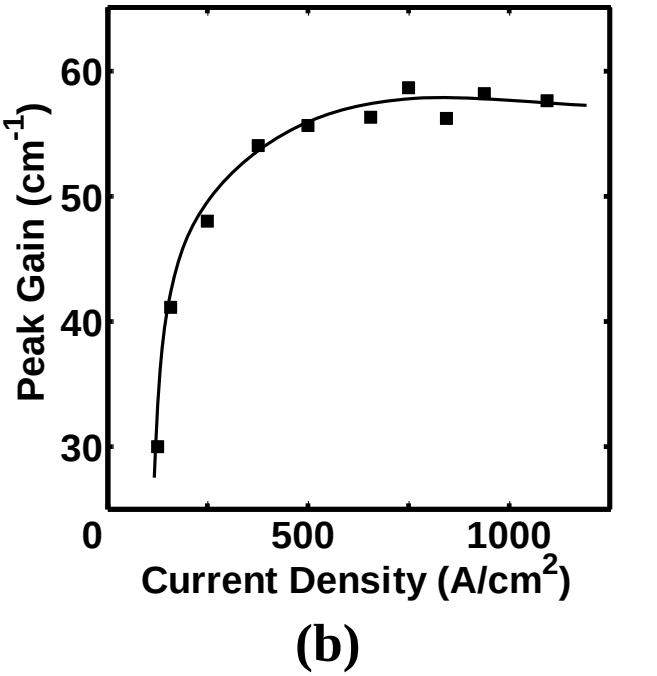

(b)

Fig. 6.11: (a) Measured modal gain versus wavelength at three different biases in 1.1 μm p-doped tunnel injection quantum dot lasers; (b) peak optical gain of the same devices at different current densities. The solid line is guide to the eye.

conventional QD lasers are from 5 to 12 cm^{-1} per dot layer [26],[82]. Therefore, the reported value of 19 cm^{-1} per QD layer in this work for TI p-doped lasers is a factor of ~1.5-4 higher than previous data for conventional QD lasers. This can be attributed to minimization of hot carrier effects and decrease of wetting layer and higher states occupation leading to higher population of the ground states in TI lasers. Analysis of the measured gain in conventional QD lasers and comparison with calculated occupancies of the electron and hole ground states has confirmed that the population inversion factor, f_n-$f_{p,}$ in Eqn. 2.7, and modal gain, are limited to as low as 20% of the saturated value at room temperature [42]. This is due to the existence of the wetting layer with a much higher density of states and the thermal broadening of hole energy levels, as was discussed in detail in Section 2.4. Therefore, the high measured values of modal gain in this work correspond to as high as ~80% of the maximum attainable gain of QDs. This high occupation confirms efficient injection of cold carriers by phonon-assisted tunneling into the dot ground state and is in agreement with the measured large differential gain from the modulation response in the Section 6.4.2.

6.5 Summary

High-performance InGaAs undoped and p-doped TI self-organized QD lasers emitting at 1.1 μm are demonstrated. Undoped tunnel injection QD lasers have ~22 GHz small-signal modulation bandwidth. The measured near-field pattern, linewidth enhancement factor and dynamic chirp of TI-QD lasers were compared with those of SCH QW lasers. The near-field measurements show that significant filamentation occurs in QW lasers at biases above twice the threshold current. Such filamentation is not

observed in the quantum dot lasers even at high biases. The linewidth enhancement factor of the undoped 1.1 μm TI laser is ~0.73 at lasing peak, and its dynamic chirp is <0.6 Å at various frequencies and AC biases, which is superior to respective values of ~3.7 and 1.6-3.0 Å in the SCH QW lasers. Higher modulation bandwidth (~25 GHz) and differential gain (3×10^{-14} cm^2) are measured in 1.1 μm p-doped TI lasers with a characteristic temperature, T_0, of 205 K in the temperature range of 5 to 95°C. The 1.1 μm p-doped TI-QD lasers exhibit zero linewidth enhancement factor ($\alpha\sim0$) and negligible chirp (<0.4 Å), a low gain compression factor of 4×10^{-16} cm^3, and a high modal gain of 19 cm^{-1} per dot layer. It is amply evident that the characteristics of p-doped TI-QD lasers are superior to undoped TI-QD, p-doped conventional, as well as SCH QW lasers.

CHAPTER VII

MAGNETIC PROPERTIES OF GaMnAs AND InMnAs DILUTED MAGNETIC SEMICONDUCTORS

7.1 Introduction

The importance of spintronics for electronics and optoelectronics was described in Section 1.4. As explained therein, exploiting conventional ferromagnetic materials such as transition metals for injection of spin-polarized carriers into semiconductor devices has not shown to be successful due to spin decoherence at the metal/semiconductor interface. Diluted magnetic semiconductors (DMS's) are alloys of nonmagnetic semiconductors, e.g., GaAs, CdTe and ZnSe, in which periodic arrays of magnetic elements, e.g., manganese, are present. In other words, ferromagnetic and semiconducting properties coexist in DMS materials, thus they can be readily used in spintronic devices with standard epitaxial growth and device fabrication techniques. II-VI-based (CdTe and ZnSe) DMS's were initially being investigated, but it is difficult to dope these materials for device application [41]. Manganese-diluted alloys of GaAs and InAs are promising DMS's for spintronic applications. Interestingly, the Mn ions not only create ferromagnetism in the GaAs host material, but also act as p-type dopants. Therefore, GaMnAs layers can be used as hole spin-aligners in spintronic devices such as spin-polarized LEDs, as discussed in the next Chapter. In this Chapter, the origin of

ferromagnetism and epitaxial growth of GaMnAs are reviewed, followed by ferromagnetic properties of various GaMnAs/GaAs heterostructures. Mn-doped InAs quantum dots are another type of DMS material with Curie temperatures above room temperature, and are the subject of the last section of this Chapter.

7.2 Origin of Ferromagnetism in Mn-Doped (In)GaAs Heterostructures

Magnetism of atomic and solid state materials is a quantum mechanical property which originates from the angular momentum, **L**, and spin of electrons, **S**, and their internal quantum-mechanical interaction, as well as their response to an external magnetic field. The relation between magnetization, **M**, and the macroscopic magnetic field, **B**, is defined through the magnetic susceptibility per unit volume, χ, i.e.,

$$\mathbf{M} = \frac{\chi}{\mu_0}\mathbf{B}. \qquad (7.1)$$

Different substances can attain different magnetic characteristics, which can be mainly categorized into diamagnetism, paramagnetism, ferromagnetism, antiferromagnetism, and ferrimagnetism. In diamagnetic substances, the magnetic susceptibility is *negative*, and simply originates from the induced magnetic moment of the electrons orbiting around a nucleus, the precession of which is *opposite* to the applied field according to Lenz's law. As shown in Fig. 7.1, diamagnetism is not temperature dependent. It is observable in substances such as inert gases, where the total angular momentum, **J**=**L**+**S**, is zero. Paramagnetic substances have positive magnetic susceptibility due to the exchange interaction Hamiltonian of nonzero **J** with **B**:

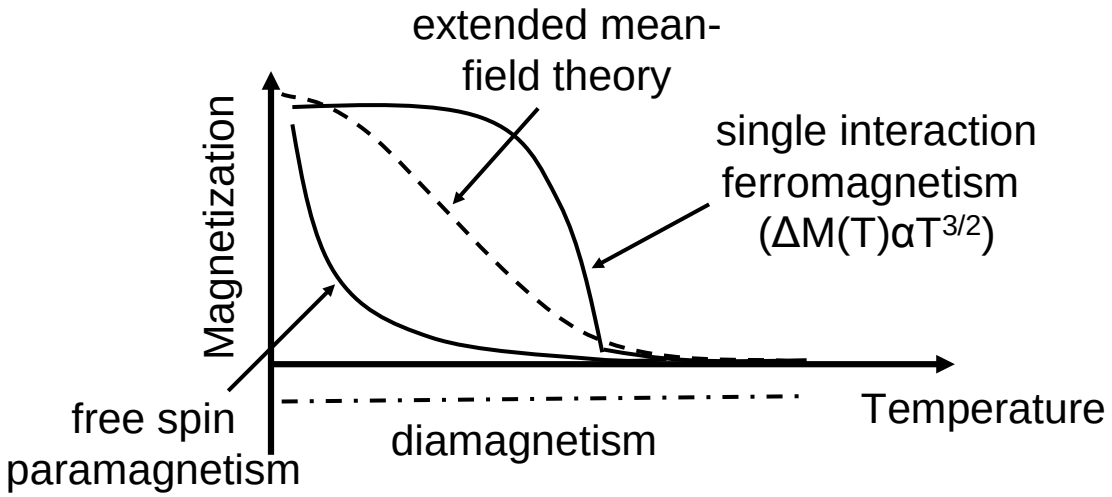

Fig. 7.1: Different characteristic modes of magnetization and their temperature dependences.

$$H = -g\mu_B \mathbf{J}\cdot\mathbf{B}, \qquad (7.2)$$

where μ_B is the Bohr momentum. In Boltzmann statistic, it can be shown that the temperature dependence of free spin paramagnetic susceptibility, depicted in Fig. 7.1, follows [119]

$$\chi = \frac{C}{T}, \qquad (7.3)$$

where C is the Curie constant. Examples of paramagnetic materials are free atoms and ions with partially filled inner shells such as Mn^{2+} and some metals.

In ferro-, antiferro-, and ferri-magnetic materials a spontaneous magnetic moment exists even without applying an external field, which can only happen in an ordered array of microscopic moments in magnetic domains. These three ordered arrangements are schematically shown in Fig. 7.2. I will only focus on describing ferromagnetism.

If an internal interaction between spin and/or angular momentum tends to order the magnetic moments of a paramagnetic material and overcome the thermal agitation, a

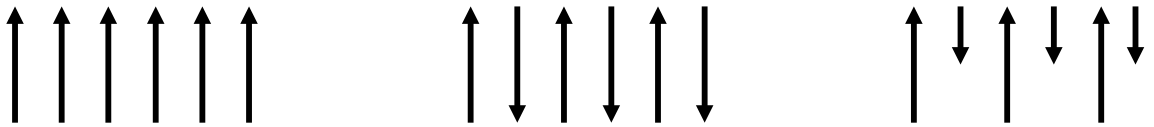

Fig. 7.2: Simple schematic of ferromagnetic, antiferromagnetic and ferrimagnetic orders.

ferromagnet is obtained below a critical temperature called the Curie temperature, T_c. The exchange field can be treated as an equivalent magnetic field, $\mathbf{B}_E$, thus Eqn. 7.1 is modified to:

$$\mathbf{M} = \frac{\chi}{\mu_0}(\mathbf{B} + \mathbf{B}_E). \qquad (7.4)$$

If in the mean-free approximation, we further assume that $\mathbf{B}_E$ is proportional to $\mathbf{M}$, Eqn. 7.3 will be modified to:

$$\chi = \frac{C}{T - T_c}. \qquad (7.5)$$

This is called the Curie-Weiss law and is a fair analytical model for describing magnetization at $T>T_c$. Below T_c, the temperature dependence is more complicated but, as shown in Fig. 7.1, generally follows [119]*:*

$$\Delta M(T) = M(0) - M(T) \propto T^{3/2}. \qquad (7.6)$$

The single ferromagnetic exchange interaction between atoms *i* and *j* can be quantum-mechanically described by the Heisenberg model:

$$H = -2J\mathbf{S}_i \cdot \mathbf{S}_j, \qquad (7.7)$$

where *J* is the exchange integral.

After this general review of magnetic modes, I focus on diluted magnetic semiconductors, in particular GaMnAs. Introducing a small concentration of magnetic elements into a semiconductor matrix can lead to diluted magnetic semiconductors. Diluted Mn-doped II-VI and II–V semiconductor compounds, e.g., Zn(Mn)O and Ga(Mn)As, are ferromagnetic. In GaMnAs, manganese (Mn: $[Ar]3d^5 4s^2$) impurities reside primarily in Ga sites (Mn_{Ga}) in the GaAs lattice, where they function as both an acceptor (Mn^{2+}) and as a source of localized magnetic moment. The bound hole orbits around the Mn^{2+} ions with a p-type ionization energy of 113 meV and a Bohr radius of 10Å [120]. Electron-spin resonance studies show that manganese-hole (Mn-*h*) complexes are formed by an antiferromagnetic coupling force, as delocalized ${}^4S_{3/2}$ holes and $A^-(3d^5)$ Mn cores give a total angular momentum of J=1, which remains the ground state up to very high fields of 50 T [121]. The corresponding Zeeman splitting of the three m_j=0, ±1 levels of the Mn-*h* complexes, with a *g*-factor of 2.77 and mediated by hole-hole coupling, is the origin of ferromagnetism in GaMnAs. It is now understood that ferromagnetism in GaMnAs is mediated by holes through Ruderman-Kittel-Kasuya-Yosida (RKKY) interaction, i.e., the exchange integral J in Eqn. 7.7 is proportional to *p-d* exchange between holes and Mn *3d* states, J_{pd} [122]. Alternatively, the coupled interaction Hamiltonians of Eqn. 7.2 and 7.7 for holes and Mn ions need to be considered. The corresponding "extended mean-field Hamiltonians" for a hole spin, **j**, and a Mn spin, **S**, are [123]:

$$\begin{aligned} H^h &= \sum_l J_l^{hh}\,\mathbf{j}\cdot\mathbf{j}_l + J^{Mnh}\,\mathbf{j}\cdot\mathbf{S} + g_h\mu_B\mathbf{J}\cdot\mathbf{B}, \\ H^{Mn} &= J^{Mnh}\,\mathbf{j}\cdot\mathbf{S} + g_{Mn}\mu_B\mathbf{J}\cdot\mathbf{B}, \end{aligned} \tag{7.8}$$

where l is the summation index in nearest lattice sites. Assuming the carriers are responsible for ferromagnetism, $J^{hh}>0$. Direct Mn-Mn interaction is negligible and is not considered in Eqn. 7.8. Hole-Mn coupling is antiferromagnetic ($J^{Mnh}<0$). The relative weight of J^{hh} and J^{Mnh} depends on the quality of the GaMnAs layer (growth and annealing conditions) and thickness of the sample, and determines the variation of magnetism with temperature. For instance, if the ferromagnetic term dominates, a "single ferromagnetic exchange" behavior (see Eqn. 7.6) is observed. If the magnitude of J^{Mnh} is about half of J^{hh}, the antiferromagnetic term is considerable and a behavior similar to the schematic dashed lines in Fig. 7.1 is observed [120], as we will see experimentally in Section 7.4. Finally, Dietl *et al.* [124] predicted that increase of Mn composition, x, and hole concentration, p, can increase the Curie temperature according to the relation:

$$T_c \propto xp^{1/3}. \qquad (7.9)$$

It is noteworthy that manganese antisites (Mn_{As}) and interstitials (Mn_I) not only hamper ferromagnetism but also act as n-dopants and cause self-compensation (~30%). Arsenic antisites (As_{Ga}) have similar self-compensation effects [125]. We will see in Section 7.4.2 that these compensation centers can be removed by thermal annealing.

7.3 Molecular Beam Epitaxial Growth of GaMnAs/GaAs Heterojunctions

Due to the low solubility of Mn in III-V materials, epitaxial growth of uniform GaMnAs films on GaAs is not possible at equilibrium. Furthermore, MnAs has a large lattice mismatch with GaAs and possesses a NiAs-type hexagonal lattice structure. Depending on the composition of Mn, x, and the substrate growth temperature, T_s, four phases can be recognized [41]: (a) at T_s>280-300°C epitaxial growth is inhibited due to

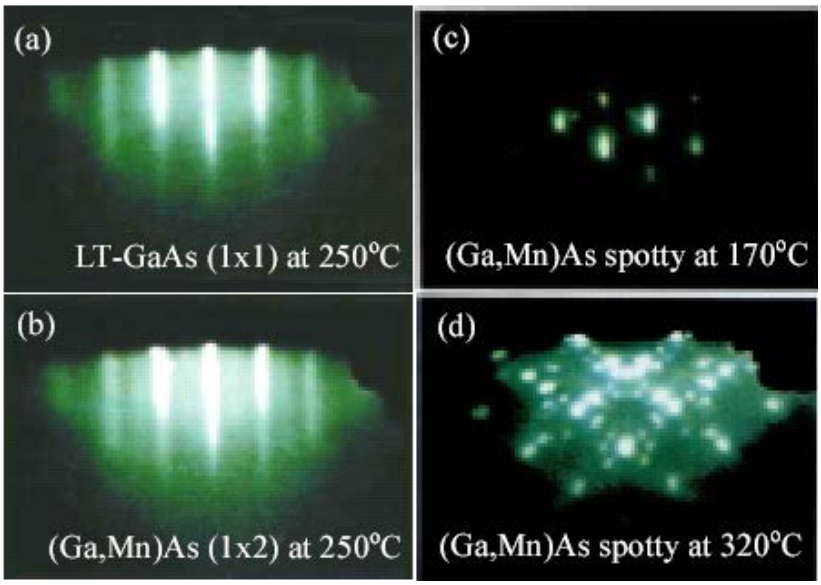

Fig. 7.3: The RHEED pattern during epitaxial growth of Ga(Mn)As at different indicated growth temperatures: (a) and (b) show low temperature GaAs and GaMnAs with streaky patterns, respectively; (c) and (d) show spotty patterns at too low and too high temperatures, respectively.

the mentioned low solubility of Mn and MnAs clusters are formed; (b) surface roughening is significant at T_s<170°C and for 0.01<x<0.06; (c) at very low and very high x and intermediate T_s, insulating GaMnAs is formed; (d) it is only at 0.01<x<0.06 and a non-equilibrium growth temperature of 180-280°C that a single-crystal alloy can be successfully grown. Partial ferromagnetism was observed in low temperature (LT) molecular beam epitaxy (MBE) growth of InMnAs films on GaAs in 1989 [126]. GaMnAs diluted magnetic semiconductors was first demonstrated by the same technique in 1996 [127]. Low growth rates are required to inhibit formation of MnAs clusters. Low As flux avoids excess As (As_I) formation at LT growth. It is noteworthy that growth interruption leads to formation of MnAs clusters.

In this work, several GaMnAs films of varying thickness and Mn composition were grown by LT-MBE on (001) semi-insulating GaAs substrates in a Varian GEN-II

chamber using a relatively low As_4:Ga beam equivalent pressure (BEP) ratio (~16:1) and a growth temperature in the range 240-270˚C. A radiatively-coupled thermocouple is used to monitor the temperature of the substrate which is In-mounted to a molybdenum block during growth. The GaMnAs film is deposited over a 100 nm LT-GaAs buffer layer after lowering the temperature from the initial 150-400 nm GaAs buffer layer grown at 600˚C. The Mn composition is calibrated using secondary ion mass spectroscopy (SIMS). Reflection high energy electron diffraction (RHEED) is a very crucial *in situ* monitoring tool in the LT-MBE growth of GaMnAs. During a typical growth, the initial GaAs buffer grown at equilibrium (600˚C) shows the well-known (2×4) reconstruction pattern. As shown in Fig. 7.3(a), this pattern changes into a (1×1) pattern in the LT (250˚C) GaAs buffer. Upon opening the Mn cell shutter at 250˚C with a growth rate of about 0.6 μm per hour, the surface reconstruction pattern changes into (1×2) which should persist during a stable growth (Fig. 7.3(b)), unless x is too high (>0.06) or T_s is marginally high. A spotty RHEED pattern obtained at very low T_s is shown in Fig. 7.3(c), which is an indication of significant surface roughness. The formation of MnAs clusters with NiAs lattice structure is evident in the RHEED pattern of Fig. 7.3(d).

7.4 Magnetic Properties of GaMnAs/GaAs Heterojunctions

Several GaMnAs films of varying thickness and Mn composition were grown by LT-MBE as discussed in the previous section. Direct, in-plane secondary quantum interference device (SQUID) magnetometery was employed to characterize the samples. Effects of thermal annealing and co-doping with Be on single- and multi-layers of

GaMnAs/GaAs heterostructures were also studied. The results are presented and discussed in the following subsections.

7.4.1 As-Grown Bulk GaMnAs Layers

A systematic study of magnetization in bulk GaMnAs layers with a nominal thickness of 150 nm was performed. Growth temperature is crucial in achieving high Curie temperature, T_c. As can be seen in Fig. 7.4(a), T_c increases from 70 K to 100 K by increasing T_s by only 10˚C (from 240 to 250˚C). Also, by comparing the shape of the magnetization versus T with what is schematically shown in Fig. 7.1, it is evident that a single ferromagnetic exchange interaction is more dominant for the sample grown at higher T_s, which indicates that hole mediated ferromagnetic order is more dominant than hole-Mn antiferromagnetic coupling in Eqn. 7.8. It has to be noted that SQUID measurements confirm the absence of MnAs clusters with T_c>300 K. Hysteresis measurements (inset of Fig. 7.4(a)) indicate the presence of ferromagnetic order in GaMnAs at low temperatures as evidenced by a sharp, square hysteresis in the film's magnetization versus applied magnetic field. As shown in Fig. 7.4(b), the Curie temperature increases with Mn composition from T_c~70 K for 150 nm thick $Ga_{0.97}Mn_{0.03}As$ to ~100 K for 150 nm thick $Ga_{0.95}Mn_{0.05}As$. This trend is consistent with Eqn. 7.9 and the corresponding existing theories describing hole-mediated ferromagnetism which suggest that T_c scales with both the Mn and hole concentrations [124],[128],[129].

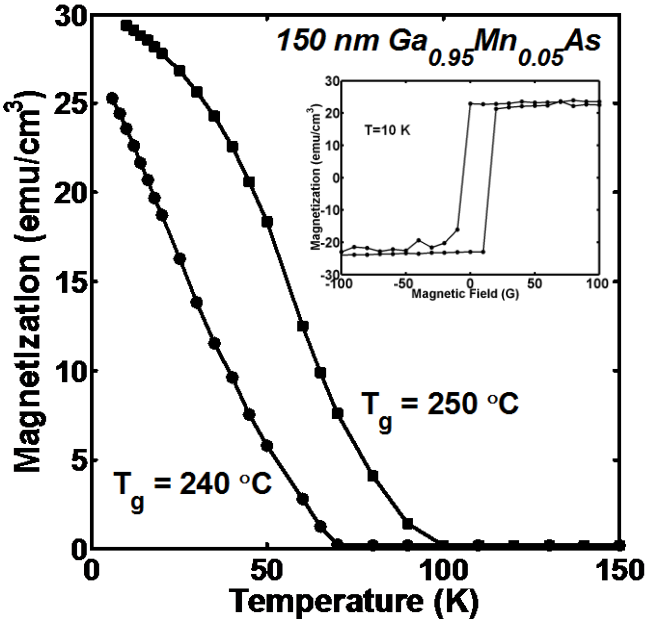

(a)

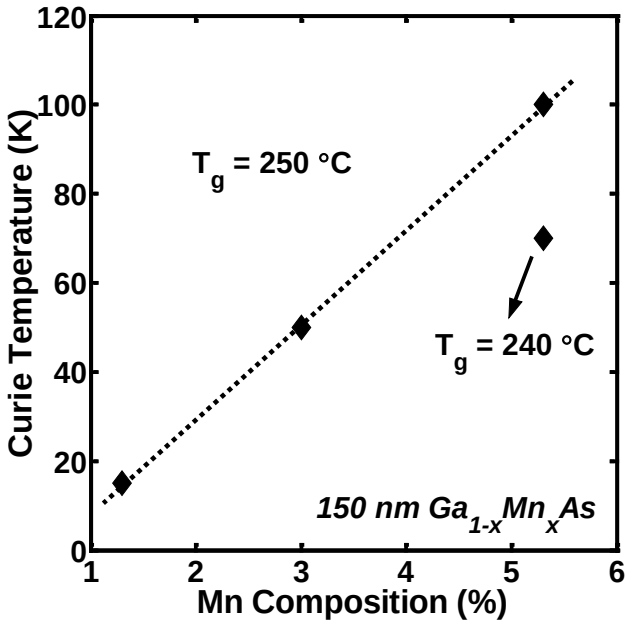

(b)

Fig. 7.4: (a) Magnetic moment versus temperature for a 150 nm thick $Ga_{0.95}Mn_{0.05}As$ films grown at different substrate temperatures, measured using low-field (50 G) SQUID magnetometry. The inset shows the magnetic moment versus field for the sample grown at 250°C, measured at 20 K; (b) the Curie temperature versus Mn composition of the same samples.

7.4.2 Effect of Thermal Annealing and Be Co-Doping on Bulk GaMnAs Layers

Thermal annealing has been suggested as a means of improving Curie temperature in GaMnAs layers grown by LT MBE [130],[131]. Annealing increases the hole density of as-grown samples. A two step process of low-temperature epitaxial growth followed by annealing provides the easiest means to maximize T_c of GaMnAs. This procedure provides a convenient alternative to the difficult task of optimizing the growth conditions alone. Different defects such as As_{Ga}, As_I, Mn_I and Ga vacancies can be formed during the MBE growth of GaMnAs samples. Positively charged Mn_I is highly mobile and occupies an interstitial site next to Mn_{Ga} and inactivates the acceptor. It is now understood that LT annealing breaks the weak Mn_I-Mn_{Ga} pair and Mn_I ions diffuse to substitutional sites or form clusters [132]. As_{Ga} is stable at LT and cannot be annealed through diffusion or evaporation. In this work, effect of annealing parameters, e.g., time and temperature, in a nitrogen ambient furnace was studied. Optimum annealing conditions are recognized to be for 60-90 minutes at 250˚C. Magnetization plots in Fig. 7.5 verify T_c improved from 70 K to ~ 100 K for $Ga_{0.95}Mn_{0.05}As$ samples grown at 240˚C. Similar to the above discussion on the effect of growth temperature, improvement in single ferromagnetic exchange interaction is evident upon annealing from the shape of the magnetization plots (see Section 7.2).

The properties of GaMnAs films co-doped with Be, an acceptor in GaAs was also investigated. Since the origin of ferromagnetism is hole mediated, increase of hole concentration, p, can increase the Curie temperature (Eqn. 7.9). The hole concentration produced by the Mn dopants is, however, limited due to heavy compensation by donor defects. Co-doping of Be can be perceived as a means of increasing p in GaMnAs layers

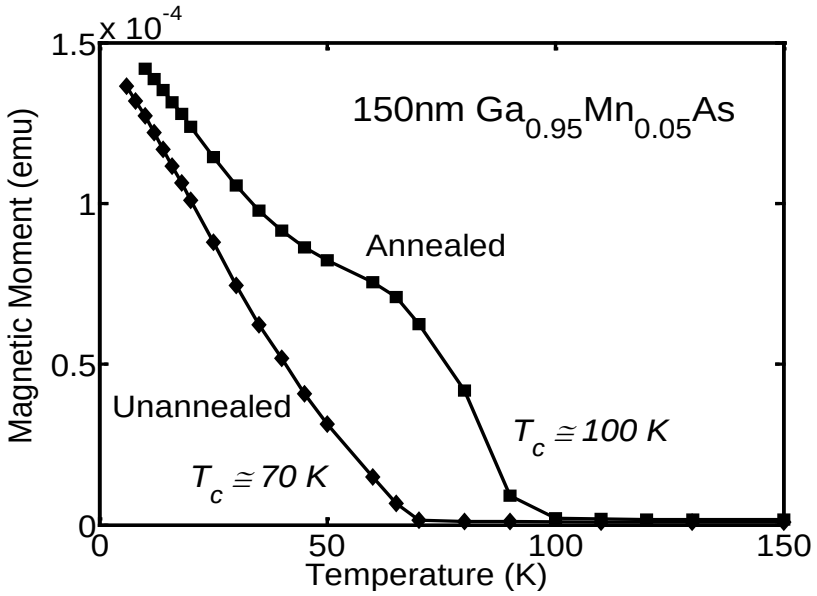

Fig. 7.5: Effect of thermal annealing at 250˚C for 90 min, on the Curie temperatures for a 150 nm thick $Ga_{0.95}Mn_{0.05}As$ films grown at 240˚C.

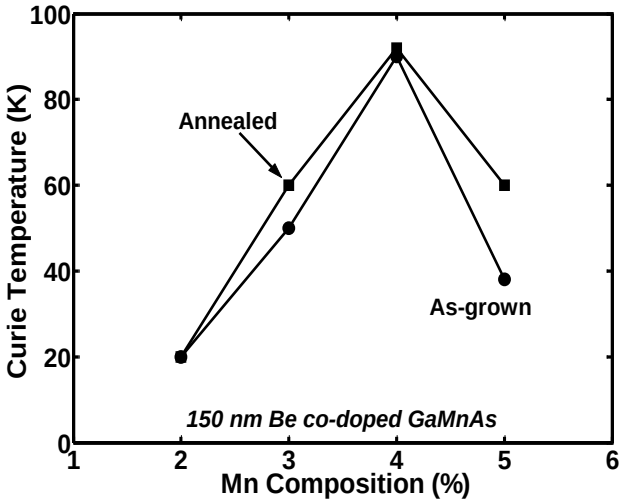

Fig. 7.6: Curie temperatures of as-grown and optimally annealed, 150 nm thick, Be co-doped GaMnAs films as determined from low-field (50 G) SQUID magnetometry.

[125]. The Curie temperature for 150 nm thick, Be co-doped GaMnAs films is plotted versus Mn atomic fraction in Fig. 7.6 for as-grown and optimally annealed samples. For the Be co-doped GaMnAs films considered in this investigation, saturation of the Curie

temperature occurs for a lower Mn composition at x=0.04 rather than x=0.05 as is typically observed for GaMnAs. Additionally, co-doped films do not exhibit Curie temperatures larger than those observed in GaMnAs. These observations support the view of a Fermi level induced saturation of the extrinsic carrier concentration owing to the formation of compensating native defects, as suggested by Lee *et al.* [125].

7.4.3 Thin GaMnAs Layers and GaMnAs/GaAs Multilayers

Thin GaMnAs films have been found to exhibit magnetic properties different from those of thicker layers [133],[134]. GaMnAs epilayers of thickness in the range of were grown by LT-MBE using a deposition temperature of T_s=240–280˚C and following a procedure similar to the one describe in Section 7.2 for the growth of 150 nm thick GaMnAs films. The as-grown layers were subjected to low-temperature post-growth annealing in nitrogen ambient for 60-90 min. The highest Curie temperature of 150 K was obtained for a 15 nm $Ga_{0.95}Mn_{0.05}As$ epilayer annealed for 250˚C for 60 min. The magnetic moment versus both temperature and field for this sample is shown in Fig. 7.7. Other groups have observed a similar enhancement of the Curie temperature in thin GaMnAs layers after low-temperature annealing and have attributed the increase to a higher free hole concentration [133]. Due to the low temperatures necessary for the epitaxy of GaMnAs, the material quality is very sensitive to growth conditions such as substrate temperature and arsenic overpressure. Slight changes in the growth temperature may significantly affect magnetic properties of a DMS. In contrast to the extreme sensitivity of thicker GaMnAs films on growth temperature, our experiments indicate that the magnetic properties of thin GaMnAs layers are relatively insensitive to slight (i.e.,

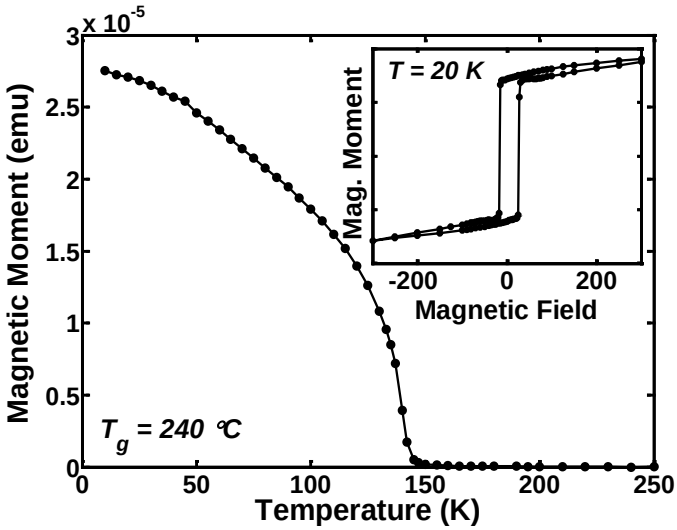

Fig. 7.7: Magnetic moment versus temperature for a 15 nm thick $Ga_{0.95}Mn_{0.05}As$ film measured using low-field (50 G) SQUID magnetometry. The inset shows the magnetic moment versus field for the same sample measured at 20 K. The applied field is parallel to the plane of the film.

5-10˚C) changes in substrate temperature during growth.

Magnetic properties of GaMnAs multilayers in which 15 nm $Ga_{0.95}Mn_{0.05}As$ layers were separated by 5 nm of intrinsic or heavily p-doped GaAs grown at a substrate temperature of 250˚C was also investigated. It is found that the maximum Curie temperature obtained from optimally annealed GaMnAs/i-GaAs multilayer heterostructures is nearly independent of the number of layers up to seven layers and is approximately equal to that of a single 15 nm GaMnAs epilayer. When the LT-GaAs spacer layers are heavily doped with Be, the Curie temperature in annealed structures is reduced from the case where no Be doping is used. The data from this study is summarized in Fig. 7.8. These structures offer thicker p^+-type contact layers, which may benefit certain device applications, without a significant degradation of the Curie temperature.

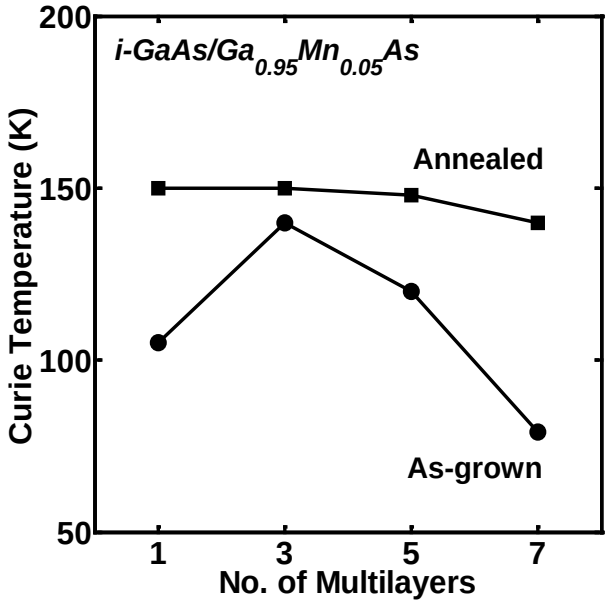

(a)

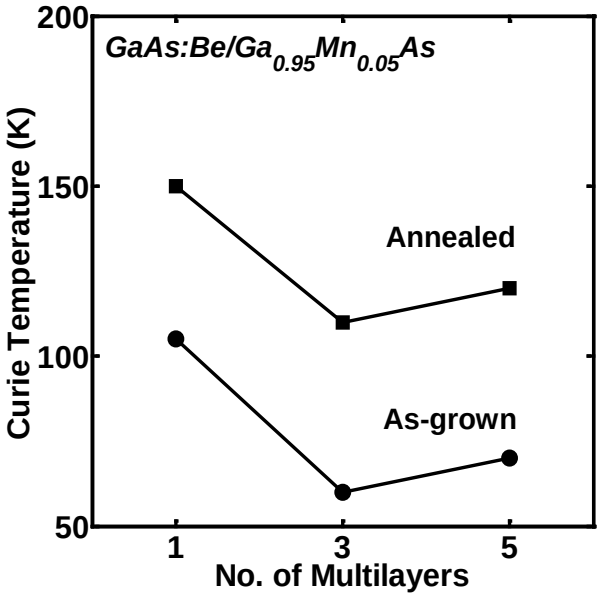

(b)

Fig. 7.8: Curie temperature of $Ga_{0.95}Mn_{0.05}As$/GaAs multilayers for as-grown and optimally annealed samples: (a) summarizes the data for an i-GaAs spacer layer placed between GaMnAs layers; (b) summarizes the data for p^+-GaAs spacer multilayer structures.

7.5 Epitaxial Growth and Magnetic Properties of InMnAs Quantum Dots

It was observed in Section 7.4 that T_c may not be raised above 150-160 K in thin (15 nm) (Ga,Mn)As epilayers and trilayer structures. Slightly higher T_c of 172 K has been reported in Mn δ-doped GaAs/p-AlGaAs triangular quantum wells after low-temperature annealing [135]. For electronic and optoelectronic spin injection devices, it is clearly desirable to achieve spin injection and device operation at room temperature, rendering GaMnAs unsuitable for such applications at the present time. It was theoretically predicted that *disorder* can increase Curie temperatures of DMS's [136]. An artificial way of creating disorder is to introduce randomness in self-organized diluted magnetic quantum dots (DMQDs) through inhomogeneous incorporation of Mn and interdot Mn compositional variation. It is in this context that magnetization properties of InMnAs QDs were studied.

As discussed in Section 2.2, self-organized InAs and InGaAs quantum dots are usually grown at substrate temperatures in the range of 480-520˚C. However, segregation of Mn and phase separation of MnAs in the InAs matrix necessitates the growth of InMnAs quantum dots at much lower substrate temperatures. Growth studies have shown that the formation of InAs quantum dots on (001)-GaAs is significantly inhibited at temperatures below 350˚C due to low In adatom surface migration [137]. The effects of altered growth conditions was investigated and found that with an As_4 pressure of 7×10^{-6} Torr and very low growth rates (<0.05ML/sec), single crystal self-organized quantum dots can be grown at substrate temperatures as low as 260˚C. A typical heterostructure is shown in Fig. 7.9(a). The Mn content was varied in the range of 10-20%. This nominal Mn content is estimated from the flux used during growth which is

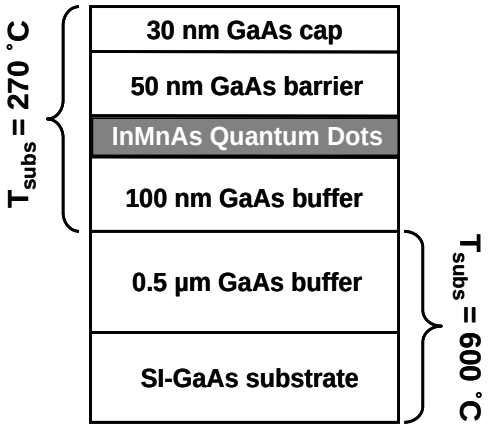

(a)

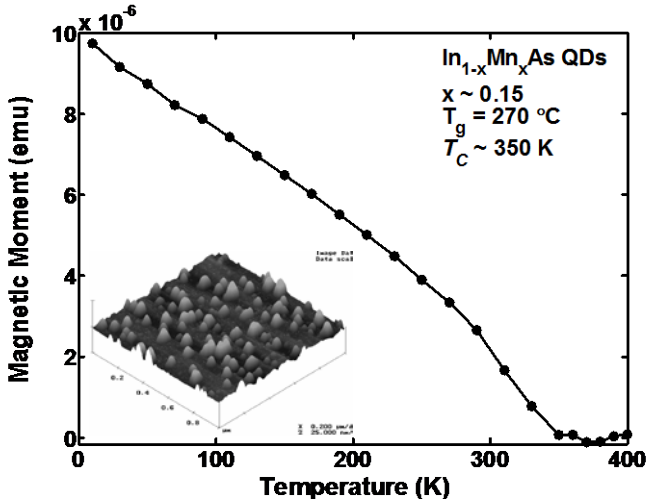

(b)

Fig. 7.9: (a) Heterostructure of DMQD sample measured by SQUID magnetometry; (b) magnetic moment versus temperature of 10-layer InMnAs QD sample measured by SQUID magnetometry. Inset shows the 1×1 μm^2 3-D AFM image of ~4 ML InMnAs QDs on an InAs wetting layer grown at 270˚C atop LT-GaAs.

calibrated by secondary ion mass spectroscopic (SIMS) analysis on InGaMnAs quantum wells. The inset in Fig. 7.9(b) shows a 3-D AFM image for ~4 monolayer InMnAs QDs deposited on LT-GaAs and indicates that the dots are well-formed even at low growth temperatures. The dot density is ~10^9 cm^{-2}. Transmission electron microscopy (TEM)

bright field imaging and diffraction analysis (see Fig. 7.10(a)) show that the InMnAs multilayer structure is fully pseudomorphic with respect to the GaAs substrate, but some dislocations, stacking faults, and point defects are generated during low-temperature epitaxy. No evidence of hexagonal, NiAs-type MnAs clusters was observed by TEM imaging nor was a second lattice structure detected by diffraction analysis. A high-resolution, cross-sectional TEM image of a single dot (see Fig. 7.10(b)) shows that InMnAs QDs grown by LT-MBE maintain a zincblende crystal structure and are near-pyramidal in shape, having a height and base width of 12 nm and 21 nm, respectively. X-ray energy dispersive spectroscopy (XEDS) analysis performed by Y. Lei at Argonne National Laboratory, Argonne, IL confirms the presence of Mn in each of the ten QD layers and finds the average Mn/In ratio over these layers to be 0.236. A representative magnetization curve is shown in Fig. 7.9(b) for a 10-layer InMnAs QD sample with T_c as high as 350 K. The reported Curie temperatures of MnAs and MnGa clusters in Ga(Mn)As are 318 K and above 400 K, respectively [137]. Thus, a Curie temperature of 350 K suggests a magnetic response that is either unique to InMnAs QDs or MnAs-rich MnGaAs clusters, though significant clustering is not indicated by our material characterization as discussed above.

The observed Curie temperatures in the InMnAs QD multilayer samples are significantly higher than those observed in either GaMnAs or InMnAs thin films grown by LT-MBE. While the previously discussed theoretical models neglecting the effect of disorder on magnetic properties and treating *p-d* exchange using a mean-field approximation provide a Curie temperature in reasonable agreement with experimental findings in the bulk materials, ferromagnetism in quantum dots is more complex as the

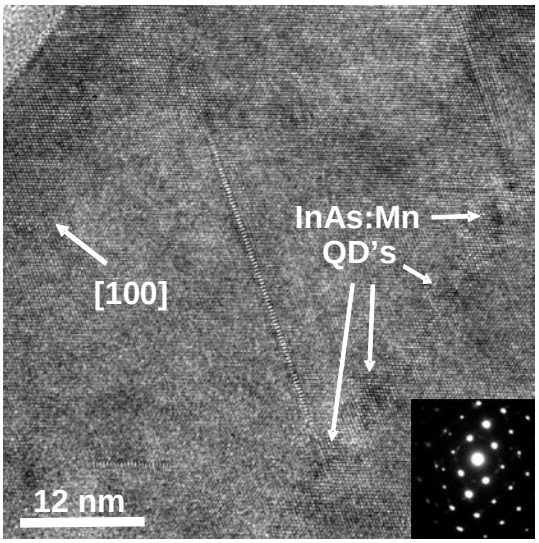

(a)

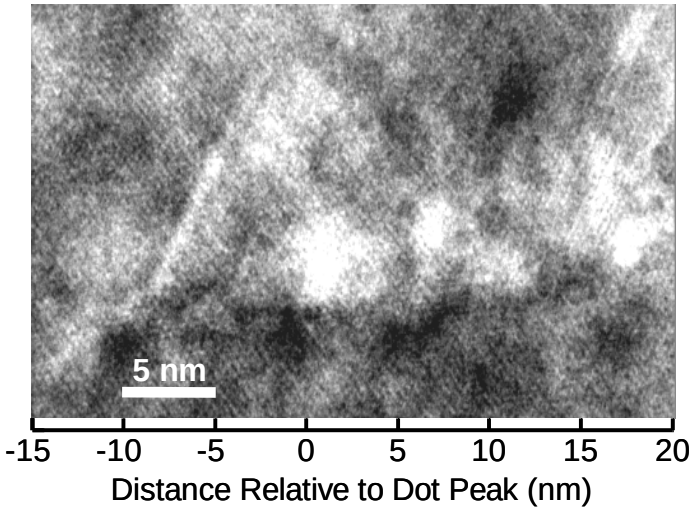

(b)

Fig. 7.10: (a) High-magnification TEM bright field image of an InMnAs quantum dot layer taken with <011> projection. A representative electron diffraction pattern of the GaAs matrix surrounding an InMnAs QD layer is shown in the inset; (b) high-resolution TEM image of a single InMnAs quantum dot (obtained in collaboration with Y. Lei at Argonne National Laboratory, Argonne, IL).

effects of epitaxial strain, quantum confinement, and disorder are expected to play a key role in determining their magnetic properties [136],[139]-[141]. It should be noted, in particular, that the degree of disorder in DMQDs is larger than in bulk due not only to substitutional disorder but also inhomogeneous Mn incorporation among neighboring DMQDs and irregularities in dot size and distribution unavoidably introduced during self-assembly. The effects of disorder on ferromagnetism have been theoretically studied by Berciu and Bhatt [136] and they predict an increase in T_c due to disorder. The multiple layers of the self-organized dots give rise to a matrix with a random distribution of the dots. If it can be assumed that the Mn incorporation within each dot is uniform and that disorder arises from fluctuation in the Mn content between individual dots, then a situation similar to the one analyzed by Berciu and Bhatt is obtained. Theoretical studies by Bouzerar *et al.* [139] accounting for a disordered carrier distribution within a non-perturbative RKKY treatment similarly predict higher Curie temperatures in DMS's than are suggested by standard RKKY calculations. Also, the presence of strong charge and spin disorder make carrier distribution and localization relevant issues in DMQDs. Hole localization by the trapping potential of Mn impurities can create a spin polarization of Mn atoms within the span of its wave function to form bound magnetic polarons [142], the interaction of which characterizes the ferromagnetic behavior of insulating, doped DMS's [143]. Carrier confinement within a QD is expected to strengthen hole localization and subsequently enhance the thermal stability of magnetic polarons, which may explain ferromagnetism in DMQDs at high temperatures.

Finally, it was found that the Curie temperature of the InMnAs DMQD samples may be further enhanced, when the dots are embedded in a GaMnAs matrix. The

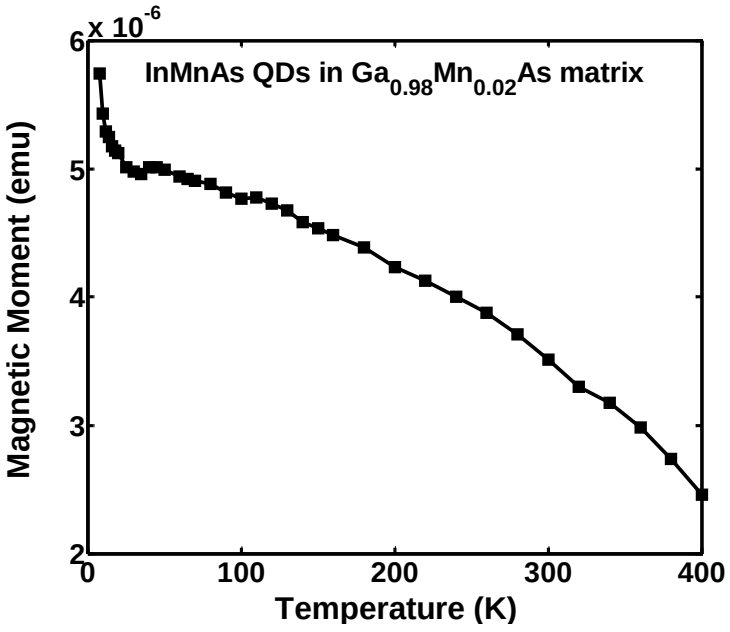

(a)

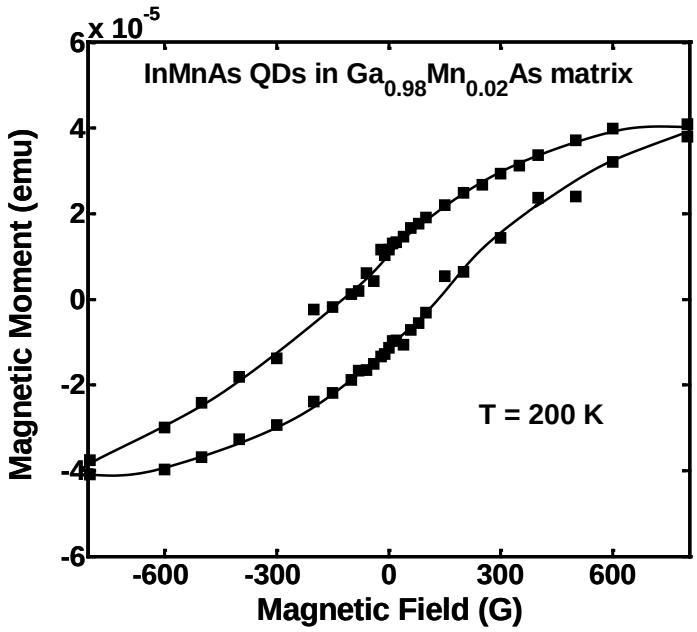

(b)

Fig. 7.11: (a) Magnetic moment versus temperature and (b) magnetic hysteresis measured at 200 K for a 10-layer InMnAs QD sample in GaMnAs matrix.

measured magnetic moment versus both temperature and applied field is shown in Fig. 7.11. The direction of the applied magnetic field is parallel to the plane of the sample. Unfortunately, SQUID setup constraints impeded conducting these experiments beyond 400 K. These InMnAs DMQDs may serve as high temperature spin injector layers in future spintronic devices, where a conductive (doped) matrix for the embedded DMQDs is required.

7.6 Summary

The magnetic properties of single and multiple layers of GaMnAs, grown by molecular beam epitaxy, have been investigated for application as spin injector layers in spin polarized lights sources. As-grown, thermally annealed and Be co-doped layers were studied. Curie temperatures as high as 150 K have been measured in 15nm $Ga_{0.95}Mn_{0.05}As$ films and similar results are obtained for multiple thin layers of GaMnAs separated by 5nm thick GaAs layers. The properties of self-organized InMnAs QDs buried in a GaAs or GaMnAs matrix were investigated. Magnetization measurements indicate T_c>300 K in the dot heterostructures.

CHAPTER VIII

SPIN-POLARIZED QUANTUM DOT LIGHT EMITTING DIODES WITH GaMnAs INJECTORS

8.1 Introduction

The electrical injection of spin-polarized carriers can be utilized for the realization of polarized light emitters [34],[144],[145]. Ideally in such devices, with the modulation of both spin orientation and density of carriers, the information carrying capacity can be enhanced as compared to a conventional light source. Together with polarization-sensitive detectors and optical interconnects, optical communication systems of increased bandwidth can be realized. In a typical spin-polarized light source, spin-polarized electrons or holes are injected from a spin injector (or spin-aligner) layer across a suitably spaced spacer layer and made to recombine with unpolarized carriers of the opposite type in the active (or recombination) region. The spin aligner layer is usually a diluted magnetic semiconductor (DMS) which exhibits ferromagnetic behavior below its Curie temperature, T_c. Therefore, spin injection does not require an external magnetic field.

The origin of ferromagnetism in GaMnAs DMS was discussed in Section 7.2. The intrinsic magnetic field causes the Zeeman splitting of the fourfold degenerate valence band energy levels, and the hole carriers are favored to be at the highest heavy-hole (HH) level, |3/2,-3/2>. Thus, *p*- type GaMnAs ferromagnetic layers can be used to inject holes

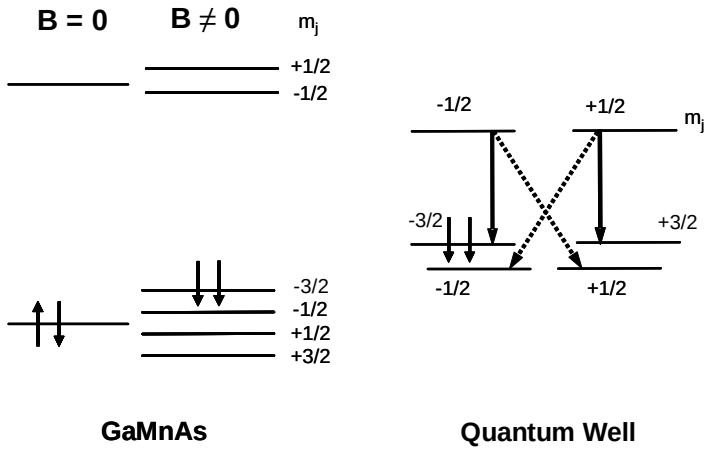

Fig. 8.1: Schematic of spin-alignment in GaMnAs by Zeeman splitting and selection rules of heavy- and light-hole recombination in an ideal quantum well.

with m_j=-3/2 orientation into the recombination regions of light emitting devices. The selection rules for optical transitions in quantum wells (QW) or quantum dots (QD) allow the interesting conversion of soin-polarized holes into circularly polarized emitted photons. According to the quantum selection rule of $\Delta m_j=\pm 1$, right-circularly polarized light is obtained from (-3/2→-1/2) and (-1/2→1/2) transitions of holes to the conduction band and, similarly, left-circularly polarized light arise from (3/2→1/2) or (1/2→-1/2) transitions. These are depicted in Fig. 8.1. Since HH and light hole (LH) transitions have different strengths, the optical polarization, P_{opt}, can be linked to the degree of spin-polarization, P_j. For instance, in an ideal GaAs/AlGaAs QW, where heavy hole transition is three times stronger than the light hole transitions, the maximum value of P_{opt} is $(1/2)P_j$. The situation is slightly different in real QWs because of the HH/LH band splitting and is further complicated in QDs because of the effect of biaxial strain and zero-dimensional effects in the energy levels as discussed in Section 2.2, but the same basic principles still apply.

Light emitting diodes (LEDs) with n-type II-VI DMS ZnMNSe and BeMnZnSe electron spin-aligners and GaAs-based active regions have been reported [34], [144]. Spin injection efficiencies of ~90% and optical polarization efficiencies of ~45% are measured at ~5 K in these devices. However, lattice-matched II-VI compounds on GaAs are difficult to realize by epitaxy and it is difficult to dope these materials [41]. The III-V DMS GaMnAs has also been used as a spin injector in LEDs [142]. Very low optical polarization (≤2%) at low temperatures (T<40 K) observed in these devices is primarily attributed to the large spin-orbit coupling in the valence band, leading to increased spin decoherence of holes.

In the present work, the materials parameters and heterostructure design have been carefully optimized to obtain record high output polarization, P_{opt}~30%, at T=80 K in spin-polarized LEDs. As in a previous study [146], self-organized InGaAs quantum dots have been utilized as the recombination medium for two reasons: first, pump-probe experiments have shown that the spin relaxation time in such QDs, ~50 ps, is larger than in quantum wells [147]; second, the interband ground state transition energy of the QDs is considerably smaller than the bandgap of GaMnAs for dilute alloys and therefore, despite the Zeeman splitting in this layer, field induced dichroism should be negligible.

8.2 Design, Epitaxial Growth and Fabrication of Spin Polarized LEDs

The heterostructure of the device grown by molecular beam epitaxy is shown in Fig. 8.2. 150 nm $Ga_{0.95}Mn_{0.05}As$ has been used as the spin-aligner and p-contact layer. As discussed in Section 7.3.4, the smaller thickness of GaMnAs provides a high Curie temperature, T_c,, but thick layers are required for fabrication of ohmic contacts. The

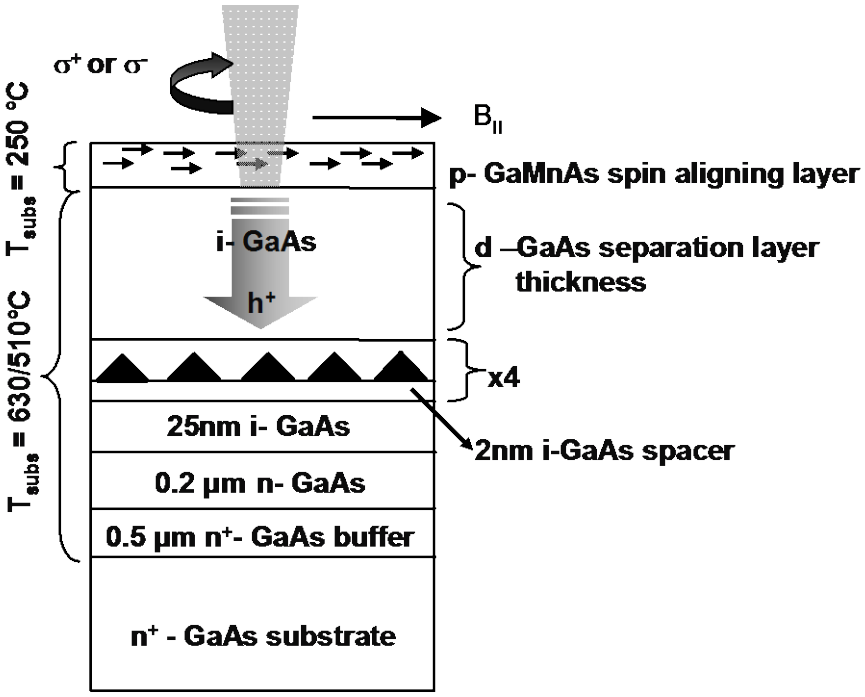

Fig. 8.2: Schematic of the grown and characterized spin-polarized light emitting diode.

LEDs were grown on semi-insulating GaAs (100) substrates. The n-GaAs layers were grown at 630°C, while the InGaAs QDs were grown at 500°C. After growing the *d*=45 nm GaAs spacer, the temperature was ramped down with a growth interruption. The details of the growth of GaMnAs layer were discussed in Section 7.3 and its magnetization data was presented in Fig. 7.4(a). An important design consideration is the thickness of the GaAs spacer, *d*, between the active quantum dot region and the spin-aligner. The spin dephasing time is very long for electrons and polarized carriers survive upto diffusion lengths of 100 µm [34]. The dephasing time is much smaller for holes, and so it is desirable to keep the spacer thickness as small as possible. On the other hand, if the Mn-doped injector layer is too close to the QD recombination region, the optical

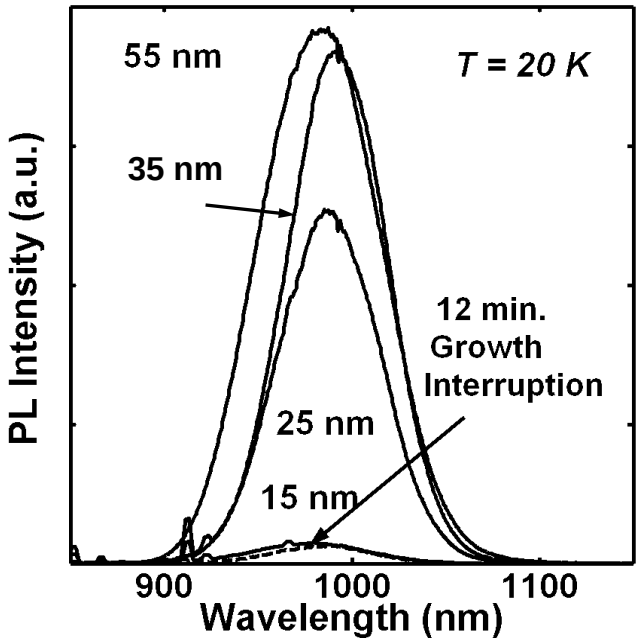

Fig. 8.3: The photoluminescence (PL) intensity versus wavelength on various spacer thicknesses between the quantum dot recombination region and GaMnAs aligner layer. The dashed curve is the PL of the sample with 12 minutes of growth interruption after deposition of 15 nm GaAs spacer.

property of the QDs is expected to degrade. We have therefore conducted photoluminescence (PL) measurements on samples with different values of *d*. The results are shown in Fig. 8.3. It is observed that the dots show very weak PL for $d \leq 15$ nm. The PL intensity increases with increasing spacer thickness *d* with constant excitation and tends to saturate for *d* larger than 35 nm. In order to determine whether the PL degradation for $d \leq 15$ nm is due to out-diffusion of Mn towards the QDs, or the incorporation of impurities due to growth interruption, measurements on a sample in which growth was interrupted for 12 minutes after deposition of 15 nm of GaAs spacer was conducted. The substrate temperature was lowered to 250°C and another 30 nm of GaAs was grown, followed by growth of the 150 nm GaMnAs layer at the same

temperature. The weak luminescence from this sample, also shown in Fig. 8.3, indicates that the PL degradation is related to incorporation of impurities during the growth interruption. d~45 nm was chosen, as an optimal value for maximum PL intensity and minimum spin dephasing. Mesa-shaped diodes with 400-600 μm diameters and ring ohmic contacts were fabricated by standard optical lithography, wet etching and metallization techniques.

8.3 Device Characteristics

The electroluminescence (EL) of the LEDs was measured in an Oxford Instruments magneto-cryostat at temperatures below the measured T_c of the GaMnAs aligner layer. The direction of the magnetic field was in plane, i.e., the easy axis of magnetization of GaMnAs. The EL peak was at 1.19 eV at 54 K with a full width at half-maximum (FWHM) linewidth of 65 meV. The spectral position of the EL peak is in agreement with the measured PL of the QDs. The LEDs were forward DC biased at 80 mA. The output light was passed through a zero-order quarter-wave plate, which converts circularly polarized light into linearly polarized light. A Glan-Thompson calcite linear polarizer was used to analyze the degree of the horizontal and vertical linearly polarized light. The analyzed light is focused onto a Miniature Fiber Optics spectrometer. The background spectrum of the ambience and electronic noise of the spectrometer were measured and subsequently subtracted from the measured signals. Near zero polarization was observed before magnetizing the device at 54 K. The measured EL spectra at 4.5 K are shown in Fig. 8.4(a). The peak optical polarization was calculated from:

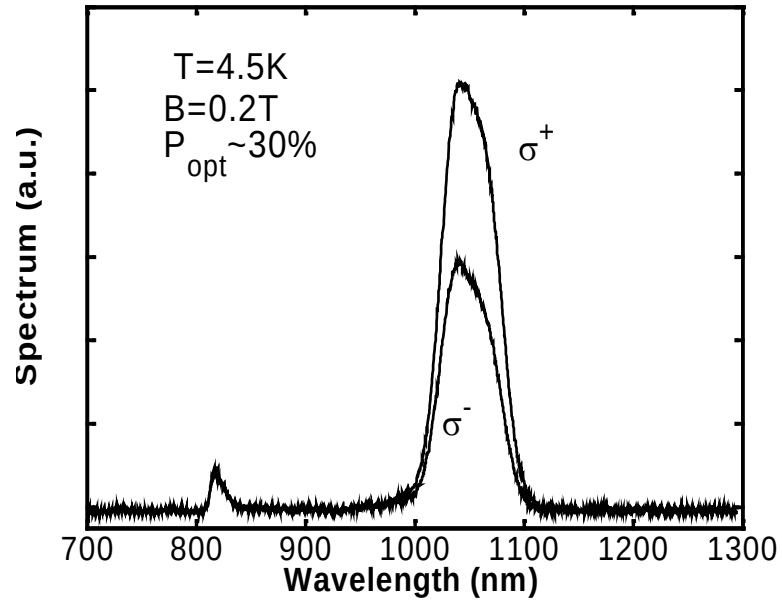

(a)

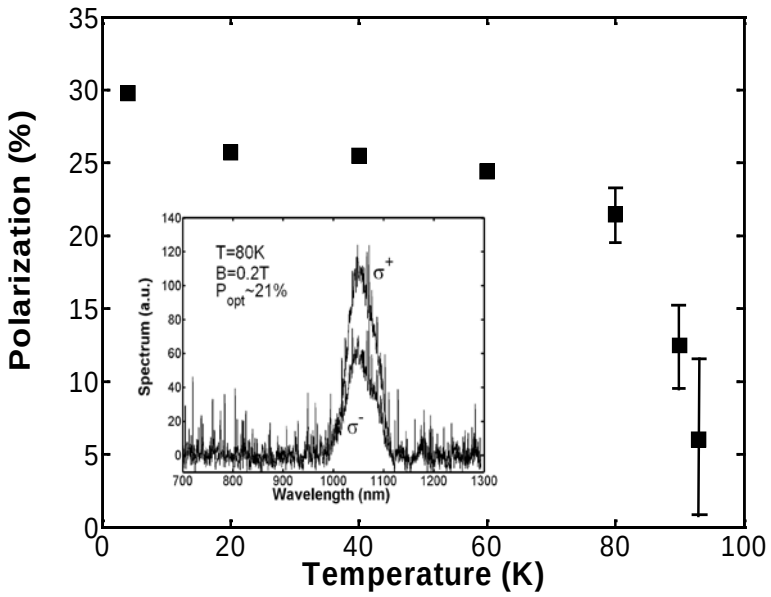

(b)

Fig. 8.4: (a) The analyzed left- and right-circularly polarized output light of spin-LEDs at 4.5 K; (b) peak polarization versus temperature. The inset shows the polarized spectrum at 80 K.

$$P_{opt} = \frac{\sigma^+ - \sigma^-}{\sigma^+ + \sigma^-} \qquad (8.1)$$

The data show clear discrimination between right- and left-circular components of the light with a peak optical polarization of ~30%, while no polarization is observed at the smaller GaAs peak at about 820 nm. Magnetic field- and temperature-dependent measurement of the polarized output spectra were conducted on the magnetized devices.

As shown in Fig. 8.4(b), the devices show P_{opt} of about 21% at temperatures as high as 80 K, which is the highest reported operating temperature of spin-polarized light sources to date [34],[144]-[146]. The improvements in the device performance, compared to previous reports, are attributed to the aforementioned careful choice of the thickness of the GaAs spacer by proximity can be PL studies, as well as the optimized growth condition and thickness of the GaMnAs layer with a high T_c~100 K.

8.4 Summary

Light-emitting diode heterostructures with 150 nm $Ga_{0.95}Mn_{0.05}As$ spin injector layers and $In_{0.4}Ga_{0.6}As$ quantum dot active regions were grown and fabricated into 600 μm diameter mesa-shaped surface-emitting devices. Polarized light at 1.05 μm is observed with an output polarization efficiency of 30% and record high temperature operation.

APPENDIX

FABRICATION STEPS FOR GAAS-BASED SINGLE-MODE RIDGE WAVEGUIDE LASERS

I. Post-Growth Preparation

a) Indium removal: $HgCl_2$/dimethlyformamide solution with ultrasound.

b) Lapping: indium residue removal and backside planarization

II. P-Contact Metallization

a) Oxide removal: BHF, 30 sec.

b) Lithography

1) Solvent clean: acetone, IPA 3 min. each

2) Dehydration bake: 2 min. at 130°C

3) Photo-resist spin: HMDS, AZ5214E at 4.5 krpm

4) Pre-bake: 1 min at 105°C

5) Edge bead removal

- Exposure: 40 sec. at 20 mW/cm^2
- Photo-resist development: AZ 327 for 50 sec.

6) Exposure: 4.5 sec. at 20 mW/cm^2

7) Post-bake: 1 min. at 130°C

8) Image reversal: 90 sec. at 20 mW/cm^2

9) Photo-resist development: AZ327 for 50 sec.

10) De-scum: 1 min. at 80 W

c) Oxide removal: BHF, 30 sec.

d) Deposition: Pd/Zn/Pd/Au=100/200/200/3000 Å

e) Lift-off: warm acetone, IPA

f) Dektak: measure deposited metal thickness

III. Self-Aligned Etching to Form the Ridge

a) Reactive ion etching: BCl_3/Ar=11/21 sccm, 10 mT, 50 W (rate ~12 nm/min.)

b) Wet etching: $H_3PO_4/H_2O_2/H_20$=1/1/20 (rate ~ 5 nm/sec)

c) Dektak: Stop combination of mostly dry and partially wet etching at 200 nm above the active region.

IV. Mesa Formation

a) Lithography

1) Solvent clean: acetone, IPA 3 min. each

2) Dehydration bake: 2 min. at 130°C

3) Photo-resist spin: HMDS, SC1827 at 4.0 krpm

4) Pre-bake: 1 min at 105°C

5) Exposure: 12.5 sec. at 20 mW/cm^2

6) Photo-resist development: AZ351:H_2O=1:5 for 45 sec.

7) De-scum: 1 min. at 80 W

b) Etching the Mesa

1) Reactive ion etching: BCl_3/Ar=11/21 sccm, 10 mT, 50 W (rate ~12 nm/min.)

2) Wet etching: $H_3PO_4/H_2O_2/H_20$=1/1/20 (rate ~ 5 nm/sec)

3) Dektak and electrical probing: Stop combination of mostly dry and partially wet etching to reach the n-contact layer

c) Resist strip: hot PRS1000 for 30 min., DI water rinse for 10 min., acetone, IPA

V. N-Contact Metallization

a) Lithography: similar to step IV-a.

b) Oxide removal: BHF, 30 sec.

c) Deposition: Ni/Ge/Au/Ti/Au=250/325/650/200/3000 Å

d) Lift-off: warm acetone, IPA

VI. Contact Annealing

a) 250/400/250°C for 30/60/30 sec.

VII. Planarization and Passivation

a) 1μm-thick SiO_2 deposition by plasma enhanced chemical vapor deposition (PECVD): SiH_4/N_2O=24/20 sccm, 100 mT, 200°C, 80 W, 70 min.

VIII. Via Hole

a) Lithography

1) Solvent clean: acetone, IPA 3 min. each

2) Dehydration bake: 2 min. at 130°C

3) Photo-resist spin: HMDS, NR8-3000 at 4.0 krpm

4) Pre-bake: 1 min at 105°C

5) Exposure: 14 sec. at 20 mW/cm^2

6) Photo-resist development: RD-2, 3.5-4.0 min.

7) De-scum: 1 min. at 80 W

b) Reactive ion etching: CH_4/CHF_3=25/25 sccm, 40 mT, 180 W (rate ~45-50 nm/min.)

c) Strip photo-resist: hot RR2-2, 20 min., IPA

d) De-scum: 3 min at 150 W

IX. Interconnect Metallization

a) Lithography: similar to step IV-a, except pre-bake at 90°C at step IV-a-4.

b) Deposition Ti/Al/Ti/Au=500/10000/500/4000 Å

X. Cleaving

a) Create 1500 μm-long, 180 μm-deep scribe marks with desired cavity lengths spacing

b) Lap down sample to ~100 μm

c) Cleave by mounting the sample on a metal strip with black wax and bending the strip

BIBLIOGRAPHY

[1] R. N. Hall, G. E. Fenner, J. D. Kingsley, T. J. Soltys and R. O. Carlson, "Coherent light emission from GaAs junctions," *Physical Review Letters*, vol. 9, pp. 366-368, 1962.

[2] M. I. Nathan, W. P. Dupke, G. Burns, F. H. Dill, Jr. and G. Lasher, "Stimulated emission of radiation from GaAs p-n junctions," *Applied Physics Letters*, vol. 1, pp. 62-64, 1962.

[3] N. Holonyak Jr. and S. F. Bevacqua, "Coherent (visible) light emission from $Ga(As_{1-x}P_x)$ junctions," *Applied Physics Letters*, vol. 1, pp. 82-83, 1962.

[4] T. M. Quist, R. H. Rediker, R. J. Keyes, W. E. Krag, B. Lax, A. L. McWhorter and H. J. Zeiger, "Semiconductor maser of GaAs," *Applied Physics Letters*, vol. 1, pp. 91-93, 1962.

[5] R. D. Dupuis, "An introduction to the development of the semiconductor laser," *IEEE Journal of Quantum Electronics*, vol. 23, pp. 651-657, 1987.

[6] Z. I. Alferov and R. F. Kazarinov, "Semiconductor laser with electric pumping," Inventor's Certificate 181737 [in Russian], Appli. 950840, priority as of March 30, 1963.

[7] H. Kroemer, "A proposed class of heterojunction injection lasers," *Proceedings of IEEE*, vol. 51, p. 1782, 1963.

[8] H. Hayashi, M. B. Panish, P. W. Foy and S. Sumski, "Junction lasers that operate continuously at room temperature," *Applied Physics Letters*, vol. 17, pp. 109-111, 1970.

[9] Z. I. Alferov, V. M. Andreev, D. Z. Garbuzov, Y. Z. Zhilyaev, E. P. Morozov, E. L. Portnoi and V. G. Trogim, "Investigation if the influence of the AlAs-GaAs heterostructure parameters on the laser threshold current and the realization of continuous emission at the room temperature," *Fiz. Tekh. Poluprovodn*, vol. 4, pp. 1826-1829, 1970 [*Sov. Phys. Semiconduc.*, vol. 4, pp. 1573-1575, 1971].

[10] J. P. van der Ziel, R. Dingle, R. C. Miller, W. Wiegmann and W. A. Nordland Jr., "Laser oscillations from quantum states in very thin GaAs- $Al_{0.2}Ga_{0.8}As$ multilayer structures," *Applied Physics Letters*, vol. 26, pp. 463-465, 1975.

[11] R. D. Dupuis, P. D. Dapkus, N. Holonyak Jr., E. A. Rezek and R. Chin, "Room temperature operation of quantum-well $Ga_{1-x}Al_xAs$-GaAs laser diodes grown by metalorganic chemical vapor deposition," *Applied Physics Letters*, vol. 32, pp. 295-297, 1978.

[12] H. M. Manasevit, "Single crystal GaAs on insolating substrates," *Applied Physics Letters*, vol. 12, pp. 156-159, 1968.

[13] A. Y. Cho, "Film deposition by molecular beam technique," *Journal of Vacuum Science Technology*, vol. 8, pp. S31-S38, 1971.

[14] Y. Arakawa and H. Sakaki, "Multidimensional quantum well laser and temperature dependence of its threshold current," *Applied Physics Letters*, vol. 40, pp. 939-941, 1982.

[15] H. Hirayama, K. Matsunaga, M. Asada, and Y. Suematsu, "Lasing action of $Ga_{0.67}In_{0.33}As$/GaInAsP/InP tensile-strained quantum box lasers," *Electronic Letters*, vol. 30, pp. 142-143, 1994.

[16] K. W. Brryman, S. A. Lyon, and M. Segev, "Mid-infra-red photoconductivity in InAs quantum dots," *Applied Physics Letters*, vol. 70, pp. 1861-1863, 1997.

[17] J. Phillips, K. Kamath, and P. Bhattacharya, "Far-infrared photoconductivity in self-organized InAs quantum dots," *Applied Physics Letters*, vol. 72, pp. 2020-2022, 1998.

[18] D. Pan, E. Towe, and S. Kennerly, "Normal incidence Intersubband (In,Ga)As/GaAs quantum dot infrared photodetectors," *Applied Physics Letters*, vol. 73, pp. 1937-1939, 1998.

[19] J. Phillips, K. Kamath, T. Brock, and P. Bhattacharya, "Characteristics of InAs/AlGaAs self-organized quantum dot modulation doped field effect transistors," *Applied Physics Letters*, vol. 72, pp. 3509-3511, 1998.

[20] O. Qasaimeh, K. Kamath, J. Phillips, and P. Bhattacharya, "Linear and quadratic electro-optic coefficients of self-organized $In_{0.4}Ga_{0.6}As$/GaAs quantum dots," *Applied Physics Letters*, vol. 72, pp. 1275-1277, 1998.

[21] N. Kirsteadter, N. N. Ledentsov, M. Grundmann, D. Bimberg, V. M. Ustinov, S. S. Ruvimov, M. V. Maximov, P. S. Kop'ev, and Z. I. Alferov, "Low threshold, large T_0 injection laser emission from (InGa)As quantum dots," *Electronic Letters*, vol. 30, pp. 1416-1417, 1994.

[22] Z. I. Alferov, N. Y. Gordeev, S. V. Zaistev, P. S. Kop'ev, I. V. Kochnev, V. V. Khomin, I. L. Krestinov, N. N. Ledentsov, A. V. Lunev, M. V. Maksimov, S. S. Ruminoc, A. V. Sakharov, A. F. Tsatsul'nikov, Y. M. Shernyskov, and D. Bimberg,

"A low-threshold injection heterojunciton laser based on quantum dots, produced by gas-phase epitaxy from organometallic compounds," *Semiconductors*, vol. 30, pp. 197-200, 1996.

[23] K. Kamath, P. Bhattacharya, T. Sonowski, T. Norris, J. Phillips, "Room-temperature operation of $In_{0.4}Ga_{0.6}As$/GaAs self-organised quantum dot lasers," *Electronics Letters*, vol. 32, pp. 1374-1375, 1996.

[24] K. Kamath, J. Phillips, H. Jiang, J. Singh, and P. Bhattacharya, "Small-signal modulation and differential gain of single-mode self-organized $In_{0.40}Ga_{0.60}As$/GaAs quantum dot lasers," *Applied Physics Letters*, vol. 70, pp. 2952-2953, 1997.

[25] D. Klotzkin, K. Kamath, K. Vineberg, P. Bhattacharya, R. Murty, and J. Laskar, "Enhanced modulation bandwidth (20 GHz) of $In_{0.4}Ga_{0.6}As$/GaAs self-organized quantum dot lasers at cryogenic temperatures: role of carrier relaxation and differential gain," *IEEE Photonics Technology Letters*, vol. 10, pp. 932-934, 1998.

[26] P. G. Eliseev, H. Li, T. Liu, T. C. Newell, L. F. Lester, and K. J. Malloy, "Ground-state emission and gain in ultralow-threshold InAs-InGaAs quantum-dot lasers," *IEEE Journal of Selected Topics on Quantum Electronics*, vol. 7, pp. 135-142, 2001.

[27] N. Kirstaedter, O. Schmidt, N. Ledenstov, D. Bimberg, V. Ustinov, A. Egorov, A. Zhukov, M. Maximov, P. Kop'ev, and Z. I. Alferov, "Gain and differential gain of single layer InGaAs/GaAs quantum dot injection lasers," *Applied Physics Letters*, vol. 69, pp. 1226-1228, 1996.

[28] T. C. Newell, D. J. Bossert, A. Stintz, B. Fuchs, K. J. Malloy, and L .F. Lester, "Gain and linewidth enhancement factor in InAs quantum-dot laser diodes," *IEEE Photonics Technology Letters*, vol. 11, pp. 1527-1529, 1999.

[29] H. Saito, N. Nishi, and S. Sugou, "Low chirp operation in 1.6 μm quantum dot laser under 2.5 GHz direct modulation," *Electronic Letters*, vol. 37, pp.1293-1295, 2001.

[30] C. Ribbat, R. L. Sellin, I. Kaiander, F. Hopfer, N. N. Ledentsov, D. Bimberg, A. R. Kovsh, V. M. Ustinov, A. E. Zhukov, and V. Maximov, "Complete suppression of filamentation and superior beam quality in quantum-dot lasers," *Applied Physics Letters*, vol. 82, pp. 952-954, 2003.

[31] H. A. Akinaga, H. Ohno, "Semiconductor Spintronics," *IEEE Transactions on Nanotechnology*, vol. 1, pp. 19-31, 2002.

[32] G. A. Prinz, "Magnetoelectronics," *Science*, vol. 282, pp. 1660-1663, 1998.

[33] S. Datta, and B. Das, "Electronic analog of the electro-optic modulator," *Applied Physics Letters*, vol. 56, pp. 665-667, 1990.

[34] R. Fiedeling, M. Keim, G. Reuscher, W. Ossau, G. Schmidt, A. Waag, and L. W. Molenkamp, "Injection and detection of a spin-polarized current in a light-emitting diode," *Nature*, vol. 402, pp. 787-790, 1999.

[35] M. Oestreich, M. Bender, J. Hübner, D. Hägele, W. W. Rühle, T. Hartmann, P. J. Klar, W. Heimbrodt, M. Lampalzer, "Spin injection, spin transport and spin coherence," *Semiconductor Science and Technology*, vol. 17, pp. 285-297, 2002.

[36] A. Imamoglu, D. D. Awschalom, G. Burkard, D. P. DiVincenzo, D. Loss, M. Sherwin, and A. Small, "Quantum information processing using quantum dot spins and cavity QED," *Physical Review Letters*, vol. 83, pp. 4204-4207, 1999.

[37] D. Hägele, M. Oestreich, W. W. Rühle, N. Nestle, K. Eberl, "Spin transport in GaAs," *Applied Physics Letters*, vol. 73, pp. 1580-1582, 1998.

[38] B. T. Jonker, "Progress toward electrical injection of spin-polarized electrons into semiconductors," *Proceedings of IEEE*, vol. 91, pp. 727-740, 2003.

[39] S. von Molnár, and D. Read, "New materials for semiconductor spin-electronics," *Proceedings of IEEE*, vol. 91, pp. 715-726, 2003.

[40] P. R. Hammar, B. R. Bennet, M. J. Yang, and M. Johnson, "Observation of Spin Injection at a Ferromagnet-Semiconductor Interface," *Physical Review Letters*, vol. 83, pp. 203-206, 1999.

[41] H. Ohno, "Making nonmagnetic semiconductors ferromagnetic," *Science*, vol. 281, pp. 951-956, 1998.

[42] D. R. Matthews, H. D. Summers, P. M. Smowton, and M. Hopkinson, "Experimental investigation of the effect of wetting-layer states on the gain-current characteristics of quantum-dot lasers," *Applied Physics Letters*, vol. 81, pp. 4904-4906, 2002.

[43] L. Asryan, and S. Luryi, "Tunnel-injection quantum-dot laser: ultra-high temperature stability", *IEEE Journal of Quantum Electronics*, vol. 37, pp. 905-910, 2001.

[44] P. Bhattacharya, and S. Ghosh, "Tunnel injection $In_{0.4}Ga_{0.6}As$/GaAs quantum dot lasers with 15 GHz modulation bandwidth at room temperature," *Applied Physics Letters*, vol. 80, pp.3482-3484, 2002.

[45] Y. Miyamoto, Y. Miyake, M. Asada, and Y. Suematsu, "Threshold current density of GaInAsP/InP quantum box lasers," *IEEE Journal of Quantum Electronics*, vol. 25, pp. 2001-2006, 1989.

[46] O. B. Shchekin, and D. G. Deppe, "Low-threshold high-T_0 1.3-μm InAs quantum-dot lasers due to p-type modulation doping of the active region," *IEEE Photonics Technology Letters*, vol. 14, pp. 1231-1233, 2002.

[47] S. W. Corzine, R.-H. Yan, and L. A. Coldren, "Optical gain in III-V bulk and quantum well semiconductors," in *Quantum Well Lasers*, P. S. Zory, Ed. San Diego, CA: Academic Press, 1993, pp. 17-96.

[48] L. V. Asryan, and R. A. Suris, "Inhomogenous line broadening and the threshold current density of a semiconductor quantum dot laser," *Semiconductor Science and Technology*, vol. 11, pp. 554-567, 1996.

[49] H. Jiang, and J. Singh, "Nonequilibrium distribution on quantum dot lasers and influence on laser spectral output," *Journal of Applied Physics*, vol. 10, pp. 7438-7442, 1999.

[50] M. Grundmann, and D. Bimberg, "Gain and threshold of quantum dot lasers: theory and comparison to experiments," *Japanese Journal of Applied Physics*, vol. 36, pp. 4181-4187, 1997.

[51] H. Jiang, and J. Singh, "Self-assembled semiconductor structures: electronic and optoelectronic properties," *IEEE Journal of Quantum Electronics*, vol. 34, pp. 1188-1196, 1998.

[52] O. Stier, M. Grundmann, and D. Bimberg, "Electronic and optical properties of strained quantum dots modeled by 8-band k.p theory," *Physical Review B*, vol. 59, pp. 5688-5701, 1999.

[53] P. Bhattacharya, K. K. Kamath, J. Singh, D. Klotzkin, J. Phillips, H. Jiang, N. Chervela, T. B. Norris, T. Sonsowski, J. Laskar, and M. R. Murty, "In(Ga)As/GaAs self-organized quantum dot lasers: DC and small-signal modulation properties," *IEEE Transactions on Electron Devices*, vol. 46, pp. 871-883, 1999.

[54] P. M. Petroff, A. C. Gossard, W. Wiegmann, "Structure of AlAs-GaAs interfaces grown on (100) vicinal surfaces by molecular beam epitaxy," *Applied Physics Letters*, vol. 45, pp. 620-622, 1984.

[55] T. Fukui, and H. Saito, "$(AlAs)_{0.5}(GaAs)_{0.5}$ fractional-layer superlattices grown on (001) vicinal surfaces by metalorganic chemical vapor deposition," *Applied Physics Letters*, vol. 50, pp. 824-826, 1987.

[56] E. Kapon, K. Kash, E. M. Olausen, D. M. Hwang, and E. Calos, "Luminescence characteristics of quantum wires grown by organometallic chemical vapor deposition on nonplanar substrates," *Applied Physics Letters*, vol. 60, pp. 477-479, 1992.

[57] L. N. Pfeiffer, H. I. Stormer, K. W. Baldwin, K. W. West, A. R. Goni, A. Pinzuk, R. C. Ashoori, M. M. Dignam, and W. Wegscheider, "Cleaved edge overgrowth for quantum wire fabrication," *Journal of Crystal Growth*, vol. 127, pp. 849-857, 1993.

[58] W. J. Schaffer, M. D. Lind, S. P. Kowalczyk, and R. W. Grant, "Nucleation and strain relaxation at the InAs/GaAs(100) heterojunction," *Journal of Vacuum Science and Technology B*, vol. 1, pp. 688-695, 1983.

[59] B. F. Lewis, T. C. Lee, F. J. Grunthaner, A. Madhukar, R. Fernandez, and F. F. Madanian, "RHEED oscillation studies of MBE growth kinetics and lattice mismatch strain-induced effects during InGaAs growth on GaAs(100)," *Journal of Vacuum Science and Technology B*, vol. 2, pp. 419-424, 1983.

[60] F. Houzay, C. Guille, J. M. Moisson, P. Henoc, and F. Barth, "First stages of the MBE growth of InAs on (001)GaAs," *Journal of Crystal Growth*, vol. 81, pp. 67-72, 1987.

[61] D. Leonard, M. Krishnamurthy, C. M. Reaves, S. P. Denbaars, and P. M. Petroff, "Direct formation of quantum-sized dots from uniform coherent islands of InGaAs on GaAs surfaces," *Applied Physics Letters*, vol. 63, pp. 3203-3205, 1993.

[62] K. Mukai, N. Ohtsuka, M. Sugawara, and S. Yamazaki, "Self-Formed $In_{0.5}Ga_{0.5}As$ Quantum Dots on GaAs Substrates Emitting at 1.3 μm," *Japanese Journal of Applied Physics*, vol. 33, pp. L1710-L1712, 1994.

[63] M. Volmer, and A. Weber, *Z. Phys. Chem*., vol. 119, p. 277, 1926.

[64] I. N. Stranski, and L. Krasranow, "Sitzungsberichte d. Akad. D. Wissenschaften in Wien," *Abt. IIb.*, Band, vol. 146, p. 146, 1937.

[65] F. C. Frank, and J. H. van der Merwe, *Proceedings of Royal Society of London A*, vol. 198, p. 205, 1949.

[66] I. Vurgaftman, Y. Lam, and J. Singh, "Carrier thermalization in sub-three-dimensional electronic systems: Fundamental limits on modulation bandwidth in semiconductor lasers," *Physical Review B*, vol. 50, pp. 14309-14326, 1994.

[67] J. Urayama, T. B. Norris, J. Singh, and P. Bhattacharya, "Observation of phonon bottleneck in quantum dot electronic relaxation," *Physical Review Letters*, vol. 86, pp. 4930-4932, 2001.

[68] K. Kim, J. Urayama, T. B. Norris, J. Singh, J. Phillips, and P. Bhattacharya, "Gain dynamocs and uktrafast spectral hole burning in In(Ga)As self-organized quantum dots," *Applied Physics Letters*, vol. 81, pp. 670-672, 2002.

[69] J. Urayama, T. B. Norris, H. Jiang, J. Singh, and P. Bhattacharya, "Temperature-dependent carrier dynamics in self-assembled InGaAs quantum dots," *Applied Physics Letters*, vol. 80, pp. 2162-2164, 2002.

[70] D. G. Deppe, and D. L. Huffaker, "Quantum dimensionality, entropy, and the modulation response of quantum dot lasers," *Applied Physics Letters*, vol. 77, pp. 3325-3327, 2000.

[71] P. Bhattacharya, J. Singh, H. Yoon, X. Zhang, A. Gutierrez-Aitken, and L. Yam, "Tunneling injection lasers: a new class of lasers with reduced hot carrier effects," *IEEE Journal of Quantum Electronics*, vol. 32, pp. 1620-1629, 1996.

[72] X. Zhang, A. Gutierrez-Aitken, D. Klotzkin, P. Bhattachrya, C. Caneau, and R. Bhat , "0.98-μm multiple-quantum-well tunneling injection laser with 98-GHz intrinsic modulation bandwidth," *IEEE Journal of Selected Topics on Quantum Electronics*, vol. 3, pp. 309-314, 1997.

[73] H. Yoon, A. Gutierrez-Aitken, R. Jambunathan, J. Singh, and Bhattacharya, "A "cold" InP-based tunneling injection laser with greatly reduced Auger recombination and temperature dependence," *IEEE Photonics Technology Letters*, vol. 7, pp. 974-976, 1995.

[74] P. Bhattacharya, S. Ghosh, S. Pradhan, J. Singh, Z-K. Wu, J. Urayama, K. Kim, and T. Norris, "Carrier dynamics and high-speed modulation properties of tunnel injection InGaAs/GaAs quantum dot lasers," *IEEE Journal of Quantum Electronics*, vol. 39, pp. 952-962, 2003.

[75] S. Ghosh, S. Pradhan, and P. Bhattacharya, "Dynamic characteristics of high-speed $In_{0.4}Ga_{0.6}As$/GaAs self-organized quantum dot lasers at room temperature," *Applied Physics Letters*, vol. 81, pp. 3055-3057, 2002.

[76] S. Fathpour, P. Bhattacharya, S. Pradhan, S. Ghosh, "Linewidth enhancement factor and near-field pattern in tunnel injection $In_{0.4}Ga_{0.6}As$ self-assembled quantum dot lasers," *Electronics Letters*, vol. 39, pp. 1443-1445, 2003.

[77] S. Fathpour, Z. Mi, S. Chakrabarti, P. Bhattacharya, A. R. Kovsh, S. S. Mikhrin, I. L. Krestnikov, A. V. Kozhukhov, and N. N. Ledentsov, "Characteristics of high-performance 1.0 μm and 1.3 μm quantum dot lasers: impact of p-doping and tunnel injection," in *62nd Device Research Conference Digest*, Notre Dame, IN, June 2004, pp. 156-157.

[78] S. Fathpour, Z. Mi, and P. Bhattacharya, "High-speed quantum dot lasers," *Journal of Physics D*: *Applied Physics*, to appear in the May 2005 issue.

[79] K. J. Vahala, and C. E. Zah, "Effect of doping on the optical gain and the spontaneous noise enhancement factor in quantum well amplifiers and lasers studied

by simple analytical expressions," *Applied Physics Letters*, vol. 52, pp. 1945-1947, 1998.

[80] K. Uomi, "Modulation-doped multi-quantum well (MD-MQW) lasers. I. theory," *Japanese Journal of Applied Physics*, vol. 29, pp. 81-87, 1990.

[81] O. B. Shchekin, and D. G. Deppe, "The role of p-type doping and the density of states on the modulation response of quantum dot lasers," *Applied Physics Letters*, vol. 80, pp. 2758-2760, 2002.

[82] D. G. Deppe, H. Huang, and O. B. Shchekin, "Modulation characteristics of quantum-dot lasers: the influence of p-type doping and electronic density of states on obtaining high speed," *IEEE Journal of Quantum Electronics*, vol. 38, pp. 1587-1593, 2002.

[83] A. A. Dikshit, and J. M. Pikal, "Carrier distribution, gain, and lasing in 1.3-μm InAs-InGaAs quantum-dot lasers," *IEEE Journal of Quantum Electronics*, vol. 40, pp. 105-112, 2004.

[84] M. Gioannini, "Investigation of p-type doping effect on the gain characteristics of quantum dash semiconductor lasers," *Proceeding of SPIE International Society of Optical Engineering*, vol. 5452, pp. 526-533, 2004.

[85] S. Fathpour, Z. Mi, P. Bhattacharya, A. R. Kovsh, S. S. Mikhrin, I. L. Krestnikov, A. V. Kozhukhov, and N. N. Ledentsov, "The role of Auger recombination in the temperature-dependent output characteristics of p-doped 1.3 μm quantum dot lasers," *Applied Physics Letters*, vol. 85, pp. 5164-5166, 2004.

[86] D. Bhattacharyya, E. A. Avrutin, A. C. Bryce, J. H. Marsh, D. Bimberg, F. Heinrichsdorff, V. M. Ustinov, S. V. Zaitsev, N. N. Ledentsov, P. S. Kop'ev, Zh. I. Alferov, A. I. Onischenko, and E. P. O'Reilly, "Spectral and dynamic properties of InAs-GaAs self-organized quantum-dot lasers," *IEEE Journal of Selected Topics on Quantum Electronics*, vol. 5, pp. 648-657, 1999.

[87] M. L. Osowski, J. S. Hughes, R. M. Lammert, and J. J. Coleman, "An asymmetric cladding gain-coupled DFB laser with oxide defined metal surface grating by MOCVD," *IEEE Photonics Technology Letters*, vol. 9, pp. 1460-1462, 1997.

[88] H. A. Haus, and C. V. Shank, "Antisymmetric taper of distributed feedback lasers," *IEEE Journal of Quantum Electronics*, vol. 12, pp. 532-539, 1976.

[89] R. Krebs, F. Klopf, S., Rennon, J. P. Reithmaier, and A. Forchel, "InAs/GaInAs quantum dot DFB lasers emitting at 1.3 μm," *Electronics Letters*, vol. 37, pp. 634-636, 2001.

[90] M. V. Maximov, N. N. Ledentsov, V. M. Ustinov, Z. I. Alferov, and D. Bimberg, "GaAs-based 1.3 InGaAs quantum dot lasers: a status report," *Journal of Electronic Materials*, vol. 29, pp. 476-486, 2000.

[91] L. Zhang, T. F. Boggess, D. G. Deppe, D. L. Huffaker, O. B. Shchekin, and C. Cao, "Dynamic response of 1.3-μm-wavelength InGaAs/GaAs quantum dots," *Applied Physics Letters*, vol. 76, pp. 1222-1224, 2000.

[92] K. Nishi, H. Saito, S. Sugou, and J. Lee, "A narrow photoluminescence linewidth of 21 meV at 1.35 μm from strain-reduced InAs quantum dots covered by $In_{0.2}Ga_{0.8}As$ grown on GaAs substrates," *Applied Physics Letters*, vol. 74, pp. 1111-1113, 1999.

[93] E. C. Le Ru, P. Howe, T. S. Jones, and R. Murray, "Strain-engineered InAs/GaAs quantum dots for long-wavelength emission," *Physical Review B*, vol. 67, pp. 165303:1-5, 2003.

[94] L. S. Coldren, and S. W. Corzine, *Diode lasers and photonic integrated circuits*, Wiley, New York, 1995.

[95] K. P. O'Donnell, and X. Chen, "Temperature dependence of semiconductor band gaps," *Applied Physics Letters*, vol. 58, pp. 2924–2926, 1991.

[96] S. Ghosh, P. Bhattacharya, E. Stoner, J. Singh, H. Jiang, S. Nuttinck, and J. Laskar, "Temperature-dependent measurement of Auger recombination in self-organized $In_{0.4}Ga_{0.6}As$/GaAs quantum dots," *Applied Physics Letters*, vol. 79, pp. 722-724, 2001.

[97] M. Brasken, M. Lindberg, M. Soupanen, H. Lipsanen, and J. Tulkki, "Temperature dependence of carrier relaxation in strain-induced quantum dots," *Physical Review B*, vol. 58, R15993-15996, 1998.

[98] S. Krishna, P. Bhattacharya, J. Singh, T. Norris, J. Urayama, P. J. McCann, and K. Namjou, "Intersubband gain and stimulated emission in long-wavelength (λ=13 μm) intersubband In(Ga)As-GaAs quantum-dot electroluminescent devices," *IEEE Journal of Quantum Electronics*, vol. 37, pp. 1066-1074, 2001.

[99] I. P. Marko, A. D. Andreev, A. R. Adams, R. Krebs, J. P. Reithmaier, and A. Forchel, "The role of Auger recombination in InAs 1.3-μm quantum-dot lasers investigated using high hydrostatic pressure," *IEEE Journal of Selected Topics on Quantum Electronics*, vol. 9, pp. 1300-1307, 2003.

[100] B. W. Hakki, and T. L. Paoli, "Gain spectra in GaAs double-heterostructure injection lasers," *Journal of Applied Physics*, vol. 46, pp. 1299-1306, 1975.

[101] G. Liu, X. Jin, and S. L. Chuang, "Measurement of linewidth enhancement factor of semiconductor lasers using an injection-locking technique," *IEEE Photonics Technology Letters*, vol. 13, pp. 430-432, 2001.

[102] A. Markus, J. X. Chen, O. Gauthier-Lafaye, J.-G. Provost, C. Paranthoën, and A. Fiore, "Impact of intraband relaxation on the performance of a quantum dot laser," *IEEE Journal of Selected Topics on Quantum Electronics*, vol. 9, pp. 1308-1314, 2003.

[103] M. Grundmann, and D. Bimberg, "Theory of random population of quantum dots," *Physical Review B*, vol. 55, pp. 9740-9742, 1996.

[104] H. Jiang, and J. Singh, "Numerical simulation of the dynamic response of self-assembled $In_{0.4}Ga_{0.6}As$/GaAs quantum dot lasers," *Proceedings of SPIE International Society of Optical Engineering*, vol. 3547, pp. 341-349, 1998.

[105] N. Tessler, R. Nagar, and G. Eisenstein, "Structure dependent modulation response in quantum-well lasers," *IEEE Journal of Quantum Electronics*, vol. 28, pp. 2242-2250, 1992.

[106] R. Nagarajan, M. Ishikawa, T. Fukushima, R. S. Geels, and J. E. Bowers, "High speed quantum-well lasers and carrier transport effects," *IEEE Journal of Quantum Electronics*, vol. 28, pp. 1990-2008, 1992.

[107] J. R. Marciante, and G. Agrawal, "Nonlinear mechanisms of filamentation in broad-area semiconductor lasers," *IEEE Journal of Quantum Electronics*, vol. 32, pp. 590-596, 1996.

[108] J. K. Kim, T. A. Strand, R. L. Naone, and L. A. Coldren, "Design parameters for lateral carrier confinement in quantum-dot lasers," *Applied Physics Letters*, vol. 74, pp. 2752-2754, 1999.

[109] P. M. Smowton, E. J. Pearce, H. C. Schneider, W. W. Chow, and M. Hopkinson, "Filamentation and linewidth enhancement factor in InGaAs quantum dot lasers," *Applied Physics Letters*, vol. 81, pp. 3251-3253, 2002.

[110] Ch. Ribbat, R. L. Sellin, I. Kaiander, F. Hopfer, N. N. Ledentsov, D. Bimberg, A. R. Kovsh, V. M. Ustinov, A. E. Zhukov, and V. Maximov, "Complete suppression of filamentation and superior beam quality in quantum-dot lasers," *Applied Physics Letters*, vol. 82, pp. 952-954, 2003.

[111] B. Kochman, S. Ghosh, J. Singh, P. Bhattacharya, "Lateral hopping conductivity and large negative magnetoresistance in InAs/AlGaAs self-organized quantum dots," *Journal of Physics D: Applied Physics*, vol. 35, pp. L65-L68, 2002.

[112] J. K. Kim, T. A. Strand, R. L. Naone, and L. A. Coldren, "Design parameters for lateral carrier confinement in quantum-dot lasers," *Applied Physics Letters*, vol. 74, pp. 2752-2754, 1999.

[113] J. Stohs, D. J. Bossert, D. J. Gallant, and S. R. J. Brueck, "Gain, refractive index change, and linewidth enhancement factor in broad-area GaAs and InGaAs quantum-well lasers," *IEEE Journal of Quantum Electronics*, vol. 37, pp. 1449-1459, 2001.

[114] H. Saito, K. Nishi, A. Kamei, S. Sugou, "Low chirp observed in directly modulated quantum dot lasers," *IEEE Photonics Technology Letters*, vol. 12, pp. 1298-1300, 2000.

[115] S. L. Yellen, A. H. Shepard, R. J. Dalby, J. A. Bumann, H. B. Serreze, T. S. Guido, R. Soltz, K. J. Bystrom, C. M. Harding, and R. G. Waters, "Reliability of GaAs-based semiconductor diode lasers: 0.6-1.1 μm," *IEEE Journal of Quantum Electronics*, vol. 29, pp. 2058-2067, 1993.

[116] C. H. Henry, R. A. Logan, and F. R. Merritt, "Measurement of gain and absorption spectra in AlGaAs buried heterostructure lasers," *Journal of Applied Physics*, vol. 51, pp. 3042-3050, 1980.

[117] A. Oster, g. Erbert, and H. Wenzel, "Gain spectra measurements by a variable stripe length method with current injection," *Electronics Letters*, vol. 33, pp. 864-866, 1997.

[118] J. D. Thomson, H. D. Summers, P. J. Hulyer, P. M. Smowton, and P. Blood, "Determination of single-pass optical gain and internal loss using a multisection devices," *Applied Physics Letters*, vol. 76, pp. 2527-2529, 1999.

[119] C. Kittel, *Introduction to solid state physics*, 5th Edition, John Wiley & Sons, New York, 1976.

[120] A. van Esch, L. Van Boscktal, J. De Bock, G. Verbanck, A. S. van Steenbergen, P. J. Wellmann, B. Grietens, R. Bogaerts, F. Herlach, and G. Borghs, "Interplay between the magnetic and transport properties in the III-V diluted magnetic semiconductor $Ga_{1-x}Mn_xAs$," *Physical Review B*, vol. 56, pp. 13103-13112, 1997.

[121] J. Schneider, U. Kaufmann, W. Wilkening, M. Baeumler, and F. Kohl, "Electronic structure of the neutral manganese acceptor in gallium arsenide," *Physical Review Letters*, vol. 59, pp. 240-243, 1987.

[122] F. Matsukara, H. Ohno, A. Shen, and Y. Sugawra, "Transport properties and origin of ferromagnetism in (Ga,Mn)As," *Physical Review B*, vol. 57, pp. R2037-R2039, 1998.

[123] L. van Bockstal, A. van Esch, R. Bogaerts, F. Herlach, A. S. van Steenbergen, J. De Boeck, G. Borghs, "Magnetic interactions with charge carriers in III-V diluted magnetic semiconductors," *Physica B*, vol. 246-257, pp. 258-261, 1998.

[124] T. Dietl, H. Ohno, F. Matukura, J. Cibert, and D. Ferrand, "Zener model description of ferromagnetism in zinc-blende magnetic semiconductors," *Science*, vol. 287, pp. 1019-1022, 2000.

[125] S. Lee, J. Chung, I. S. Choi, Sh U. Yuldeshev, Hyunsik Im, T. W. Kang, W. –L. Lim, Y. Sasaki, X. Liu, T. Wojtowicz, and J. K. Furdyna, "Effect of Be doping on the properties of GaMnAs ferromagnetic semiconductors," *Journal of Applied Physics*, vol. 93, pp. 8307-8309, 2003.

[126] H. Munekata, H. Ohno, S. von Molnar, A. Segmuller, L. L. Chang, and L. Esaki, "Diluted magnetic III-V semiconductors," *Physical Review Letters*, vol. 63, pp. 1849-1852, 1989.

[127] H. Ohno, A. Shen, F. Matsukara, A. Oiwa, A. Endo, S. Katsumoto, and Y. Iye, "(Ga,Mn)As: A new diluted magnetic semiconductor based on GaAs," *Applied Physics Letters*, vol. 69, pp. 363-365, 1996.

[128] J. König, Hsiu-Hau Lin, and A. H. MacDonald, "Theory of Diluted Magnetic Semiconductor Ferromagnetism," *Physical Review Letters*, vol. 84, pp. 5628-5631, 2000.

[129] S. Sanvito, P. Ordejón, and N. A. Hill, "First-principles study of the origin and nature of ferromagnetism in $Ga_{1-x}Mn_xAs$," *Physical Review B*, vol. 63, pp. 165206:1-13, 2001.

[130] T. Hayashi, Y. Hoshimoto, S. Katsumoto, and Y. Iye, "Effect of low-temperature annealing on transport and magnetism of diluted magnetic semiconductors," *Applied Physics Letters*, vol. 78, pp. 1691-1693, 2001.

[131] S. J. Potashnik, K. C. Ku, S. H. Chun, J. J. Berry, N. Samath, and P. Schiffer, "Effects of annealing time on defect-controlled ferromagnetism in $Ga_{1-x}Mn_xAs$," *Applied Physics Letters*, vol. 79, pp. 1495-1497, 2001.

[132] K. M. Yu, W. Walukiewicz, T. Wojtowicz, I. Kuryliszyn, X. Liu, Y. Sasaki, and J. K. Furdyna, "Effect of location of Mn sites in ferromagnetic $Ga_{1-x}Mn_xAs$ on its Curie temperature," *Physical Review B*, vol. 65, pp. 201303:1-4, 2002.

[133] K. C. Ku, S. J. Potashnik, R. F. Wang, S. H. Chun, P. Schiffer, N. Samarth, M. J. Seong, A. Mascarehas, E. Johnston-Halperin, R. C. Myers, A. C. Gossard, and D. D. Awschalom, "Highly enhanced Curie temperature in low-temperature annealed [Ga,Mn]As epilayers," *Applied Physics Letters*, vol. 82, pp. 2302-2304, 2003.

[134] B. S. Sørensen, P. E. Lindelof, J. Sadowski, R. Mathieu, and P. Svedlindh, "Effect of annealing on carrier density and Curie temperature in epitaxial (Ga,Mn)As thin films," *Applied Physics Letters*, vol. 82, pp. 2287-2289, 2003.

[135] A. M. Nazmul, S. Sugahara, and M. Tanaka, "Ferromagnetism and high Curie temperature in semiconductor heterostructures with Mn δ-doped GaAs and p-type selective doping," *Physical Review B*, vol. 67, pp. 241308:1-4, 2003.

[136] Berciu and R. N. Bhatt, "Effects of disorder on ferromagnetism in diluted magnetic semiconductors," *Physical Review Letters*, vol. 87, pp. 107203:1-3, 2001.

[137] S. P. Guo, A. Shen, F. Matuskara, Y. Ohno, and H. Ohno, "Surfactant effect of Mn on the formation of self-organized InAs nanostructures," *Journal of Crystal Growth*, vol. 208, pp. 799-803, 2000.

[138] J. Shi, J. M. Kikkawa, D. D. Awschalom, G. Medeiros-Ribeiro, P. M. Petroff, and K. Babcock, "Magnetic properties and imaging of Mn-implanted GaAs semiconductors," *Journal of Applied Physics*, vol. 79, pp. 5296-5298, 1996.

[139] G. Bouzerar, J. Kudrnovský, and P. Bruno, "Disorder effects in diluted ferromagnetic semiconductors," *Physical Review B*, vol. 68, pp. 205311:1-4, 2003.

[140] A. L. Chudnovskiy and D. Pfannkuche, "Influence of disorder on ferromagnetism in diluted magnetic semiconductors," *Physical Review B*, vol. 65, pp. 165216:1-7, 2002.

[141] M. P. Kennett, M. Berciu, and R. N. Bhatt, "Monte Carlo simulations of an impurity-band model for III-V diluted magnetic semiconductors," *Physical Review B*, vol. 66, pp. 045207:1-16, 2002.

[142] T. Dietl and J. Spałek, "Effect of thermodynamic fluctuations of magnetization on the bound magnetic polaron in dilute magnetic semiconductors," *Physical Review B*, vol. 28, pp. 1548-1663, 1983.

[143] A. C. Durst, R. N. Bhatt, and P. A. Wolff, "Bound magnetic polaron interactions in insulating doped diluted magnetic semiconductors," *Physical Review B*, vol. 65, pp. 235205:1-10, 2002.

[144] G. Schmidt, and L. W. Molenkamp, "Electrical spin injection into semiconductors," *Physica E*, vol. 9, pp. 202-208, 1999.

[145] Y. Ohno, D. K. Young, B. Beschoten, F. Matsukura, H. Ohno, and D. D. Awschalom, "Electrical spin injection in a ferromagnetic semiconductor heterostructure," *Nature*, vol. 402, pp. 790-792, 1999.

[146] S. Ghosh and P. Bhattacharya, "Surface-emitting spin-polarized $In_{0.4}Ga_{0.6}As$/GaAs quantum-dot light-emitting diode," *Applied Physics Letters*, vol. 80, pp. 658-660, 2002.

[147] A. S. Lenihan, M. V. Gurdev Dutt, D. G. Steel, S. Ghosh, and P. K. Bhattacharya, "Raman coherence beats from entangled polarization eigenstates in InAs quantum dots," *Physical Review Letters*, vol. 88, pp. 223601:1-4, 2002.

[148] S. D. Offsey, L. F. Lester, W. J. Schaff, and L. F. Eastman, "High-speed modulation of strained-layer InGaAs-GaAs-AlGaAs ridge waveguide multiple quantum well lasers," *Applied Physics Letters*, vol. 58, pp. 2336-2338, 1991.

[149] S. Fathpour, P. Bhattacharya, S. Pradhan, S. Ghosh, and J. Topoľančik, "Modulation characteristics of $In_{0.4}Ga_{0.6}As$/GaAs quantum dot gain-coupled distributed feedback Lasers," 16th *IEEE Laser and Electro-Optics Society Annual Meeting Conference Proceedings*, pp. 202-203, Tucson, AZ, November 2003.

[150] D. L. Huffaker, L.A. Graham, and D.G. Deppe, "Low-threshold continuous-wave operation of an oxide-confined vertical cavity surface emitting laser based on a quantum dot active region and half-wave cavity," *Electronics Letters*, vol. 33, pp. 1225-1226, 1997.

[151] H. Z. Chen, J. Palaski, A. Yariv, and H. Morkoc, "High-frequency modulation of AlGaAs/GaAs lasers grown on Si substrate by molecular beam epitaxy," *Applied Physics Letters*, vol. 52, pp. 605-606, 1988.

[152] K. K. Linder, J. Phillips, O. Qasaimeh, X. F. Liu, S. Krishna, P. Bhattacharya, and J. C. Jiang, "Self-organized $In_{0.4}Ga_{0.6}As$ quantum-dot lasers grown on Si substrates," *Applied Physics Letters*, vol., 74, pp. 1355-1357, 1999.

[153] H. von. Kanel, C. Roseblad, M. Kummer, E. Muller, T. Graf, and T. Hackbarth, "Fast Deposition Process for Graded SiGe Buffer Layers," *Japanese Journal of Applied Physics*, vol. 39, pp. 2050-2053, 2000.

[154] M. T. Currie, S. B. Samavedam, T. A. Langdo, C. W. Leitz, and E. A. Fitzgerald, "Controlling threading dislocation densities in Ge on Si using graded SiGe layers and chemical-mechanical polishing," *Applied Physics Letters*, vol. 72, pp. 1718-1720, 1998.

[155] E. A. Fitzgerald, G. P. Watson, E. P. Proano, D. G. Ast, "Nucleation mechanisms and the elimination of misfit dislocations at mismatched interfaces by reduction in growth area," *Journal of Applied Physics*, vol. 65, pp. 2220-2237, 1989.

[156] H. Gebretsadik, O. Qasaimeh, J. Hongtao P. Bhattacharya,C. Caneau, R. Bhat, "Design and realization of a 1.55-μm patterned vertical cavity surface emitting laser with lattice-mismatched mirror layers," *Journal of Lightwave Technology*, vol. 17, pp. 2595-2604, 1999.

[157] S. Fathpour, M. Holub, S. Chakrabarti, P. Bhattacharya, “Spin-polarised quantum dot light-emitting diodes with high polarisation efficiency at high temperatures,” *Electronics Letters*, vol. 40, pp. 694 – 695, 2004.

[158] S. Chakrabarti, M. A. Holub,P. Bhattacharya, T. D. Mishima, M. B. Santos, M. B. Johnson, M. B. D. A. Blom, “Spin-polarized light-emitting diodes with Mn-doped InAs quantum dot nanomagnets as a spin aligner,” *Nano Letters*, vol. 5, pp. 209-212, 2005.

[159] M. Holub, J. Shin, S. Chakrabarti, and P. Bhattacharya, “Electrically-injected spin-polarized vertical-cavity surface-emitting lasers,” submitted to *Applied Physics Letters*.

[160] T. Hayashi, M. Tanaka, K. Seto, T. Nishinaga, H. Shimada, K. Ando, “Hall effect and magnetic properties of III–V based ($Ga_{1-x}Mn_x$)As/AlAs magnetic semiconductor superlattices,” *Journal of Applied Physics*, vol. 83, pp. 6551-6553, 1998.